ofioliti
An International Journal
on Ophiolites and Modern Oceanic Lithosphere

JOURNAL PRE-PROOF

Metasomatic horizon sealing serpentinite-metasediments pair in the Zermatt-Saas metaophiolite (Northwestern Alps): record of a channel for focussed fluid flow during subduction

Francesca Claudia Rotondo, Paola Tartarotti, Sara Guerini, Giovanna Della Porta, Nicola Campomenosi

To appear in OFIOLITI

DOI: https://doi.org/10.4454/ofioliti.v46i1.535

Received date: 3 June 2020

Accepted date: 17 September 2020

Pre-Proof

METASOMATIC HORIZON SEALING SERPENTINITE-METASEDIMENTS PAIR IN THE ZERMATT-SAAS METAOPHIOLITE (NORTHWESTERN ALPS): RECORD OF A CHANNEL FOR FOCUSSED FLUID FLOW DURING SUBDUCTION

Francesca Claudia Rotondo*[1], Paola Tartarotti*, Sara Guerini*, Giovanna Della Porta*, Nicola Campomenosi**

** Dipartimento di Scienze della Terra "Ardito Desio", Università degli Studi di Milano, Italy*
*** Dipartimento di Scienze della Terra, Ambiente e Vita DISTAV - Università di Genova, Italy*
1. Now at the National Oceanography Centre Southampton, University of Southampton, United Kingdom

Corresponding author, email: F.Rotondo@southampton.ac.uk

Keywords: *metasomatic rocks; metaophiolites and metaophicarbonates; Jurassic Tethys; subduction; Zermatt-Saas Zone; Northwestern Alps; Italy*

ABSTRACT

A metasomatic horizon (MH) occurs between the metaophiolite (serpentinite and metaophicarbonates) basement and metasedimentary sequence (chaotic rocks and calcschists) of the Lake Miserin Ophiolite, in the high pressure Zermatt-Saas Zone of the Northwestern Alps. Macro- and microstructural analyses combined with petrological and geochemical investigations of the MH and surrounding lithologies unravelled a polyphase blastesis-deformation history, which led to the formation of a complex fabric and minero-chemical alteration of the serpentinite basement-metasediments interface. Dehydration, decarbonation and carbonation interplayed from early Alpine subduction up to HP-LT metamorphic peak (T=550-630 °C, P=1.8-2.5 GPa), to produce a distinctive, pervasive amphibole (tremolite/actinolite) replacement both in carbonate-rich and serpentinite-rich domains pertaining to the MH protoliths, i.e. serpentinite and carbonate-bearing metabreccia of the chaotic rock unit. This characteristic amphibole metasomatism is more pronounced toward the contact with the metaophicarbonates, and the average $\delta^{18}O_{VSMOW}$ and $\delta^{13}C_{VPDB}$ values of dolomite within the MH (+14.4‰ and +0.7‰ respectively) lie between those of the metaophicarbonates and of calcschist. These results suggest that Mg- H_2O-rich fluids from the dehydrating slab, CO_2 released by decarbonation and SiO_2-rich fluids evolved in calcschists mixed together and circulated mostly along the metaophiolite basement/metasediments interface, where the MH developed and recorded a preferential channel for mixed metamorphic fluid flow. These findings highlight and confirm that the study of metasomatic rocks in convergent systems is crucial to comprehend the behaviour of different fluids circulating, mixing and interacting with lithologies along slab-parallel discontinuities, which act as major fluid conduits for deep volatile recycling.

INTRODUCTION

The fluid-driven metamorphic reactions occurring along the "subduction channel" (Shreve and Cloos, 1986) during plate convergence are countless and responsible for the production of thick sequences (tens of metres

scale) of minero-chemically altered or hybrid metasomatic rocks (e.g., Bebout and Barton, 1993, 2002; Spandler et al., 2008; Bebout, 2012; Angiboust et al., 2014; Scambelluri et al., 2016; Piccoli et al., 2018). Scientific interest has been recently arising on high pressure (HP) metasomatic rocks as a potential record for fluid transport, mass transfer and volatiles deep-recycling across and along the subduction interface, although remnants of high pressure (HP) fluid-rock interaction are exposed in scarce and dimensionally limited outcrops (e.g., Angiboust et al., 2014, 2017; Scambelluri et al., 2016; Fornash and Whitney, 2020). Metasomatism is favoured by the mechanical coupling of chemically disparate lithologies during the onset of subduction (e.g., Angiboust et al., 2011), such as sediments, mafic and ultramafic rocks, and likely also by chaotic assemblages of mechanically different rocks (i.e., mélanges; Festa et al., 2019). Subduction-zone metasomatism can be activated at structural shallow levels, as the oceanic lithospheric slab (with sediments) bends while entering the trench, thus it is potentially infiltrated by seawater along fractures and faults. At the same time, sediments accreted in the forearc begin to undergo extensive physical compaction, fluid expulsion, and diagenetic alteration (e.g., Bebout, 2012). At greater depths, a series of dehydration reactions occur (Schmidt and Poli, 1998) and the release of H_2O-rich fluids is able to extensively hydrate and metasomatise the hanging walls of subduction zones (i.e., slab-mantle interface and mantle wedge).

Our study documents the occurrence of a pervasive metasomatic horizon within high-pressure (HP)-metaophiolites in the Northwestern Alps (Zermatt-Saas Zone). This horizon marks the contact between serpentinites/metaophicarbonates and carbonate-rich metasediments including a chaotic rock unit. Structural investigations from meso- to micro-scale of the metasomatic rocks were integrated with electron microprobe, Raman spectroscopy, stable oxygen, and carbon isotope analyses performed on selected mineral phases, in order to constrain the relative timing of metasomatism with respect to the metaophiolite evolution, from the oceanic stage to the onset of the Alpine subduction, HP-peak condition, and exhumation. The direct juxtaposition of ultramafic and carbonate-rich rocks, frequently observed in the Northwestern Alps metaophiolites and in modern slow spreading oceanic lithosphere, can be regarded as a crucial assemblage characterised by contrasting rheology. Possible qualitative chemical reactions are proposed for the formation of the metasomatic horizon within this lithological interface, which may have acted as a mechanical discontinuity facilitating fluid channelization, thus promoting metasomatic reactions at least since the inception of the Alpine subduction.

GEOLOGICAL BACKGROUND

The study area is located in the high Champorcher valley (Aosta Valley region, NW Alps, Italy; Fig. 1), characterized by the occurrence of metaophiolites comparable to the Zermatt-Saas Zone (hereafter ZS; Dal Piaz, 1965; Bearth, 1967; Dal Piaz and Ernst, 1978), which represents the fossil oceanic lithosphere of the Ligurian-Piedmont basin, a branch of the Jurassic Tethyan Ocean. This ocean basin developed as a result of rift-to-drift and seafloor spreading occurred between 165 and 150 Ma, according to U/Pb dating on ophiolitic gabbros

Pre-Proof

(Manatschal and Müntener, 2009 for a review) and to palaeontological dating on post-rift radiolarian cherts overlying the gabbros (see Bill et al., 2001 and ref. therein). The Ligurian-Piedmont oceanic lithosphere (i.e., the eventual ZS) underwent subduction along the margin of the African plate early in the Alpine orogeny, and exhumed as ophiolite fragments that were tectonically stacked within the western Alpine belt, between the Penninic (palaeo-Europe) and the Austroalpine (palaeo-Africa) continental domains (Fig. 1b; e.g., Bigi et al., 1990; Dal Piaz, 1999, 2001; Frey et al., 1999; Dal Piaz et al., 2008). The Champorcher valley metaophiolites are tectonically juxtaposed between the eclogitic Lower Austroalpine "outliers" of the Tour Ponton, Glacier-Rafray, and other minor slivers (Dal Piaz and Nervo, 1971; Nervo and Polino, 1976; Dal Piaz et al., 2008; Fig. 1b) and the Penninic Gran Paradiso massif (Fig. 1b).

The ZS recalls the typical rock sequence of slow-spreading oceanic lithosphere (e.g., Atlantic Ocean; Lagabrielle and Cannat, 1990; Lagabrielle, 2009; Tartarotti et al., 2017), which includes ultramafic rocks, metagabbros and metabasalts with locally preserved slices of metasediments (e.g., Bearth and Schwander, 1981). Most ZS lithologies display high-pressure (HP) to ultra-high (UHP) mineral assemblages (Ernst and Dal Piaz, 1978; Reinecke, 1998; Bucher et al., 2005; Angiboust et al., 2009; Groppo et al., 2009; Frezzotti et al., 2011; Luoni et al., 2018), with minor to moderate replacement of the HP minerals by greenschist-facies assemblages (Cartwright and Barnicoat, 1999 and ref. therein). In the high Champorcher valley, metaophiolites mainly consist of serpentinites and metaophicarbonate breccias overlain by flysch-type calcschists (Tartarotti et al., 2019 and ref. therein). Serpentinites are more widely exposed to the north of the Champorcher valley, where they constitute the Mount Avic massif, for an area of ca. 180 km^2 (Dal Piaz et al., 2008; Fontana et al., 2015) and show Alpine HP mineral parageneses, including olivine, Ti-clinohumite, antigorite, magnetite. The Mount Avic serpentinites have been interpreted as deriving from a mantle peridotite protolith as attested by, although rare, pre-Alpine (oceanic) mineral relics (Fontana et al., 2008, 2015). Serpentinites and metaophicarbonate breccias of the high Champorcher valley are covered by a metasedimentary chaotic rock unit, ca. 40 m thick (i.e., the "Composite Chaotic Unit" or "CCU" of Tartarotti et al., 2017, 2019), showing a block-in-matrix texture and consisting of ultramafic clasts and brecciated blocks embedded within a carbonate-rich matrix. The CCU has been interpreted as the final result of both gravity-driven sedimentary processes in a sector of the Jurassic Ligurian-Piedmont Ocean and Alpine polyphase deformation (Tartarotti et al., 2019). The contact between serpentinites+ophicarbonates and the CCU is distinctly marked by metasomatic rocks (hereafter, "metasomatic horizon" or "MH") that constitute a fairly continuous horizon with a centimetres to metres thickness. The MH commonly shows a layered internal structure marked by carbonate-rich layers and lenses usually boudinaged, alternating with amphibole+clinopyroxene-rich layers. The polyphase Alpine folding, superposition of folds, boudinage, stretching, and shearing created the complex present structure of the metasomatic horizon that is here correlated with various metamorphic mineral assemblages. The overall metaophiolite sequence is completed by flysch-type metasediments (i.e., the "Calcschist Unit" or "CSU" of Tartarotti et al., 2017), representing post-extensional sedimentation sealing the syn-extensional ophiolite architecture (Tartarotti et al., 2017).

Pre-Proof

ANALYTICAL METHODS

Field mapping

Common techniques of field mapping and structural geology were adopted in the field in order to determine the lithostratigraphy in the study area and for reconstructing its tectonic evolution based on superimposed deformation phases related to the Alpine history.

Petrographic and microstructural analyses

The sampling strategy adopted in the field was to have a complete record of all lithologies within the metaophiolite basement and MH, in order to investigate the different rock fabrics and to evaluate their mineral paragenesis in relation to the deformation history. The petrographic and microstructural analyses were performed by means of optical microscope on 80 standard thin sections (30 μm thick). Thin sections with carbonate minerals were stained with alizarin red to discriminate between calcite and dolomite (Dickson, 1966). The terminology adopted in the present work for microstructural analysis is taken from Vernon (2004) and Passchier and Trouw (2005). Mineral abbreviations adopted throughout the text are taken from Whitney and Evans (2010), except for white mica (Wm). Note that abbreviation "Cb" stays for "carbonate mineral group". The recrystallization stages of Cal (Cal1, Cal2, Cal3) and Dol (Dol1, Dol2) are based on Tartarotti et al. (2019).

Cathodoluminescence analysis was performed on 2 polished thin sections (samples MIS46 from CCU, MIS64bis from CSU; see Fig. S2) to investigate the carbonate phases (cf. Machel, 2004) using a CITL Optical Cathodoluminoscope at the Dipartimento di Scienze della Terra, University of Milano (Italy), operated at 10-14kV accelerating voltage and 0.5 mA gun current intensity.

Minerochemical analysis – Electron microprobe (EMPA)

The quantitative mineral chemistry analyses of the rock-forming minerals were carried out on seven thin sections using a JEOL 8200 Super Probe, at the Dipartimento di Scienze della Terra, University of Milano (Italy). A WDS system was used at 15 kV of acceleration voltage on the tungsten filament and 5 nA of current electron beam, with a point analysis of 1 μm of diameter. The standards used were: Na on omphacite, Mg on olivine, Al-Si-Ca on grossular, Ti on ilmenite, Mn on rhodonite, Fe on fayalite, K on K-feldspar, Cr on metallic/pure Cr, Ni on niccolite and Sr on celestine. The WDS spectrometers used were: TAP (for Na, Mg, Al, Si), PET-J (for Sr, Ti, Cr), LIFH (for Mn, Fe, Ni) and PETH (for K and Ca). Thin sections were carbon coated with a C film (ca. 20 μm thick). The values of oxides in wt. % were recalculated to atomic proportion using the program NORM (Peter Ulmer, ETHZ, revised by Poli, 2001, personal communication). Results from electron microprobe analyses are reported in Tables S1-S6 (Supplementary files).

Pre-Proof

Serpentine characterization – X-ray powder diffraction (XRD)

The serpentine group polymorphs and their bearing serpentinite (3 samples) were investigated by high-resolution X-ray powder diffractometer Panalytical X'pert Pro, at the Dipartimento di Scienze della Terra, University of Milano (Italy). The samples have been back-loaded on a flat sample-holder and measured with the usual Bragg Brentano geometry (divergent beam). The detector is a multi-channel X'Celerator (Cu Kα, with λ=0.154187 nm), which allows a very fast qualitative data collection. Data were collected in the range 5–80° 2θ with a step size of about 0.02° 2θ and a counting time of about 30 s/step. The three chief polymorphs of serpentine (lizardite, antigorite and chrysotile) were distinguished on the basis of reference XRD patterns for the serpentine minerals in the Powder Diffraction File database 1997: lizardite 11-386 and 18-779, antigorite 7-417 and chrysotile 10-380 (Wicks, 2000).

Serpentine characterization – Raman spectroscopy

Micro-Raman spectroscopic analyses were carried out at the University of Genova (DISTAV), using a Horiba Jobin-Yvon Explora_Plus single monochromator spectrometer (grating of 2400 grooves/mm), equipped with an Olympus BX41 confocal microscope. The 532-nm line of Nd:YAG solid-state laser was used as excitation source. The spectral resolution is about 2 cm-1 and the instrumental accuracy in determining the peak position is ~0.5 cm^{-1}. The Raman peak of silicon (520.5 cm^{-1}) was used to calibrate the system before the analysis session. The spectra were collected with the 100x objective (n.a. 0.9) with different acquisition time (15 and 25 s with 5 accumulations), in order to obtain the best signal-background ratio. Raman spectra were collected in the spectral ranges 150-1150 cm^{-1} and 3600-3800 cm^{-1}. Serpentine polymorphs, carbonates and other mineral phases from three thin sections (2 serpentinites and 1 metasomatic rock) were analysed in the same points investigated by the electron microprobe.

Stable oxygen and carbon isotope analyses

Twenty-seven carbonate powder samples were extracted with a handheld microdrill from four rock samples (Table S7). Analysed powder samples are: 4 samples from an intrafolial calcite vein from the metaophicarbonate of the metaophiolite basement (sample 6); 7 samples from carbonate (dolomite) porphyroblasts from the MH (sample E9); 12 samples from the BrFm1 lithotype of the CCU (sample MIS46; 4 powders from a late calcite vein; 4 powders from calcite-rich serpentinite clasts; 4 powders from the dolomite-rich matrix); 4 samples from calcite-rich lithons from the CSU (sample MIS64bis).

Stable oxygen and carbon isotope analyses of these 27 carbonate powder samples were performed using an automated carbonate preparation device (GasBench II) connected to a Delta V Advantage (Thermo Fisher Scientific Inc.) isotopic ratio mass spectrometer at the Dipartimento di Scienze della Terra, University of Milano (Italy). Carbonate powders (nearly 200 µg) were reacted offline with > 99% orthophosphoric acid; reaction time

Pre-Proof

was 1 to 3 hours at 70°C. The carbon and oxygen isotope compositions are expressed in the conventional delta notation calibrated to the Vienna Pee-Dee Belemnite (VPDB) scale by the international standards IAEA 603 ($\delta^{18}O$ = -2.37 ± 0.04 and $\delta^{13}C$ = +2.46 ± 0.01) and NBS-18 ($\delta^{18}O$ = -23.2 ± 0.1 and $\delta^{13}C$ = -5.014 ± 0.035) and internal laboratory standards. Analytical reproducibility for these analyses was better than ± 0.1‰ for both $\delta^{18}O$ and $\delta^{13}C$ values. For the conversion of the $\delta^{18}O$ values between the VPDB and VSMOW scales, the equation proposed by Kim et al. (2015) was used.

FIELD OBSERVATIONS

The study area is located in the high Champorcher valley near Lake Miserin (2576 m a.s.l.; Figs. 1, 2 and 3); the area is ca. 1.5 km^2 wide, and is part of the Mont Avic Natural Park. The Lake Miserin ophiolite (i.e., the LMO of Tartarotti et al., 2017) consists of a metaophiolite basement, mainly composed of serpentinites, overlain by a more erodible and soft metasedimentary sequence. The metaophiolite basement includes massive to foliated or schistose Atg-serpentinites and associated metaophicarbonates. Serpentinites are mainly composed of Srp, Mag, and seldom, in the foliated types, of oxidized patches of Dol constituting centimetres-sized lenticular or eye-shaped aggregates elongated along the foliation.

The metasedimentary sequence comprises, from bottom to top: 1) the CCU, consisting of ultramafic clasts/blocks embedded within a Cal+Dol-rich matrix, varying from clast- to matrix-supported. Clasts and blocks are characterized by different size, shape, nature and abundance; the matrix is purely carbonate-rich or impure in composition. On the base of different clast/matrix ratio and size and nature of clasts, four types of metabreccias were distinguished in the CCU (Tartarotti et al., 2019); 2) the CSU, Calcschist unit representing the post-rift metasedimentary cover unit (Tartarotti et al., 2019). It mainly consists of calcschists characterized by a continuous to spaced foliation defined by Cal-rich layers (Cal=35-75 vol.%) alternating with Wm-rich layers (Wm=15-25 vol.%), and by abundant Lws pseudomorphs often stretched in lineated aggregates. Calcschists include metres-thick micaschist levels consisting of Qtz+Grt+Wm+Cld, interlayered with quartz-rich portions (metaquartzites layers). This unit is at the top of the whole metaophiolite sequence, although it often directly overlies the serpentinite+metaophicarbonate basement (Figs. 2 and 3).

The contact between the metaophiolite basement and the metasedimentary sequence is marked by the MH, which is the focus of this study. The MH is a centimetres- to metres-thick horizon, more or less continuous, consisting of Cb (Dol±Cal) and green amphiboles (Tr/Act), which overall provide the rock with a distinctive green and orange (or brownish) colour (Fig. 4). The MH is widely distributed in the area, although it changes in thickness (varying from 10 cm up to 4 m) due to intense ductile Alpine deformation. The MH is systematically interposed between the serpentinites and the overlying metasedimentary rocks, but it also occurs along the tectonic contact between serpentinites and the CSU (Figs. 2 and 3c); it has never been observed between the CCU and the CSU.

Pre-Proof

The MH has a general block-in-matrix fabric as evidenced by the occurrence of dm-scale blocks and mm- to cm-scale clasts embedded within a foliated matrix, which is characterized by fine-grained aggregates of Dol±Cal+Amp±Chl±Op (mostly Mag). The shape of blocks ranges from sub-rounded to sigmoidal due to increasing boudinage and shearing; they often show a massive or blocky texture. Moderate to highly transposed clasts are frequently foliated, with an internal foliation (S_i) parallel or sub-parallel to the main external foliation (S_e). Three different types of rock are distinguished from bottom to top in the MH (Figs. 3 and 4), i.e. MH1, MH2 and MH3.

MH1 is a clast-supported metabreccia, cm- to dm-thick, often occurring between serpentinites or metaophicarbonate and MH2; clasts (mm-/cm-sized) are enriched in Amp, are not or weakly foliated, and are embedded in a Dol±Cal-rich matrix (Figs. 3 and 4a).

MH2 is the most common rock type occurring within the MH; it has a brecciated to foliated fabric, where blocks/clasts are variously transposed into the main foliation (Figs. 4b, 4c and 4d). Accordingly, the foliation plane locally includes either cm- to dm-sized relict clasts, not completely transposed, or highly disrupted levels (cm- to dm-thick) with a breccia-like texture (Figs. 4c and 4d). In most foliated types, relict isoclinal fold hinges can be observed (Fig. 4b), attesting the occurrence of a previous foliation (i.e., S_1) evidenced by a mineral layering defined by mm-thick layers of Dol (±Op) alternating with layers of Amp±Chl (±Op; Fig. 4b).

MH3 consists of Amp-rich layers that embed Dol-porphyroblasts or patches, sometimes with a lense or sigmoidal shape (Figs. 4e and 4f). Amp-rich layers seldom alternate with epidote-rich or Dol±Cal-rich layers. This rock type occurs randomly throughout the whole MH, sometimes in correspondence of intense shear zones near the contact with CSU.

Different structures were identified in the metaophiolites of the study area, attributable to at least five deformation phases, four ductile and one brittle. The oldest structure recognizable in the field is S_1, i.e. the oldest foliation, which recrystallized from the primary sedimentary bedding (i.e., S_0) in the CSU. The ductile deformation phase D_2 produced the foliation S_2, present in the whole LMO sequence and marked by different mineral assemblages. S_2 is characterized by a pervasive fabric that is axial planar to (F_2) isoclinal folds, dipping northward or southward (NNW or SSE, girdle distribution with a high range of inclinations > 10°). In the metabreccias of the CCU (e.g., the BrFm2 defined by Tartarotti et al., 2019), the oldest structure (S_1) is still visible in the field and mostly corresponds to the clast-matrix contacts, generally deformed by subsequent D_2 phase. The D_2 phase gave rise to elongated and boudinaged clasts with Di+Dol fibres growing as extensional veins parallel to the direction of stretching within boudin necks. The S_2 foliation is crenulated and folded during the following ductile D_3 phase, characterized by asymmetric, polyharmonic open (F_3) folds (interlimb angle: 120°-70°), with sub-horizontal axial plane and randomly distributed A_3 axes. Only in the CSU, the D_3 phase forms dm-scale gentle folds (interlimb angle of 120°-180°) with sub-horizontal axial plane and asymmetric (S-Z) geometry, while the D_4 ductile phase is recognizable by a dome-and-basin geometry produced by metre to tens of metres-scale folds with a sub-vertical axial plane. In the whole area, the last brittle deformation phase D_5

Pre-Proof

produced different extensional fracture systems that crosscut the previous ductile structures, with filling minerals including Qz in the calcschists and Cal in the serpentinites, metaophicarbonates, and CCU metabreccias.

The MH, although characterized by a general block-in-matrix fabric, retains different internal structures. The most prominent structure in the MH, as in the whole study area, is the S_2 foliation, which in the MH is mainly characterized by mineralogical layering, commonly defined by layers of Dol±Cal (±Op) alternating with layers of Amp±Chl (±Op). The D_2 deformation phase is frequently characterized by a shear component that results, in the MH as in the CCU, into boudinage and shearing of the components, but mostly, in the sigmoidal shape of clasts and blocks. Structures that developed before the D_2 phase are: *i)* the poorly foliated clastic texture of MH1, consisting of Amp-rich clasts and carbonate-rich matrix; *ii)* an inferred relict S_1 foliation, showing a layered fabric and observed in isoclinal fold hinges attributable to the D_2 phase (see Fig. 4b). Structures younger than S_2 are difficult to be recognized in the MH, due to the contrasting competence of clasts and matrix often resulting in a disharmonic folding.

MICROSTRUCTURES AND PETROGRAPHY

The microstructural analysis and deformation history deduced from thin section observations is fundamental for integrating outcrop scale observations. A complete list of rock samples selected for thin section observations is reported in Table 1.

The principal structure largely identified in the field (and at a regional scale; see §2) is the main foliation S_2. Consequently, the microstructures and relative stable mineral associations are distinguished into pre-D_2, syn-D_2, or post-D_2 structures if they are products of previous, synchronous, or subsequent deformation phases or metamorphic events with respect to the D_2 phase, respectively, based on overprinting relations. Relative time relationships between deformation phases and stable mineral assemblages are summarized in Table 2.

Metaophiolite basement

The metaophiolite basement encompasses different kinds of serpentinite showing a massive to foliated fabric, and few portions of metaophicarbonates and their associated vein sets.

Serpentinite

Massive serpentinite (e.g., thin section C1, Tab. 1) still preserves relict microstructures of the mantle peridotite protolith and of oceanic serpentinization. Among the former, Cpx and Spl porphyroblasts were recognized. Cpx porphyroblasts show curved, mostly irregular grain boundaries, often with embayments and protrusions (Fig. 5a). Small (<< 1mm) rounded aggregates of Srp fibres occur inside Cpx porphyroblasts (Fig. 5a). Cpx may show a strong zonation defined by inclusion-rich cores and inclusion-free rims that is here interpreted as being due to the Alpine recrystallization of mantle Cpx porphyroblasts. Spl porphyroblasts consist

Pre-Proof

of Mag+Fe-Chr crystals exhibiting holly-leaf or anhedral shapes (Fig. 5b), reminiscent of original mantle Spl, rimmed by Srp+Chl aggregates. Fine-grained aggregates of Srp show a gridlike texture (Pichler and Schmitt-Riegraf, 1997), which may represent relict mesh texture, probably replacing former Ol (Fig. 5a, lower right corner). In some massive serpentinites, serpentinization is almost complete (only a few Cpx porphyroclasts are present), foliation is more pervasive and often characterized by the development of S-C shear bands. In spite of pervasive serpentinization, relict S_1 foliation is still recognizable and marked by isoclinal fold hinges underlined by Mag crystals rimmed by Srp±Chl aggregates. Antitaxial veins filled with Srp fibres crosscut the whole serpentinite texture (Tab. 2).

Foliated serpentinites are fine-grained to microcrystalline rocks (samples B1, B2, C2, CRB2; Tab. 1), and consist of Srp (85-95 vol.%), and Spl (up to 5 vol.%). Sometimes there are up to 25% of Mgs+Dol aggregates that define, with their shape preferred orientation (hereafter SPO), the main S_2 foliation together with Spl SPO, marking a mineral lineation (L_2). Mgs occurs in relict sites partially replaced by coarse-grained Dol (Dol1) ±Srp (Fig. 5c). Mgs+Dol1 aggregates are inequigranular interlobate, chemically zoned (see below) and ductilely deformed (Fig. 5c). Dol2 neoblasts recrystallized from Dol1 (Fig. 5c) and also fill veins that crosscut the serpentinite foliation (thin section B1; Tab. 1). Srp occurs both as fibres that grow in two preferred orientation forming a grid (gridlike texture) within the S_2 foliation, and as cryptocrystalline (<100µm) pseudomorphs (Srp1) on former primary mantle minerals (e.g., Pl or Px), essentially inferred from the shape of the ghost mineral and the occurrence of relict exsolution lamellae and cleavage plane traces. Fine-grained Srp2 aggregates developed around Srp1 and along the S_2 foliation. Here as well, shear component produced C- and C'-type shear bands, boudinaged Mag fish and sigmoid-shaped Srp1 aggregates. In foliated serpentinites Spl may show a holly-leaf habit and chemical zoning marked by Al-Chr-rich cores and Fe-Chr (I)- and Mag (II)-rich rims (Fig. 5d; see Tab. S6). Thus also foliated serpentinites may preserve textural and mineralogical features of mantle spinels (e.g., Fontana et al., 2008; Sansone et al., 2012). More frequently, Spl occurs as euhedral to anhedral Mag crystals that sometimes preserve Fe-Chr-rich cores (e.g., spinels in Fig. 5b).

In summary, serpentinites are characterized by relict textures and (rare) mineralogy attributable to the pre-Alpine (oceanic) history (pre-D_1 phase in Tab. 2), followed by the Alpine prograde D_1 and D_2 phases dominated by crystallization of Srp1-2, Mgs, Dol1-2, Di, Amp and Chl. Srp2 and Dol2 dominate the D_3 phase, while late crystallization of Cal3 marks the post-D_3 phase (Tab. 2).

The X-ray powder diffraction (XRD) patterns of the three analysed serpentinite samples (B1, C1, and C2; Tab. and Fig. S1) show that the serpentine species identified is a mixture of antigorite and lizardite, where Atg constitutes the dominant polymorph. No chrysotile type was identified in the analysed samples.

Metaophicarbonate

Metaophicarbonates (e.g., thin sections B3 and B4, Tab. 1) are mainly constituted by serpentinite domains (~50%) and Dol-rich veins (~50%). Boudinaged σ-type sigmoidal aggregates of Srp have pressure shadows and

Pre-Proof

boudin necks filled with elongated fine-grained Dol2 crystal aggregates, which partly include transposed Srp portions. Dol-rich domains are constituted by inequigranular interlobate aggregates including coarse-grained Dol1 with linear thick and thin twins, and polygonal or stretched Dol2 grains rimming Dol1 porphyroblasts.

Different sets of vein crosscut the metaophicarbonates and are associated to Alpine deformation stages (thin sections C4A, C4B, C6, C7B, Tabs. 1 and 2; sample 6, Tab. S7 and Fig. S2). These sets include: *i)* intrafolial veins, parallel to S_2, filled either by Srp fibres with SPO perpendicular to the vein selvedges or by Amp±Cal aggregates with random crystal orientation, attributed to an early Alpine stage or even older (oceanic?); *ii)* tension gashes opened inside the intrafolial veins. These gashes are filled with deformed Dol1 crystals, up to 2 mm in size, recrystallized into fine-grained Dol2 aggregates, and Di (Cpx), occurring as fibres or elongated prismatic crystals or crystal aggregates. This second set of Di+Dol veins is related to a subduction stage or to a retrograde stage (syn- and/or post- peak metamorphic conditions), as veins are both at high and low angle to the S_2 foliation (Tab. 2); *iii)* shear Cal veins, constituted by 100% fine-grained Cal3 as polygonal to interlobate crystal aggregates. These veins likely developed during late brittle deformation stages, during shallower exhumation stages, as shear plane direction is perpendicular to the S_2 planes in metaophicarbonate, and at a high angle to the tension gashes inside intrafolial veins.

In summary, metaophicarbonates contain minor amount of Di than serpentinites and include several sets of vein, both syn-tectonic and post-tectonic with respect to the D_2 HP phase. Metaophicarbonates do not show relics of the mantle protolith, instead, they record the Alpine evolution from the prograde D_1 and D_2 steps, as attested by boudinage and development of S_2 foliation, to the late Alpine events dominated by shear structures and late brittle structures (Tab. 2).

Metasomatic horizon (MH)

MH1

The MH1 occurs in contact with metaophicarbonate or with serpentinite (see Figs. 3c and 4a for outcrop view). It is mostly composed of coarse- to medium-grained Dol1+Dol2 domains surrounded by medium- to fine-grained Amp aggregates (Figs. 5e and 5f; thin sections B5 and E9; Tab. 1). Dol1 porphyroblast is the most abundant Dol phase, generally rich in inclusions of Cpx, Chl±Srp. Dol1 was stable during D_1 and started to deform and dynamically recrystallize into Dol2 new grains during D_2 (Tab. 2). Amp grew likely at the expense of a previous mineral and in part of Dol1, although Amp may also be in textural equilibrium with Dol1. Chl crystallized at the expense of opaque mineral relics (Spl?), and Cal3 is a late mineral phase that replaces Dol1, Dol2, Amp and Chl (Fig. 5e). Dol2+Amp are attributed to the D_2 phase because they represent the main mineralogical association marking the S_2 foliation in more schistose metasomatic rocks (i.e., MH2), developed as axial plane of D_2 isoclinal folds. After D_2, Cal3 largely crystallized in these rocks, filling Dol1 rhomboidal cleavages and microfractures, or occurring as inclusions in Amp, or in interstices or boudin necks (Fig. 5f).

Pre-Proof

MH2

The MH2 (e.g., Figs. 6a, 6b, 6c and 6d; thin sections B6, B8, B10A, B10B, B11, B12, B13A, B13B, E7; Tab. 1) represents the thickest MH type, commonly interposed between MH1 and MH3. The main foliation (S_2) is spaced to zonal and characterized by Amp+Op±Chl±Srp- rich domains alternating with microlithons made of fine- to medium-grained Dol±Cal±Amp (see also Fig. 4b for outcrop view).

Amp in Amp-rich domains is represented by both fine-grained elongated crystals (neoblasts) and coarse-grained, isolated, subhedral, often boudinaged porphyroclasts, suggesting the occurrence of different stages of Amp crystallization (Fig. 6a). Frequently, Amp is rich in inclusions, mainly constituted by Chl, Dol2, Di ±Ttn (e.g., Figs. 6a and 8b). Dol in microlithons varies from less frequent inequigranular fine- to medium-grained interlobate crystals (Dol1 + subgrains), to more common equigranular, fine-grained polygonal crystals (Dol2 new grains). In these domains, the S_2 foliation is marked by Dol1 and Dol2 SPO and sporadic Amp SPO (Fig. 6a). Dol1+Dol2 and Amp are often replaced by Cal3, which forms cryptocrystalline interstitial aggregate.

Although not frequent, relict S_1 is recognizable in isoclinal D_2 fold hinges. S_1 is generally defined by mineral layering consisting of alternating layers of Op+Chl±Srp, Amp, and Dol, respectively. Such D_2 folds generated a weak axial planar S_2 foliation mostly defined by re-oriented Dol2±Dol1 grains and Amp SPO (e.g., sample B11; Fig. 6b; see Fig. 4b for outcrop view).

The MH2 includes cm- to mm-sized clasts consisting of Amp and carbonates. These clasts are characterized by an internal foliation (S_i) (thin section B8, Tab. 1) defined by Amp-rich layers alternating with Dol1+Op±Dol2±Cal3-rich domains, all parallel to the external S_2 that is marked by Amp and Dol+Op SPO. S_i ($\sim S_e=S_2$) is here inferred to result from tectonic transposition of a previous fabric, probably composed of Op+Chl, Amp, Dol compositional layering (similar to S_1 of thin section B11). Frequently, clasts are boudinaged, with boudin neck filled with Di+Dol1+Dol2 (thin section B6, Tab. 1) fibrous aggregates; fibres have grown parallel to the extension direction during boudinage which is inferred to be syn-D_2 (see Tab. 2). Cpx is in equilibrium with kinked and elongated Dol1 porphyroblasts, which show evidences for dynamic recrystallization into Dol2 aggregates near the contact with the boudinaged clast.

MH2 locally embeds metasomatised dm- to m-sized blocks (Fig. 6c; see Fig. 4d for outcrop view; see thin sections B12 and E7; Tab. 1). These blocks have various size, shape and texture at the outcrop scale, as well as different fabrics in thin section. Mainly, metasomatised blocks have a granoblastic polygonal texture defined by Dol grains (Fig. 6c). The Dol-rich domains are equigranular, interlobate to polygonal, with Dol subgrains still dynamically deformed (i.e., undulose extinction), suggesting that recrystallization is not always complete. Amp-rich domains are randomly distributed and consist of fine- to medium-grained acicular, subhedral crystals. Aggregates of fibrous Amp+Chl±Tlc and Op grains surround some Dol2 aggregates, and Cal3 sporadically replaces Dol and Amp, also filling their fractures. Some clasts/blocks have a weakly foliated texture, with S_2 deformed by the D_3 phase, which produced gentle folds developing an incipient new foliation marked by Amp

Pre-Proof

crystals intersecting the S_2 foliation at high angle (incipient S_3 foliation; Fig. 6c), or shear structures evidenced by S-C shear bands and Amp/Dol sigmoid-shaped aggregates, as also observed at the outcrop scale. During D_3, Amp was not deforming and Cal3 likely started replacing Dol and Amp aggregates.

In most deformed domains, MH2 mainly consists of metasomatic disrupted levels that are cm- to dm-thick (Fig. 6d; thin sections B13A and B13B; Tab. 1). In these levels the S_2 foliation is defined by Chl+Op(±Cpx±Srp) layers alternating with Dol2+Cpx(±Dol1±Amp) domains. Relics of a S_1 compositional layering are locally recognizable, especially in less transposed, sigmoidal microlithons where Cpx is still aligned to S_1 planes (Fig. 6d). Amp is less abundant whereas Cpx relics are still present; Cpx is fine- to medium-grained, highly fractured, anhedral-subhedral and with a weak SPO along the S_1 and S_2 directions. The Cpx+Chl+Op association likely represents transposed portions of relict serpentinite clasts, and mark isoclinal D_2 fold hinges truncated by shear bands. Dol1 or Cpx sigmoids are diffused, with Cal3 filling strain caps and replacing Dol grains after D_2. Cal3 veins either are shear micro-veins or crosscut all the previous structures.

MH3

In different sites of the study area, MH3 type occurs sporadically and has a random distribution within the metasomatic horizon. MH3 includes coarse-grained Dol-rich sigmoidal domains, embedded within Amp-rich layers, and Ep-rich or carbonate-rich layers alternating with Amp domains (thin sections E8, H4, H5; Tab. 1).

Many coarse-grained Dol1 sigmoidal domains (> 1 cm long; Fig. 6e; thin section H5, Tab. 1; see Fig. 4f for outcrop view) are embedded within Amp-rich layers (almost 100% Amp) defining the S_2 foliation. Dol aggregates with sigmoidal shape (top to NNW shear sense) consist of inequigranular, interlobate Dol1 porphyroblasts frequently replaced by Amp and Cal, and associated with Fe-oxides/hydroxides. Dol2 neoblasts are commonly concentrated within the pressure shadows of Dol1 sigmoidal domains (Fig. 6e). Within the pressure shadows, possible relics of folded S_1 were observed and marked by fine-grained Amp (Fig. 6e).

Epidote-rich rocks occur as levels characterized by a particular massive texture, consisting of fine- to medium-grained granoblastic Ep+Amp±Cpx±Op surrounded by coarse-grained poikilitic Cal (Cal3 or Cal4).

Dol-Amp-rich rocks are characterized by Amp(+Cpx+Chl+Op)-rich layers, with continuous to spaced foliation defined by the SPO of Amp and Cpx, alternating with medium- to fine-grained (Dol1+Dol2)-rich layers. Cpx often forms σ-type mantled porphyroclasts (Fig. 6f). Dol-rich domains are characterized by polygonal Dol2 aggregates. Shear structures are present as Chl+Op S-C shear bands and Dol±Cpx sigmoidal aggregates. Locally, Cal3 ribbons mark the contact between Amp-rich and Dol-rich domains (Fig. 6f).

In summary, the MH is characterized by a pervasive foliation defined by mineralogical layering. This layering consists of Chl+Spl (Mag) domains alternating with Amp-rich and Dol-rich layers. Within Amp-rich and Dol-rich layers, minerals are attributed to various crystallization stages. Dol1 porphyroblasts crystallized during the D_1 phase and then recrystallized into Dol2 during the D_2 phase (Tab. 2). Amp is stable since the D_2 phase, while Ep and Cal3 are attributed to D_3 and post-D_3 phases. Chl+Mag domains are always stable.

Pre-Proof

MINERAL CHEMISTRY

Serpentine

The analysed serpentine (Figs. 7a and 7b; Tab. S1) was distinguished according to its texture: in massive (sample C1) and foliated (sample B1) serpentinite, Srp1 replacing Opx or inclusions in Cpx, Srp2 in foliation S_2, Srp3 filling veins (Tab. S1). The analysed Srp occurs both in fine-grained aggregates replacing mantle protolith phases, and in corona around Spl grains (probable former Pl) associated with Chl, mainly in massive serpentinites. Almost all serpentines have an Atg composition, with MgO ranging from 33.5 wt.% to 36.5 wt.% and SiO_2 from 40 wt.% to 44 wt.%. Serpentine from foliated serpentinite shows a more restricted MgO value range (Fig. 7a), and the highest FeO wt.% contents. No clear distinctive composition can be envisaged for serpentines growing on former Opx, on inclusions in Cpx, within foliation S_2, or in veins. Serpentine shows two different ranges of Al_2O_3, one including values of ca. 0-4 wt% Al_2O_3 and one projected to Al_2O_3 contents as high as > 12.00 wt%; this latter range, however, likely represents mixed analyses of Atg-Chl intergrowths (Tab. S1). Tschermak's exchange in Atg consists in the incorporation of Al through a substitution of Mg and Si cations by two Al cations, so that Al-contents in analysed, unmixed Atg are up to 4.0 a.p.f.u. (Fig. 7b; Tab. S1). The y(Atg) (=Al/8 in a.p.f.u., 116 O, see Tab. S1) ranges from 0.06 to 0.49 (excluding the Atg-Chl intergrowths analyses). Al-content in Atg as a geothermometer could provide an additional constraint of the P-T conditions for serpentinites in the study area (Padrón-Navarta et al., 2013; see discussion in §9.1).

Amphibole

The analysed amphibole (see Fig. 8 for textural features; Tab. S2) pertains to the group of Ca-amphiboles (Tr/Act) following the classifications of Leake et al. (1997, 2004). The content of Ca varies from 1.72 a.p.f.u. to 2.03 a.p.f.u., positively correlated with #Mg(Fe^{2+}) = Mg/(Mg+Fe^{2+}). Fe is almost all Fe^{2+} in C site with Mg, while Mn, Ti, Ni and Cr are lower than 0.4 wt.%. In massive serpentinite, Amp replacing Cpx is always Tr; in MH, Amp varies from Tr to Act, frequently showing compositional zonations with Tr cores and Act rims (Figs. 8a, 8b and 8d; Tab. S2).

Dolomite and calcite

The chemical composition of Dol (Fig. 7c; Tab. S3) is near the pure term, with few amounts of Fe^{2+} (0.04 a.p.f.u. to 0.19 a.p.f.u.), and the Mg being inversely correlated to Ca. In foliated serpentinites, Dol has relatively high values of Ca/Mg; there are no substantial compositional differences between Dol1 replacing zoned Mgs relics and Dol2 filling micro-veins that crosscut the serpentinite assemblage. In MH, Dol occurs in porphyroblasts (Dol1, e.g. Figs. 5e, 6e, 8a and 8d) and new grains (Dol2, e.g. Fig. 8c), in which chemical composition does not vary much; Mg slightly decreases in zoned Dol1 cores. Analysed Cal (Fig. 7c) belongs mostly to the MH, replacing Dol and Amp, filling fractures in Dol, Amp boudin necks and veins (Fig. 8). Their

Pre-Proof

chemical composition does not differ much from one to the others: Mg is very low (up to 0.08 a.p.f.u.), Ca ranges between 0.8 a.p.f.u. to 0.99 a.p.f.u., and the Ca:Mg ratio diverges a little by 1:1 because of very small substitutions of Mg and Fe^{2+} in the Ca site. In massive serpentinite, Cal occurs in micro-veins with an almost pure $CaCO_3$ composition.

Clinopyroxene

Almost all the analysed Cpx (Tab. S4) have a diopside-rich composition, with Wo values ranging between 47.5 and 50.5%. In massive serpentinite, some Cpx porphyroblasts are Di with some Fe-Mg exchange, e.g. Di porphyroblasts with Atg inclusions that have a slight minor amount of Si and Ca. The other Di crystals, both in massive serpentinite and in metasomatic rocks, have Ca ranges from 0.94 a.p.f.u. to 1.02 a.p.f.u., and Mg values between 0.81 a.p.f.u. and 0.96 a.p.f.u. In both lithologies Di is frequently replaced by Amp. In MH (MH2), Di often occurs as crypto-inclusions within Amp and Dol1, or within the disrupted level (Figs. 8a and 8b).

Chlorite

Within the analysed Chl crystals (Figs. 7d and 8; Tab. S5), Al ranges from 0.5 a.p.f.u. to 4.3 a.p.f.u. and Mg values between 7.2 a.p.f.u. and 10.3 a.p.f.u., with lower Al and higher Mg values in Chl pertaining to massive serpentinite. In MH, Chl (especially when associated to Mag) has small amounts of Cr (0.2-0.4 a.p.f.u.) and of Ni (up to 0.1 a.p.f.u.), suggesting that such chlorites might have inherited the composition of a former peridotite mineral rich in Ni (e.g., Ol) and Cr (e.g., Spl). Overall, the analysed chlorite is Clinochlore, however in massive serpentinite chlorite has a composition ranging between Penninite (when replacing Cpx or Opx) and Talc-chlorite (inclusions in Cpx). Thus, Chl within massive serpentinites is a Mg-Fe-rich (Al-poor) chlorite; in MH, Chl has a chemical composition between Fe-chlorite (“chamosite” end member) and Cr-chlorite, occurring mostly with Mag.

Spinel group minerals

The compositions of the analysed Spl (Tab. S6) are mainly magnetite. In serpentinites, Spl composition range from Al-Chr in relict cores, to Fe-Chr and Mag in the rims. The Al-Chr cores within Spl holly-leaf shaped crystals are interpreted as relict composition of mantle peridotite protolith spinels. In MH, Spl is mostly Mag, with 0.1-0.2 a.p.f.u. of Cr in magnetite at the rim of Fe-Chr relics.

RAMAN SPECTROSCOPY ON SERPENTINE MINERALS

The different serpentine polymorphs were characterized using micro-Raman spectroscopy at the University of Genova (Italy). Following previous study on this mineral group (e.g., Petriglieri et al., 2015), the Raman spectra of these minerals can be split into two main ranges: (i) low wavenumber spectral range (from 150 to

Pre-Proof

1100 cm^{-1}) and (ii) high wavenumber spectral range (from 3500 to 3800 cm^{-1}). The first range of the serpentine spectrum corresponds to the inner phonon modes of the lattice and to the Si-O_4 vibrations, while the second one, at higher wavenumbers, corresponds to the phonon modes assigned to the OH group (e.g., Auzende et al., 2004).

Micro-Raman spectra from three thin sections (e.g., Fig. 9; see Methods, §3.5) confirm that Atg is the most abundant species. Figure S3 shows and compares three reference Raman spectra for each serpentine polymorph. In agreement with Petriglieri et al. (2015), we exploit the OH spectral range for the identification of the different serpentine polymorphs. Indeed, the Raman spectra show the largest differences among the three species in this range (Fig. S3). For instance, Atg displays, in this spectral range, two main Raman peaks near to 3661 and 3692 cm^{-1}, Lz has two other major peaks near 3677 and 3698 cm^{-1} while Ctl has the most intense peak near 3694 and one minor peak (appearing as shoulder) near to 3685 (Fig. S3). At the low spectral range, Ctl and Lz are the same and the only difference can be found in the Atg spectrum showing a peak near to 1044 cm^{-1}.

CARBONATE STABLE OXYGEN AND CARBON ISOTOPE ANALYSES

The results of oxygen and carbon stable isotope analyses on carbonates from each LMO units, i.e. CSU (Cal lithons), CCU (Cal in serpentinite clast, Dol matrix and Cal vein), MH (MH1 Dol porphyroblasts) and metaophiolite basement (metaophicarbonate Cal vein), are shown in Figure 10 (see Fig. S2 and Tab. S7 for analytical sites and data). Cal oxygen and carbon isotopic composition in CSU shows values with average (n=4) $\delta^{18}O$ = +22.7‰ VSMOW (-7.9‰ VPDB) and $\delta^{13}C$ = -3.6‰ VPDB. Carbonates (Cal, Dol) in the CCU (BrFm1 type from Tartarotti et al., 2019) retain O and C stable isotope compositions that vary slightly upon the textural occurrence. Cal replacing the serpentinite clasts (n=4) has average $\delta^{18}O$ and $\delta^{13}C$ values of +17.1‰ VSMOW (-13.4‰ VPDB) and +2.1‰ VPDB, respectively. The matrix has a dynamically recrystallized Dol with average (n=4) $\delta^{18}O$ = +16.3‰ VSMOW (-14.1‰ VPDB) and $\delta^{13}C$ = +1.8‰ VPDB. Cal filling late veins that crosscut the Dol matrix (see Fig. S2) has average (n=4) $\delta^{18}O$ and $\delta^{13}C$ values of +17.5‰ VSMOW (-13.0‰ VPDB) and +1.3‰ VPDB, respectively. The porphyroblastic Dol (Cal <1%) analysed from the MH (MH1) has average values (n=7) of $\delta^{18}O$ = +14.4‰ VSMOW (-16.0‰ VPDB) and $\delta^{13}C$ = +0.7‰ VPDB. Cal sampled from an intrafolial vein within the metaophicarbonate (n=4) shows the lowest $\delta^{18}O$ values (average $\delta^{18}O$ = +9.8‰ VSMOW, -20.5‰ VPDB) and the highest $\delta^{13}C$ values (average $\delta^{13}C$ = +2.4‰ VPDB).

DISCUSSION

Structural and metamorphic evolution

In the metaophiolite sequence exposed in the high Champorcher valley, mesoscale and microscale techniques of structural geology implemented with microchemical analyses were used to unravel the complex tectono-metamorphic evolution of the MH and to infer a possible interpretation of its genesis and evolution.

Pre-Proof

The oldest structure recognized in the field is the S_1 foliation that is particularly clear within calcschists. S_1 in the calcschists developed through metamorphic recrystallization of sedimentary bedding (S_0) during the Alpine D_1 phase. In the metabreccias (i.e., the CCU), the oldest structure is represented by the clast-matrix contact. However, a probable older structure can be found inside serpentinite clasts exhibiting relict serpentine mesh texture developed during oceanic serpentinization (Tartarotti et al., 2019). The MH preserves, as oldest structures, the D_1 clastic texture, consisting of Amp-rich clasts embedded in a carbonate-rich matrix, and the S_1 foliation observed within D_2 isoclinal fold hinges (see Fig. 4b). Yet, the most prominent structure in the MH is the S_2 foliation, which is characterized by mineralogical layering commonly defined by layers of Dol±Cal (±Mag) alternating with layers of green Amp±Chl (±Mag). The recognition of structural relics as the D_1 clastic texture and the S_1 foliation in the MH suggests that the D_2 layering derives from tectonic transposition of a previous (already metasomatised?) rock consisting of carbonate-rich and mafic/ultramafic assemblages. In addition to this transposition effect, the D_2 deformation phase commonly produced boudinage and shearing of rock components as attested by the occurrence, in the MH and in the CCU, of sigmoid-shaped clasts and blocks.

In the whole study area, the S_2 foliation is crenulated and folded during the ductile D_3 phase, characterized by asymmetric, polyharmonic open D_3 folds (with mainly subhorizontal axial plane), without producing a new axial plane foliation/cleavage. Locally, interference patterns produced by D_2+D_3 phases are also observable. Only in CSU, the D_4 ductile phase is recognizable for the occurrence of domes-and-basins structures produced by wide m- to tens of m-scale folds with a subvertical axial plane, and m-scale S-C structures are an example of the ductile-brittle transition regime ($D_{4(5)}$ phase). During the last brittle $D_{5(6)}$ phase, different extensional fracture systems crosscut the previous ductile structures. Fractures are commonly filled with Cal or Srp within the metaophiolite basement, MH and CCU, while in calcschists fractures are filled with Qz and/or Cal.

Microstructural and petrographic observations performed in the studied rocks added several details to this complex deformation history, summarized as follows (see Tab. 2).

Pre-D_1: oceanic stage and inception of subduction. In serpentinites, this stage is inferred by the occurrence of mantle mineral and textural relics, i.e. relics of porphyroclastic mantle peridotite, including: *i)* porphyroblastic Cpx (Aug) and Spl eventually with Pl corona now replaced by Cr-rich Chl, as observed in Spl-Pl abyssal peridotites (e.g., Tartarotti et al., 2002; Seyler et al., 2007), and in southern Apennine ophiolites (e.g., Sansone et al., 2012); *ii)* bastite- and mesh-textured Srp on original Opx and Ol, respectively; *iii)* Al-Chr cores of the holly-leaf shaped Spl crystals; *iv)* Cpx porphyroblasts including Opx blebs (now serpentinized), as observed in melt impregnation textures typical of oceanic mantle-peridotites (e.g., Tartarotti et al., 2002; Seyler et al., 2007). Other structures attributable to the oceanic stage are represented by sedimentary serpentinite breccias preserved in the CCU (Tartarotti et al., 2017, 2019). As a matter of fact, in modern oceans serpentinite breccias have been observed since long time in strongly faulted submarine environments (e.g., in transform faults; Bonatti et al., 1974; at Iberia Abyssal Margin; Gibson et al., 1996). Oceanic ophicarbonates (i.e., serpentinites intersected by various types of carbonate-rich veins) likely developed already in the Jurassic ocean through syn-rift tectonic

Pre-Proof

denudation of lithospheric mantle and concurrent hydrothermal fluid circulation at the seafloor (Driesner, 1993; Tartarotti et al., 2017). The MH does not show any pre-D_1 textures.

D_1: prograde to HP metamorphic peak. In serpentinites, mantle Cpx recrystallized into Di. Mantle Spl (Al-Chr) recrystallized into Fe-Chr and Mag. Within foliated serpentinites, elongated Dol1 porphyroblasts are lineated to the S_2 foliation and include Mgs relict crystals (see Fig. 5c). This texture suggests that Mgs likely crystallised during the D_1 stage or even before, attesting that carbonation processes may have occurred during the oceanic evolution or during the inception of subduction (i.e., during the prograde stage).

In the MH, the oldest mineral phase, on the basis of textural evidence, is represented by Dol1 porphyroblasts, which are ascribed to the D_1 prograde stage (Tab. 2). A first generation of Amp1 (Tr) ("Amp1?" in Tab. 2) might have crystallized replacing Dol1 (see Figs. 5e and 8d). In MH2 we observed isoclinal D_2 folds marked by a mineralogical layering (i.e., S_1) consisting of Op+Chl±Srp layers alternating with Amp-rich and Dol-rich layers. We interpret this foliation (e.g., Figs. 4b and 6b) as possibly due to tectonic transposition of a previous compositional layering (i.e., S_0) or composite lithology (e.g., serpentinite clasts constituted by Srp+Mag embedded in a carbonate-rich matrix, i.e. serpentinite breccia; and/or metaophiolite basement - sedimentary cover contact) during the D_1 stage.

During the D_1 stage, the primary sedimentary bedding S_0 in the calcschists recrystallized into the S_1 foliation (e.g., Tartarotti et al., 2019), mainly consisting of a compositional layering less or more transposed and marked by the alternation of different mineral assemblages depending on the lithologies involved. The Cal-rich microlithons started to dynamically recrystallize and Lws crystals started to grow, while Wm1+Ep+Op films developed alternating with carbonate domains. In the micaschist intercalations within calcschists, S_1 was defined by Wm1+Qz1±Cld±Op±Ep and Grt likely began to crystallize as porphyroblast.

D_2: syn-HP metamorphic peak. This is the most pervasive Alpine ductile phase in the entire area, which produced the regional-scale foliation S_2, as axial planar to F_2 isoclinal folds and associated with the HP-LT metamorphic peak during deep subduction. This is inferred mainly on the basis of the mineral associations within the CSU, i.e. Grt+Cld (±Ph±Lws) (Tartarotti et al., 2019), as in the CCU, MH and serpentinites the mineral associations weakly constrain the peak metamorphic conditions. During this phase, the grain size of the studied lithologies decreased due to the dynamic recrystallization of coarse-grained porphyroblasts (e.g., Dol1 porphyroblasts recrystallized into Dol2 new grains; see Tab. 2), with the concomitant orientation of fabrics (strong SPO) and pervasive tectonic transposition of mineral or lithological domains, resulting in complex mineralogical or lithological layering. In metaophicarbonate the first two sets of veins (intrafolial veins and Di+Dol extensional veins) developed. Especially but not exclusively in the MH, a wide replacement of carbonates (Dol) by Amp2 (Act/Tr) developed along the S_2 planes. Di relics are often well preserved in the transposed layers, within Dol+Amp-rich microlithons alternating with Chl+Mag films (see Fig. 6d).

During D_2, boudinage within the MH produced truncated clasts with boudin necks filled by Dol1-2+Cpx(Di) fibres, elongated parallel to the extensional direction. In MH3, Tlc occurs in association with Chl and Cal within

Pre-Proof

Amp-rich layers embedding Dol sigmoid, and its crystallization has been likely favoured by the high availability of Mg (from Dol) and the presence of SiO_2-rich-fluids that reacted with Dol to produce Tlc+Cal (+CO_2).

In the calcschists, S_1 was pervasively transposed, developing the main S_2 defined by Cal2+Wm2+Qz2±Ttn±Op; in micaschists, Grt porphyroblasts reached their maximum development, associated with Cld, and S_2 was marked mainly by Wm2, Qz, Cld SPO (e.g., Tartarotti et al., 2019).

D_3: post-HP peak. This deformation stage produced large-scale structures that are difficult to identify at the micro-scale. During this phase Amp3 crystallised with its long dimension at high angle to S_2 (Fig. 8b). Amp crystallization resulted into an almost complete substitution of serpentine and carbonate phases. In all the lithologies, Cal3 crystallization is dominant within fractures and interstitial pores.

Post-D_3: retrograde path. During late stage, Cal, Amp ("Amp3/4?" in Tab. 2), Qz crystallized at the expenses of previous mineral assemblages and many shear structures developed in different lithologies (C- and C'-type shear bands), maybe starting even during previous stages (D_3?). In brittle exhumation regime, many tension gashes were filled by Cal or Qz (Tab. 2).

In order to better constrain qualitative stability fields for the mineral associations of the LMO in general, and for the MH in particular, the model proposed by Kerrick and Connolly (1998) for HP metaophicarbonates (Fig. 11) and a model by Padrón-Navarta et al. (2013) for Ca-bearing serpentinite from Zermatt-Saas (see Fig. 6 of Padrón-Navarta et al., 2013) were applied to our case study. Note that the stability fields from Kerrick and Connolly (1998) model are related to a closed-system, which is in contrast with the assumption of metasomatic reactions driven by externally-derived fluid, but the model is still applicable for the mineral associations considered in our case study. In Figure 11, the mineral paragenesis consisting of Dol(1-2)+Di+Atg(1-2)±Cal, observed in the MH rocks and serpentinites and attributed to the prograde (D_1) to peak (D_2) subduction-related conditions (see Tab. 2), would plot the studied rocks in the P-T stability field defined by temperatures below 550°C and pressures between 0.1-1.5 and 2.5-3.0 GPa (see green field in Fig. 11), as Brc and Fo lack in the LMO rocks. Subsequent Amp(Tr)+Cal+Atg+Dol assemblage (mainly stable from D_2 onwards) would fall in the field at lower pressures, between ca. 0.3-1.0 GPa and 0.6-1.5 GPa (see orange field in Fig. 11). Syn- to post-D_2 mineral phases, such as Atg2+Cal±Tlc assemblage were found in some MH samples (e.g., sample H5; Tab. 1), thus their field is below T ~350 °C and P ~1 GPa (see yellow field in Fig. 11). P-T stability fields could also be constrained by considering the geothermometer given by the Al-content in antigorite as y(Atg), which is sensitive to temperature in serpentinites with the assemblage Atg+Ol+Chl+fluid (Padrón-Navarta et al., 2013). Although Ol and Ti-Chu in our serpentinite samples were not observed, Ol could probably be a minor occurrence in Lake Miserin ophiolite as it is abundant in the nearest outcrops of the Mount Avic serpentinites (Dal Piaz et al., 2008; Fontana et al., 2015). The fluid saturated P-T pseudosection of Figure 6 from Padrón-Navarta et al. (2013) allows to consider the occurrence of tremolite and diopside in a serpentinite assemblage from the Zermatt-Saas zone. The analysed serpentines have y(Atg) that ranges between 0.06 and 0.49 (see §6.1 and Tab. S1), from which the upper T limit would result around 630°C and the upper P limit around 1.8 GPa,

Pre-Proof

where the Chl+Atg+Tr(±Ol) assemblage (field 2 in Fig. 6 of Padrón-Navarta et al., 2013) is stable. This P-T qualitative estimatation could be related to the syn- to post-D_2 assemblages that comprehend Amp (Tab. 2).

Inferred origin of the metasomatic horizon

Structural, petrographic and mineral chemistry data reveal that the MH is constituted by various types of rocks characterized by different fabrics and textures, i.e. brecciated, schistose, with disrupted levels, transposed clasts and massive blocks. Even in such distinguished types, the MH is, however, constituted by almost the same mineral assemblage occurring with different abundances, i.e. Dol+Cal+Tr/Act+Chl+Mag/Fe-Chr+Di (±Atg±Tlc±Ttn±Ilm; see Tabs. S1-S6). The mineral assemblages are distributed in mineralogical layering as a result of tectonic transposition and pervasive mineral reactions. The layering is overall characterized by Dol±Cal rich (±Tr/Act) domains vs. Tr/Act+Chl±Mag rich domains. Since this layering has been observed within D_1 structures (as S_1, see Figs. 4b and 6b, Tab. 2), the metasomatism along this horizon might have started well before the HP metamorphic peak, e.g. during the early-subduction stage of already coupled serpentinites (+ophicarbonates) and ultramafic breccias. The S_1 is the oldest structure recognised in the MH and is suggested to likely result from early tectonic transposition of either a former compositional layering S_0 or composite lithologies. The latter hypothesis is envisaged mostly given the lithological and structural features observed within CCU. In fact, composite lithologies such as the ultramafic metabreccias are interpreted as possible protoliths for the MH, as suggested by the presence within the MH, of both carbonate-rich domains, deformed clasts and metasomatised blocks quite comparable to those occurring in the CCU (see Figs. 4c and 4d). The Chl+Mag component within S_1 (see Figs. 6b and 6f) confirms that metasomatism affected a metaophicarbonate and/or serpentinite-bearing rocks (i.e., ultramafic metabreccias). Thus, the contact between serpentinites and the CCU represents the locus of the main metasomatic reactions occurred between the ophiolitic basement and the associated carbonate-rich deposits.

Thus, the following reactions are suggested to have led to the observed petrographic and structural features in the MH, at least beginning since the prograde D_1 phase. However we cannot rule out that metasomatism could have developed during oceanic extension both at an Oceanic Core Complex context (e.g., Boschi et al., 2006; Dick et al., 2008) or at an Ocean-Continent Transition zone (e.g., OCT; Manatschal and Müntener, 2009; Coltat et al., 2019), where peridotite and serpentinite carbonation may occur.

I. Dehydration processes. Seawater-derived and sediment-derived (i.e., CSU in this study) fluids could have penetrated along cracks and crustal normal faults as the slab bent near the trench (Lafay et al., 2013, and ref. therein). Then, dehydration of oceanic hydrous phases began at the onset of subduction (i.e., at shallow depth within the accretionary wedge). Partial dehydration (~2%) of lizardite/chrysotile by serpentinization into antigorite occurred gradually alongside a 1-2 % enrichment in silica (16 Lz/Ctl + 2 $SiO_{2(aq)}$ = Atg + H_2O; Dungan, 1979; Evans, 2004), until the temperature reached ca. 390°C where Atg is the only stable serpentine

(e.g., Deschamps et al., 2013; Lafay et al., 2013). Moreover, dehydration of subduction-related hydrous phases (e.g., lawsonite, zoisite, chloritoid, amphibole, chlorite, serpentine and talc in the hydrated oceanic lithosphere and sediments), can occur at almost any depth to ca. 150-200 km depending on individual slab geotherms and relatively to the thermal stability of each hydrous mineral (Schmidt and Poli, 1998), causing the circulation of aqueous, silica-rich fluids at different structural levels. As water is generally available in a subduction system and not all of the H_2O dehydrated is recycled into the mantle wedge (Deschamps et al., 2013), some portions of the dehydrated water likely remain and is transported at shallower levels through fluid flux within the subducting plates and along plate interfaces (Bebout, 2012; Angiboust et al., 2014; Jaeckel et al., 2018 and ref. therein), then allowing circulation of fluids through the whole LMO sequence. Hence, the following mineral reactions (II- decarbonation and III- carbonation; see below) could have occurred within the serpentinite basement and metasediments (particularly CCU) interface to produce the highly metasomatised rocks.

II. Decarbonation reactions had likely taken place in the MH, as testified by the common occurrence of Amp (Tr/Act±Cpx) replacing carbonate-rich domains, especially Dol, in the CCU carbonate matrices and in metaophicarbonate veins (see Figs. 5e, 6a, 6c, 8c and 8d; Tab. 2). Decarbonation is enhanced when carbonate-bearing rocks are infiltrated by H_2O- SiO_2-rich fluids released by serpentinites and/or calcschists (Gorman et al., 2006), driving silicates precipitation in veins or replacing Cal/Dol, e.g. by the reaction: $CaMg(CO_3)_2 + CaCO_3 + H_2O + SiO_{2(aq)} \rightarrow Ca_2Mg_5Si_8O_{22}(OH)_2 \pm CaMgSi_2O_6 + CO_2$ [Dol + Cal + H_2O + $SiO_{2(aq)}$ → Tr ± Di + CO_2] [9.1] (Deer et al., 1992; Scambelluri et al., 2016).

In the CSU, decarbonation is less extensive with respect to the LMO units, as also evaluated in other Western Alps metasedimentary suites (e.g., Bebout, 2012 and ref. therein). In fact, devolatilization is more extensive where fluids can more easily and continually flow and fluid fluxes are enhanced, i.e. along mélange zones and discontinuities such as lithological contacts where shear strain is high (i.e., in the slab and mantle-wedge interface; see Bebout, 2012). In the MH, many structures attest for a shear deformation, mostly within MH3 (see Figs. 4f, 6e and 6f). Thus, the LMO setting was probably favourable for the decarbonation reactions to occur extensively along the basement-sediment cover contact, starting from the D_1 phase to the post HP-peak D_3 phase (see Tab. 2).

III. Carbonation of silicates, in particular serpentine both in the basement and in the CCU clasts/blocks, and/or carbonate-veining allowed the (re-)sequestration of CO_2 released by decarbonation reactions, e.g. through Dol and Cal (±Mgs) replacement of Srp, Cpx or Amp (see Figs. 5c, 5e, 5f, 6a, 6c and 8c). This process might have begun at shallow levels (Kelemen and Hirth, 2012) and continued further up to the HP-peak (Scambelluri et al., 2016; Piccoli et al., 2016, 2018) and then during late exhumation stages (see Dol1, Dol2, Mgs and Cal3 in Tab. 2), as long as the circulating fluids equilibrated with carbonates at depth become oversaturated in $CaCO_3$ when decompressing (Kelemen and Manning, 2015; Piccoli et al., 2018). Multiple carbonation events at different temperature conditions could be testified by the chemical zonations within Dol and Mgs (see Fig. S4 and Tab. S3). Moreover, carbonation reactions release back H_2O, e.g. as expressed by the following reaction for

carbonation of serpentine: $Mg_3Si_2O_5(OH)_4 + CO_2$ (+ Ca) → $CaMg(CO_3)_2 + CaCO_3 + H_2O$ [Srp + CO_2 (+ Ca) → Dol + Cal + H_2O] [9.2].

Reactions 9.1 (decarbonation) and 9.2 (carbonation) might have interchanged producing multiple fluid flow pulses within the basement-sediment permeable interface, as suggested by the extremely heterogeneous nature of the MH rock types. In basement serpentinites the decarbonation and carbonation products are uncommon (based on field and petrographic observations; see §4 and Tab.1). Thus, as Piccoli et al. (2018) suggested, this may indicate that serpentinites were either not reactive or of low permeability, with fluids unable to penetrate them. Within CCU metabreccias decarbonation and carbonation reactions led to the abundant formation of Dol+Cal+Amp±Cpx-rich domains (both within serpentinite clasts and matrices), this possibly indicating a reactivity of CCU serpentinite clasts to C-rich fluids. Thus, the hypothesis that basement serpentinites acted as poorly permeable unit contrasting with the highly permeable metasedimentary cover is more envisaged also for this case study. In this scenario, the permeability contrast between serpentinite basement and CCU could have allowed fluid flow along their interface (e.g., Bebout and Penninston-Dorland, 2016) and consequently behaved as a preferential channel for fluid circulation where the metasomatic reaction fronts were probably asymmetric/heterogeneous (see Piccoli et al., 2018 and ref. therein), in some extent depending on the textural features of the MH protoliths. Then, this kind of channel could have acted also as a major shear zone (e.g., Angiboust et al., 2014), where the ductile deformation was also assisted and imbrication enhanced by the flow of fluids (e.g., Cartwright and Barnicoat, 1999; Gerya et al., 2002; Angiboust et al., 2012; Zheng et al., 2013; Fagereng and den Hartog, 2017; Prigent et al., 2018, Hirauchi et al., 2020). The transitional nature of the MH contact with CCU also records the effects of channelling fluid-driven reactions along the contrasting permeability interface between the two protoliths. The MH variation in thickness (Fig. 3) is more likely related to at least the asymmetric ductile deformation during D_3 and D_4, even if MH could have developed and reached the maximum thickness during D_2 metamorphic peak, when decarbonation and carbonation reactions acted extensively.

To summarize, the development of MH was likely driven by mixed COH-rich fluids circulation along the contact between the subducting serpentinite basement and metasediments, which is interpreted as a favourable interface for fluid flow channelization (e.g., Cartwright and Barnicoat, 1999; Bebout, 2012 and ref. therein; Scambelluri et al., 2016; Piccoli et al., 2018 and ref. therein). Serpentinites play a crucial role in the subduction-zone carbon cycling (e.g., Scambelluri et al., 2016). On one hand de-serpentinization released H_2O-rich fluids and supplied water to adjacent carbonate-bearing rocks (CCU metabreccias), promoting C mobility via enhanced carbonate dissolution due to decarbonation reactions. On the other hand, reaction of serpentinites with COH-fluids led to the replacement of silicate minerals by carbonates, thus sequestering C from the circulating aqueous-carbonic fluids through enhanced carbonation. Moreover, SiO_2-rich fluids could have been supplied by the overlying CSU (or even slices of gneissic rocks from the Austroalpine domain), thus allowing the crystallization of significant amounts of Amp (Tr/Act) replacing carbonate domains, and rarely also Cpx (Di* in Tab. 2) precipitation in extensional veins, within the MH.

Pre-Proof

Oxygen and carbon stable isotope constraints on MH genesis

Oxygen and carbon isotopic compositions analysed from carbonates belonging to LMO units (see Fig. 10 and Table S7) provide preliminary constraints on the formation of the MH as the isotopic signature can potentially be used as fluid sources tracker (e.g., Driesner, 1993; Cartwright and Barnicoat, 1999; Cook-Kollars et al., 2014; Collins et al., 2015; Scambelluri et al., 2016). Cathodoluminescence analyses (Fig. S2) on CCU and CSU samples show that the $\delta^{18}O$ and $\delta^{13}C$ values obtained from their carbonates represent an average between at least two generations each of calcite and dolomite, and this can be extended also to carbonates from the other two units by petrographical analogies. Taking this into account, the majority of $\delta^{13}C$ values in both calcite and dolomite from the metaophiolite basement, MH and CCU (Table S7) retain the carbon signature of Jurassic/Cretaceous marine pristine (e.g., not altered by diagenesis) carbonates (approximately 0 to +3‰ VPDB, e.g. Veizer et al., 1999) and also of carbonates precipitated during oceanic alteration (from -2 to +3‰ VPDB, e.g. Collins et al., 2015 and ref. therein). This suggests that the analysed carbonates precipitated from fluids in which the dissolved inorganic carbon (DIC) derived from the dissolution of marine carbonate deposits. The carbon signature of the MH is inherited from its protoliths (i.e., metaophiolite basement and CCU), showing only a slight shift to lower values that has been observed to be likely due to the decarbonation reactions (see §9.2) acted during equilibration with fluids derived from the CSU (e.g., Cook-Kollars et al., 2014; Collins et al., 2015). Calcite $\delta^{13}C$ values in the CSU are more negative, as for other calcschist analysed in the Zermatt-Saas zone (see Fig. 10a). This can be explained by exchange during metamorphism with a certain amount of reduced C from graphite of organic origin in the CSU protolith marine pelites and/or carbonates, which mainly depends on the calcite/graphite abundance ratio (e.g., Busigny et al., 2003; Bebout, 2012; Bebout et al., 2013; Cook-Kollars et al., 2014). Moreover, CSU calcites have oxygen isotopic composition (average $\delta^{18}O$ values +22.7‰ VSMOW; Fig. 10) that fits within the calcite $\delta^{18}O$ value range of the Zermatt-Saas calcareous schists from Cartwright and Barnicoat (1999). This indicates that the CSU oxygen isotope compositions have been hardly altered by interaction with fluids during metamorphism (e.g., Cartwright and Barnicoat, 1999). Thus, the CSU protoliths were likely constituted by both pelites (marine pelitic rocks display $\delta^{18}O$ values = +12-17‰ VSMOW; Hoefs, 2009; Cartwright and Barnicoat, 1999; low-grade metapelites have $\delta^{18}O$ = +15-18‰ VSMOW, e.g. Hoefs, 2009) and marine carbonate deposits ($\delta^{18}O$ = +28-30‰ VSMOW, e.g. Hoefs, 2009).

The $\delta^{18}O$ values for all the LMO units are significantly lower with respect to the typical range of marine carbonates (between +28 and +30‰ VSMOW, e.g. Hoefs, 2009; $\delta^{18}O$ values of Jurassic-Cretaceous pristine marine carbonates; cf. Veizer et al., 1999), increasing gradually from the metaophicarbonate to the CSU (see Fig. 10b). Thus, this oxygen signature records fluid-rock exchanges during subduction temperatures (up to peak T = 350-550°C for LMO) and could reflect either equilibration with silicates in the metapelites (e.g., Busigny et al., 2003; Cook-Kollars et al., 2014) or infiltration by H_2O-rich fluids externally derived from dehydration of ultramafic and mafic rocks such as serpentinites (e.g., Jaeckel et al., 2018 and references therein). Calculations

of the oxygen isotope compositions of aqueous fluids in equilibrium with LMO carbonates at the estimated temperatures of 350, 400 and 550 °C (using fractionation factors from Golyshev et al., 1981 and Zheng, 1999; see Tab. S7) yield values of 5.2-10.6‰ VSMOW in the metaophicarbonate that gradually increase through the CSU, reaching 18.2-23.6‰ VSMOW. Calculated H_2O-fluid $\delta^{18}O$ values follow the same positive trend toward the CSU, suggesting that H_2O-fluids equilibrated with LMO carbonates might have changed their isotopic composition by mixing with fluids from external reservoirs.

The $\delta^{18}O$ and $\delta^{13}C$ values of carbonates within the MH and CCU lie between those of the metaophicarbonate and of the CSU (see Fig. 10), thus we consider this array another inference for the mixing of H_2O-rich fluids from the dehydrating metaophiolite basement with fluids evolved in the overlying CSU within their interface (e.g., Bebout, 2012; Collins et al., 2015). The oxygen and carbon isotopic signatures in the MH (see Fig. 10a) support the hypothesis that fluids channelization was intense and decarbonation-carbonation reactions were enhanced at its boundaries (especially near the contact with the metaophiolite basement), thus allowing mixing of fluids and oxygen isotope composition. This interpretation is consistent with an open-system or limited open-system behaviour envisaged by Cook-Kollars et al. (2014). The open-system model proposed by Cook-Kollars et al. (2014) is in support of carbonate-rich rocks flushed by H_2O-rich fluid from underlying subducting oceanic lithosphere, though in general an open-system involves infiltration by fluids from external sources (e.g., Collins et al., 2015; Scambelluri et al., 2016; Jaeckel et al., 2018; Piccoli et al., 2018; Cannaò et al., 2020; Menzel et al., 2020).

Geodynamic setting of fluid-rock interaction

The MH likely started its tectono-metamorphic formation and evolution from early Alpine subduction and continued at least up to the HP peak metamorphic conditions, as the product of multiple fluid-rock interactions along the serpentinite-metacarbonate rocks interface. Figure 12 summarizes the principal aspects of the MH geodynamic setting and shows details of the metamorphic fluid pathways all over the LMO sequence that are consistent with the structural, petrological and geochemical investigations. The metaophiolite basement and the CCU developed during the oceanic stage and coupled with post-extensional, accretionary prism deposits (i.e., CSU) at the inception of subduction (Fig. 12a), then they consequently experienced the same prograde path during subduction until the P-T peak conditions (Fig. 12b).

During the Jurassic extension of the Tethyan ocean (or Ligurian-Piedmont ocean), first carbonation processes may have been driven by hydrothermal activity within the ultramafic basement with the precipitation of minor Cal during serpentinization (e.g., Grozeva et al., 2017; Alt et al., 2018) and the CCU heterogeneous block-in-matrix deposits formed on the seafloor through mass transport processes and turbidite sedimentation related to exhumation of mantle rocks (Tartarotti et al., 2017, 2019). Metasomatism in pre-Alpine oceanic realm can likely took place along discharge zones where the sub-oceanic mantle is exposed, e.g. at the Oceanic Core Complexes (OCC) and in slow- or ultraslow-spreading ridge segments. In these settings, pervasive Tlc-Amp-Chl

Pre-Proof

metasomatism in the mafic and ultramafic rocks is localized in high strain zones, such as along detachment faults (e.g., Dick et al., 2008; Festa et al., 2015), and where hydrothermal mineralizations occur (e.g., Boschi et al., 2006; Escartín et al., 2017; Alt et al., 2018). In our case study, however, Tlc is very scarce or absent. At the onset of subduction, metasediments and serpentinite began to dehydrate and produced Mg- and SiO_2-bearing H_2O-rich fluids due to compaction and increasing metamorphic grade, thus starting fluids circulation within the subducting slab and accretionary prism. Infiltration by CO_2-rich fluids, derived from dissolution of organic carbon- and carbonate-bearing metasediments that increases the X_{CO2} of fluids (Menzel et al., 2018), allowed the Mgs/Dol crystallization within serpentinites and Cal replacement by Dol within CCU carbonate-rich matrices, mostly near the principal Mg- source, i.e. the serpentinite basement. At the same time, the mixing of Mg- H_2O- and SiO_2-rich fluids within the serpentinite-metasediments interface led to decarbonation reactions, the product of which was an intense replacement of carbonate-rich domains (i.e., CCU matrices) by silicate phases, i.e. Amp (Tr/Act) ±Cpx (Di), or silicates veining. Decarbonation reaction released back CO_2 (±Ca/Mg) within the aqueous fluids, shifting the fluid composition to more mixed COH-fluid with dissolved Ca/Mg (e.g., Scambelluri et al., 2016), which then could precipitate carbonates within veins and carbonatize the serpentinite domains (i.e., CCU clasts and metaophicarbonates). The aqueous fluids could infiltrate almost continuously into the system until the HP metamorphic peak (D_2 phase, Figs. 12b and 12d), as dehydration reactions occurred up to deeper structural levels (Schmidt and Poli, 1998) and H_2O-rich fluids could be channelized along the basement-metasediments interface (see Figs. 12c and 12d). Thus, carbonation and decarbonation reactions continued to be triggered by mixed COH-fluids at least up to D_2 phase (e.g., Kerrick and Connolly, 1998; Scambelluri et al., 2016), where the MH reached the maximum thickness (Fig. 12d). At this stage of the MH tectono-metamorphic evolution, almost complete carbonation of serpentinite domains, i.e. transposed and deformed clasts, and decarbonation of Dol+Cal domains accompanied by pervasive Amp replacement wherever possible, i.e. in matrices and veins, were concentrated at the metaophiolite basement and CCU interface, where fluids were channelized and mixed.

CONCLUSIONS

Mesoscale and microscale structural analyses implemented with petrological and geochemical data enabled to accomplish detailed inferences of the tectono-metamorphic evolution of the MH and to provide a possible interpretation of its genesis. The MH is a cm- to m-thick metasomatic horizon sealing the contact between the metaophiolite basement and the overlying metasedimentary sequence in the LMO (Zermatt-Saas Zone), characterized by the alternation of Dol±Cal (±Amp) rich domains and Amp+Chl (±Mag) rich domains. The complex interplay between mixed fluid (i.e., COH-fluid) and enhanced deformation within the metaophiolite basement-metasediments interface built up the MH intricate fabric and texture, from block-in-matrix to layered, toward the HP metamorphic peak of the Alpine subduction (and likely also during exhumation). The principal

Pre-Proof

processes that mostly acted to develop the MH were: *i*) deformation with a strong shear component within a rock assemblage characterised by contrasting competence of clasts and matrix; *ii*) chemical reactions such as decarbonation and carbonation that in turn produced a pervasive replacement of carbonate-rich domains by Amp (±Cpx) and of serpentinite domains by Dol+Cal within its protoliths (i.e., metaophiolite basement and CCU), also through the mixing with sediments-derived SiO_2-rich fluids supplied from the CSU. Serpentinites were fundamental for the subduction-zone deep carbon cycling, as de-serpentinization released H_2O-rich fluids to adjacent carbonate-bearing rocks (CCU metabreccias) and thus promoted C mobility via enhanced carbonate dissolution - decarbonation reactions. At the same time, reaction of serpentinites with mixed COH-fluids led to the replacement of silicate minerals by carbonates, thus re-sequestering C from the circulating aqueous-carbonic fluids via enhanced carbonation reactions. The oxygen and carbon isotopic composition of the whole LMO sequence allowed providing additional constraints on the fluids sources and allowed inferring an open-system scenario, accounting for rocks interaction with externally-derived fluids of hybrid serpentinite-CSU compositions. Thus, the MH represents a fossilized channel for focussed fluid flow in a subduction setting, where deformation-driven fluid-rock interaction was favoured and produced a significant minero-chemical alteration of adjacent rocks, especially the more permeable CCU broken formations.

Further studies to accomplish are bulk-rock major and trace element analyses of protolith rocks (i.e., serpentinite and ultramafic metabreccia) and metasomatic rocks, with the purpose of evaluating the gains and losses in element concentrations during metasomatism (decarbonation/carbonation) and dehydration (e.g., Angiboust et al., 2014).

ACKNOWLEDGEMENTS

Data presented in this paper and supporting our conclusions are all original and are displayed in figures and tables. The Editors Alessandra Montanini and José Alberto Padrón-Navarta are kindly thanked for the editorial handling, as well as Curzio Malinverno for the thin section manufacture, Andrea Risplendente for the EMPA analyses and Monica Dapiaggi for assistance with the XRD analyses. The manuscript greatly benefits from the thorough and constructive suggestions of Samuel Angiboust and an anonymous reviewer. Grants to P.T. received from the University of Milano (PSR2018_DZANONI) entitled to Davide Zanoni of the University of Milano, Department of Earth Sciences.

REFERENCES

Alt J., Crispini L., Gaggero L., Levine D., Lavagnino G., Shanks P. and Gulbransen C., 2018. Normal faulting and evolution of fluid discharge in a Jurassic seafloor ultramafic-hosted hydrothermal system. Geology, 46 (6): 523-526. https://doi.org/10.1130/G40287.1

Pre-Proof

Angiboust S., Agard P., Jolivet L. and Beyssac O., 2009. The Zermatt-Saas ophiolite: the largest (60-km wide) and deepest (c. 70–80 km) continuous slice of oceanic lithosphere detached from a subduction zone? Terra Nova, 21: 171-180. https://doi.org/10.1111/j.1365-3121.2009.00870.x

Angiboust S., Agard P., Raimbourg H., Yamato P. and Huet B., 2011. Subduction interface processes recorded by eclogite-facies shear zones (Monviso, W. Alps). Lithos, 127 (1-2): 222-238. https://doi.org/10.1016/j.lithos.2011.09.004

Angiboust S., Pettke T., De Hoog J.C., Caron B. and Oncken O., 2014. Channelized fluid flow and eclogite-facies metasomatism along the subduction shear zone. J. Petrol., 55 (5): 883-916. https://doi.org/10.1093/petrology/egu010

Angiboust S., Wolf S., Burov E., Agard P. and Yamato P., 2012. Effect of fluid circulation on subduction interface tectonic processes: Insights from thermo-mechanical numerical modelling. Earth Planet. Sci. Lett., (357-358): 238-248. https://doi.org/10.1016/j.epsl.2012.09.012

Angiboust S., Yamato P., Hertgen S., Hyppolito T., Bebout G.E. and Morales L., 2017. Fluid pathways and high-P metasomatism in a subducted continental slice (Mt. Emilius klippe, W. Alps). J. Metamorph. Geol., 35 (5): 471-492. https://doi.org/10.1111/jmg.12241

Auzende A., Daniel I., Reynard B., Lemaire C. and Guyot F., 2004. High-pressure behaviour of serpentine minerals: a Raman spectroscopic study. Phys. Chem. Miner., 31: 269-277. https://doi.org/10.1007/s00269-004-0384-0

Balestro G., Festa A., Borghi A., Castelli D., Gattiglio M. and Tartarotti P., 2018. Role of Late Jurassic intra-oceanic structural inheritance in the Alpine tectonic evolution of the Monviso meta-ophiolite Complex (Western Alps). Geol. Mag., 155 (2): 233-249. https://doi.org/10.1017/S0016756817000553

Balestro G., Festa A., Dilek Y. and Tartarotti P., 2015. Pre-Alpine extensional tectonics of a peridotite-localized oceanic core complex in the Late Jurassic, high-pressure Monviso ophiolite (Western Alps). Episodes, 38: 266-282. https://doi.org/10.18814/epiiugs/2015/v38i4/82421

Bearth P., 1967. Die Ophiolithe der Zone von Zermatt-Saas Fee. Beitr. Geol. Karte Schweiz (NF), 132, 130 pp.

Bearth P. and Schwander H., 1981. The post-Triassic sediments of the ophiolite zone of Zermatt-Saas Fee and the associated manganese mineralisations. Eclogae Geol. Helv., 74: 189-205.

Bebout G.E., 2012. Metasomatism in subduction zones of oceanic slabs, mantle wedges, and the slab-mantle interface. In: Harlov D. and Austrheim H. (Ed.). Metasomatism and Metamorphism: The Role of Fluids in Crustal and Upper Mantle Processes, Lect. Notes Earth Syst. Sci. Berlin, Heidelberg, Springer, p. 289-349. https://doi.org/10.1007/978-3-642-28394-9_9

Bebout G.E., Agard P., Kobayashi K., Moriguti T. and Nakamura E., 2013. Devolatilization history and trace element mobility in deeply subducted sedimentary rocks: Evidence from Western Alps HP/UHP suites. Chem. Geol., 342: 1-20. https://doi.org/10.1016/j.chemgeo.2013.01.009

Bebout G.E. and Barton M.D., 1993. Metasomatism during subduction: products and possible paths in the Catalina Schist, California. Chem. Geol., 108 (1-4): 61-92. https://doi.org/10.1016/0009-2541(93)90318-D

Bebout G.E. and Barton M.D., 2002. Tectonic and metasomatic mixing in a high-T, subduction-zone mélange – insights into the geochemical evolution of the slab-mantle interface. Chem. Geol., 187: 79-106. https://doi.org/10.1016/S0009-2541(02)00019-0

Pre-Proof

Bebout G.E. and Penniston-Dorland S.C., 2016. Fluid and mass transfer at subduction interfaces - the field metamorphic record. Lithos, 240: 228-258. https://doi.org/10.1016/j.lithos.2015.10.007

Beltrando M., Manatschal G., Mohn G., Dal Piaz G.V., Vitale Brovarone A. and Masini E., 2014. Recognizing remnants of magma-poor rifted margins in high-pressure orogenic belts: The Alpine case study. Earth-Sci. Rev., 131: 88-115. https://doi.org/10.1016/j.earscirev.2014.01.001

Bigi G., Castellarin A., Coli M., Dal Piaz G.V., Sartori R., Scandone P. and Vai G.B., 1990. Structural model of Italy 1:50'000, Sheet 1. Progetto Geodinamica, CNR, SELCA, Firenze.

Bill M., O'Dogherty L., Guex J., Baumgartner P.O. and Masson H., 2001. Radiolarite ages in Alpine-Mediterranean ophiolites: constraints on the oceanic spreading and the Tethys-Atlantic connection. Geol. Soc. Am. Bull., 113: 129-143. https://doi.org/10.1130/0016-7606(2001)113<0129:RAIAMO>2.0.CO;2

Bonatti E., Emiliani C., Ferrara G., Honnorez J. and Rydell H., 1974. Ultramafic-carbonate breccias from the equatorial Mid Atlantic Ridge. Marine Geology, 16: 83-102.

Boschi C., Früh-Green G.L., Delacour A., Karson J.A. and Kelley D.S., 2006. Mass transfer and fluid flow during detachment faulting and development of an oceanic core complex, Atlantis Massif (MAR 30°N). Geochem. Geophys. Geosyst., 7: Q01004. https://doi.org/10.1029/2005GC001074

Bucher K., Fazis Y., De Capitani C. and Grapes R., 2005. Blueschists, eclogites, and decompression assemblages of the Zermatt-Saas ophiolite: High-pressure metamorphism of subducted Tethys lithosphere. Am. Mineral., 90: 821-835. https://doi.org/10.2138/am.2005.1718

Busigny V., Cartigny P., Philippot P., Ader M. and Javoy M., 2003. Massive recycling of nitrogen and other fluid-mobile elements (K, Rb, Cs, H) in a cold slab environment: evidence from HP to UHP oceanic metasediments of the Schistes Lustrés nappe (western Alps, Europe). Earth Planet. Sci. Lett., 215 (1-2): 27-42. https://doi.org/10.1016/S0012-821X(03)00453-9

Cannaò E., Scambelluri M., Bebout G.E., Agostini S., Pettke T., Godard M. and Crispini L., 2020. Ophicarbonate evolution from seafloor to subduction and implications for deep-Earth C cycling. Chem. Geol., 546: 119626. https://doi.org/10.1016/j.chemgeo.2020.119626

Cartwright I. and Barnicoat A.C., 1999. Stable isotope geochemistry of Alpine ophiolites: a window to ocean-floor hydrothermal alteration and constraints on fluid-rock interaction during high-pressure metamorphism. Int. J. Earth Sci., 88 (2): 219-235. https://doi.org/10.1007/s005310050261

Collins N.C., Bebout G.E., Angiboust S., Agard P., Scambelluri M., Crispini L. and John T., 2015. Subduction zone metamorphic pathway for deep carbon cycling: II. Evidence from HP/UHP metabasaltic rocks and ophicarbonate. Chem. Geol., 412: 132-150. https://doi.org/10.1016/j.chemgeo.2015.06.012

Coltat R., Boulvais P., Branquet Y., Collot J., Epin M.E. and Manatschal G., 2019. Syntectonic carbonation during synmagmatic mantle exhumation at an ocean-continent transition. Geology, 47 (2): 183-186. https://doi.org/10.1130/G45530.1

Cook-Kollars J., Bebout G.E., Collins N.C., Angiboust S. and Agard P., 2014. Subduction zone metamorphic pathway for deep carbon cycling: I. Evidence from HP/UHP metasedimentary rocks, Italian Alps. Chem. Geol., 386: 31-48. https://doi.org/10.1016/j.chemgeo.2014.07.013

Dal Piaz G.V., 1965. La formazione mesozoica dei calcescisti con pietre verdi fra la Valsesia e la Valtournanche ed i suoi rapporti con il ricoprimento Monte Rosa e con la Zona Sesia-Lanzo. Boll. Soc. Geol. It., 84: 67-104.

Pre-Proof

Dal Piaz G.V., 1999. The Austroalpine-Piedmont nappe stack and the puzzle of Alpine Tethys. In Third workshop on alpine geology, Biella-Oropa 1997; Gosso, G., Jadoul, F., Sella, M., Spalla, M.I. Eds. Mem. Sci. Geol., Roma, 51: 155-176.

Dal Piaz G.V., 2001. History of tectonic interpretations of the Alps. J. Geodynamics, 32: 99-114. https://doi.org/10.1016/S0264-3707(01)00019-9

Dal Piaz G.V. and Ernst W.G, 1978. Areal geology and petrology of eclogites and associated metabasites of the Piemonte Ophiolite Nappe, Breuil-St. Jacques area, Italian Western Alps. Tectonophysics, 51: 99-126. https://doi.org/10.1016/0040-1951(78)90053-7

Dal Piaz G.V., Gianotti F., Monopoli B., Pennacchioni G., Tartarotti P. and Schiavo A., 2008. Note Illustrative della Carta Geologica d'Italia alla scala 1:50.000, Foglio 91 Chatillon. ISPRA, Servizio Geologico d'Italia, Realizz. Regione Autonoma Valle d'Aosta, 152 pp.

Dal Piaz G.V. and Nervo R., 1971. Il lembo di ricoprimento del Glacier-Rafray (Dent Blanche s.l.). Boll. Soc. Geol. Ital., 90: 401-414.

Deer W.A., Howie R.A. and Zussman J., 1992. An Introduction to the Rock-Forming Minerals. Second Edition. Longman Group UK Limited, London, 696 pp.

Deschamps F., Godard M., Guillot S. and Hattori K., 2013. Geochemistry of subduction zone serpentinites: A review. Lithos, 178: 96-127. https://doi.org/10.1016/j.lithos.2013.05.019

Dick H.J.B., Tivey M.A. and Tucholke B.E., 2008. Plutonic foundation of a slow-spreading ridge segment: Oceanic core complex at Kane Megamullion, 23°30′N, 45°20′W. Geochem. Geophys. Geosyst., 9: Q05014. https://doi.org/10.1029/2007GC001645

Dickson J.A.D., 1966. Carbonate identification and genesis as revealed by staining. J. Sediment. Petrol., 36: 491-505. https://doi.org/10.1306/74D714F6-2B21-11D7-8648000102C1865D

Driesner T., 1993. Aspects of petrographical, structural and stable isotope geochemical evolution of ophicarbonate breccias from ocean floor to subduction and uplift; an example from Chatillon, Middle Aosta Valley, Italian Alps. Schweiz. Mineral. Petrogr. Mitt., 73: 69-84.

Dungan M., 1979. A microprobe study of antigorite and some serpentine pseudomorphs. Can. Mineral., 17: 771-784.

Ernst W.G. and Dal Piaz G.V., 1978. Mineral parageneses of eclogitic rocks and related mafic schists of Piemonte ophiolite nappe, Breuil-St-Jacques Area, Italian Western Alps. Am. Mineral., 63: 621-640.

Escartín J., Mével C., Petersen S., Bonnemains D., Cannat M., Andreani M., Augustin N., Bezos A. et al., 2017. Tectonic structure, evolution, and the nature of oceanic core complexes and their detachment fault zones (13°20'N and13°30'N, Mid Atlantic Ridge). Geochem. Geophys. Geosyst., 18: 1451-1482. https://doi.org/10.1002/2016GC006775

Evans B.W., 2004. The serpentinite multisystem revisited: chrysotile is metastable. Int. Geol. Rev., 46: 479-506. https://doi.org/10.2747/0020-6814.46.6.479

Fagereng Å. and den Hartog S.A., 2017. Subduction megathrust creep governed by pressure solution and frictional–viscous flow. Nat. Geosci., 10 (1): 51-57. https://doi.org/10.1038/ngeo2857

Festa A., Balestro G., Dilek Y. and Tartarotti P., 2015. A Jurassic oceanic core complex in the high-pressure Monviso ophiolite (western Alps, NW Italy). Lithosphere, 7 (6): 646-652. https://doi.org/10.1130/L458.1

Pre-Proof

Festa A., Pini G.A., Ogata K. and Dilek Y., 2019. Diagnostic features and field-criteria in recognition of tectonic, sedimentary and diapiric mélanges in orogenic belts and exhumed subduction-accretion complexes. Gondwana Res., 74: 7-30. https://doi.org/10.1016/j.gr.2019.01.003

Fontana E., Panseri M. and Tartarotti P., 2008. Oceanic relict textures in the Mount Avic serpentinites, Western Alps. Ofioliti, 33 (2): 105-118. https://doi.org/10.4454/ofioliti.v33i2.367

Fontana E., Tartarotti P., Panseri M. and Buscemi S., 2015. Geological map of the Mount Avic massif (Western Alps Ophiolites). J. Maps, 11 (1): 126-135. https://doi.org/10.1080/17445647.2014.959567

Fornash K.F. and Whitney D.L., 2020. Lawsonite-rich layers as records of fluid and element mobility in subducted crust (Sivrihisar Massif, Turkey). Chem. Geol., 533: 119356. https://doi.org/10.1016/j.chemgeo.2019.119356

Frey M., Desmons J. and Neubauer F., 1999. The new metamorphic map of the Alps. Schweiz. Mineral. Petrogr. Mitt., 79, 230 pp.

Frezzotti M.L., Selverstone J., Sharp Z.D. and Compagnoni R., 2011. Carbonate dissolution during subduction revealed by diamond-bearing rocks from the Alps. Nat. Geosci., 4: 703-706. https://doi.org/10.1038/ngeo1246

Gerya T.V., Stöckhert B. and Perchuk A.L., 2002. Exhumation of high-pressure metamorphic rocks in a subduction channel: A numerical simulation. Tectonics, 21 (6): 6-1. https://doi.org/10.1029/2002TC001406

Gibson I.L., Milliken K.L. and Morgan J.K., 1996. Serpentinite-breccia landslide deposits generated during crustal extension at the Iberia Margin. In: Withmarsh, R.B., Sawyer, D.S., Klaus, A., and Masson, D.G. (Eds.), Proceedings of the Ocean Drilling Program, Scientific Results, Vol. 149, 571-575.

Golyshev S.I., 1981. Fractionation of stable oxygen and carbon isotopes in carbonate systems. Geokhimiya, 10: 1427-1441.

Gorman P.J., Kerrick D.M. and Connolly J.A.D., 2006. Modeling open system metamorphic decarbonation of subducting slabs. Geochem. Geophys. Geosyst., 7 (4). https://doi.org/10.1029/2005GC001125

Groppo C., Beltrando M. and Compagnoni R., 2009. The P-T path of the ultra-high pressure Lago di Cignana and adjoining high-pressure meta-ophiolitic units: insights into the evolution of the subducting Tethyan slab. J. metamorph. Geol., 27: 207-231. https://doi.org/10.1111/j.1525-1314.2009.00814.x

Grozeva N.G., Klein F., Seewald J.S. and Sylva S.P., 2017. Experimental study of carbonate formation in oceanic peridotite. Geochim. Cosmochim. Acta, 199: 264-286. https://doi.org/10.1016/j.gca.2016.10.052

Hirauchi K.I., Yamamoto Y., den Hartog S.A.M. and Niemeijer A.R., 2020. The role of metasomatic alteration on frictional properties of subduction thrusts: An example from a serpentinite body in the Franciscan Complex, California. Earth Planet. Sci. Lett., 531: 115967. https://doi.org/10.1016/j.epsl.2019.115967

Hoefs J., 2009. Stable isotope geochemistry. 6th Ed., Springer International Publishing, Switzerland. https://doi.org/10.1007/978-3-540-70708-0

Jaeckel K., Bebout G.E. and Angiboust S., 2018. Deformation-enhanced fluid and mass transfer along Western and Central Alps paleo-subduction interfaces: Significance for carbon cycling models. Geosphere, 14 (6): 2355-2375. https://doi.org/10.1130/GES01587.1

Kelemen P.B. and Hirth G., 2012. Reaction-driven cracking during retrograde metamorphism: Olivine hydration and carbonation. Earth Planet. Sci. Lett., (345-348): 81–89. https://doi.org/10.1016/j.epsl.2012.06.018

Pre-Proof

Kelemen P.B. and Manning C.E., 2015. Reevaluating carbon fluxes in subduction zones, what goes down, mostly comes up. Proc. Natl. Acad. Sci. USA, 112 (30): E3997-E4006. https://doi.org/10.1073/pnas.1507889112

Kelemen P.B. and Matter J., 2008. In situ carbonation of peridotite for CO_2 storage. Proc. Natl. Acad. Sci. USA, 105 (17): 295-217. https://doi.org/10.1073/pnas.0805794105

Kelemen P.B., Matter J., Streit E.E., Rudge J.F., Curry W.B. and Bluztajn J., 2011. Rates and mechanisms of mineral carbonation in peridotite: natural processes and recipes for enhanced, in situ CO_2 capture and storage. Annu. Rev. Earth Planet. Sci., 39: 545-576. https://doi.org/10.1146/annurev-earth-092010-152509

Kerrick D.M. and Connolly J.A.D., 1998. Subduction of ophicarbonates and recycling of CO_2 and H_2O. Geology, 26: 375-378. https://doi.org/10.1130/0091-7613(1998)026<0375:SOOARO>2.3.CO;2

Kim S.T., Coplen T.B. and Horita J., 2015. Normalization of stable isotope data for carbonate minerals: Implementation of IUPAC guidelines. Geochim. Cosmochim. Acta, 158: 276-289. https://doi.org/10.1016/j.gca.2015.02.011

Lafay R., Deschamps F., Schwartz S., Guillot S., Godard M., Debret B. and Nicollet C., 2013. High-pressure serpentinites, a trap-and-release system controlled by metamorphic conditions: Example from the Piedmont zone of the western Alps. Chem. Geol., 343: 38-54. https://doi.org/10.1016/j.chemgeo.2013.02.008

Lagabrielle Y., 2009. Mantle exhumation and lithospheric spreading: An historical perspective from investigations in the Oceans and in the Alps-Apennines ophiolites. Boll. Soc. Geol. It., 128 (2): 279-293. https://doi.org/10.3301/IJG.2009.128.2.279

Lagabrielle Y. and Cannat M., 1990. Alpine Jurassic ophiolites resemble the modern central Atlantic basement. Geology, 18: 319-322. https://doi.org/10.1130/0091-7613(1990)018<0319:AJORTM>2.3.CO;2

Leake B.E., Woolley A.R., Arps C.E.S., Birch W.D., Gilbert M.C., Grice J.D., Hawthorne F.C., Kisch H.J., Krivovichev V.G., Linthout K., Laird J., Mandarino J.A., Maresch W.V., Schumacher J.C., Smith D.C., Stephenson N.C.N., Whittaker E.J.W. and Youzhi G., 1997. Nomenclature of amphiboles: Report of the subcommittee on amphiboles of the International Mineralogical Association, commission on new minerals and mineral names. Can. Mineral., 35: 219-246. https://doi.org/10.1180/minmag.1997.061.405.13

Leake B.E., Woolley A.R., Birch W.D., Burke E.A.J., Ferraris G., Grice J.D., Hawthorne F.C., Kisch H.J., Krivovichev V.G., Schumacher J.C., Stephenson N.C.N. and Whittaker E.J.W., 2004. Nomenclature of amphiboles: Additions and revisions to the International Mineralogical Association's amphibole nomenclature. Am. Mineral., 89: 883-887. https://doi.org/10.1180/0026461046810182

Luoni P., Rebay G., Spalla M.I. and Zanoni D., 2018. UHP Ti-chondrodite in the Zermatt-Saas serpentinite: Constraints on a new tectonic scenario. Am. Mineral., 103: 1002-1005. https://doi.org/10.2138/am-2018-6460

Machel H.G., 2004. Concepts and models of dolomitization: a critical reappraisal. In: Braithwaite C.J.R., Rizzi G. and Darke G. (Eds.), The Geometry and Petrogenesis of Dolomite Hydrocarbon Reservoirs. Geol. Soc. Spec. Publ., 235: 7-63. https://doi.org/10.1144/GSL.SP.2004.235.01.02

Manatschal M. and Müntener O., 2009. A type sequence across an ancient magma-poor ocean–continent transition: the example of the western Alpine Tethys ophiolites. Tectonophysics, 473: 4-19. https://doi.org/10.1016/j.tecto.2008.07.021

Menzel M.D., Garrido C.J., Sánchez-Vizcaíno V.L., Marchesi C., Hidas K., Escayola M.P. and Huertas A.D., 2018. Carbonation of mantle peridotite by CO_2-rich fluids: the formation of listvenites in the Advocate ophiolite complex (Newfoundland, Canada). Lithos, 323: 238-261. https://doi.org/10.1016/j.lithos.2018.06.001

Pre-Proof

Menzel M.D., Garrido C.J. and Sánchez-Vizcaíno V.L., 2020. Fluid-mediated carbon release from serpentinite-hosted carbonates during dehydration of antigorite-serpentinite in subduction zones. Earth Planet. Sci. Lett., 531: 115964. https://doi.org/10.1016/j.epsl.2019.115964

Nervo R. and Polino R., 1976. Un lembo di cristallino Dent-Blanche alla Torre Ponton (Valle d'Aosta). Boll. Soc. Geol. It., 95: 647-657.

Padrón-Navarta J.A., Sánchez-Vizcaíno V.L., Hermann J., Connolly J.A., Garrido C.J., Gómez-Pugnaire M.T. and Marchesi C., 2013. Tschermak's substitution in antigorite and consequences for phase relations and water liberation in high-grade serpentinites. Lithos, 178: 186-196. https://doi.org/10.1016/j.lithos.2013.02.001

Passchier C.W. and Trouw R.A.J., 2005. Microtectonics, 2nd. Revis ed. Springer-Verlag Berlin Heidelberg. https://doi.org/10.1007/3-540-29359-0

Peacock S.A., 1990. Fluid Processes in Subduction Zones. Science, 248 (4953): 329-337. https://doi.org/10.1126/science.248.4953.329

Petriglieri J.R., Salvioli-Mariani E., Mantovani L., Tribaudino M., Lottici P.P., Laporte-Magoni C. and Bersani D., 2015. Micro-Raman mapping of the polymorphs of serpentine. J. Raman Spectrosc., 46 (10): 953-958. https://doi.org/10.1002/jrs.4695

Piccoli F., Brovarone A.V. and Ague J.J., 2018. Field and petrological study of metasomatism and high-pressure carbonation from lawsonite eclogite-facies terrains, Alpine Corsica. Lithos, 304: 16-37. https://doi.org/10.1016/j.lithos.2018.01.026

Piccoli F., Brovarone A.V., Beyssac O., Martinez I., Ague J.J. and Chaduteau C., 2016. Carbonation by fluid-rock interactions at high-pressure conditions: Implications for carbon cycling in subduction zones. Earth Planet. Sci. Lett., 445: 146-159. https://doi.org/10.1016/j.epsl.2016.03.045

Pichler H. and Schmitt-Riegraf C., 1997. Rock-forming minerals in thin sections. Chapman & Hall Ed., London, 2-6 Boundary Row, London SE1 8HN, UK, 220 pp.

Prigent C., Guillot S., Agard P., Lemarchand D., Soret M. and Ulrich M., 2018. Transfer of subduction fluids into the deforming mantle wedge during nascent subduction: Evidence from trace elements and boron isotopes (Semail ophiolite, Oman). Earth Planet. Sci. Lett., 484: 213-228. https://doi.org/10.1016/j.epsl.2017.12.008

Reinecke T., 1998. Prograde high-to ultrahigh-pressure metamorphism and exhumation of oceanic sediments at Lago di Cignana, Zermatt-Saas zone, western Alps. Lithos, 42: 147-189. https://doi.org/10.1016/S0024-4937(97)00041-8

Sansone M.T.C., Prosser G., Rizzo G. and Tartarotti P., 2012. Spinel-peridotites of the Frido Unit Ophiolites (Southern Apennine-Italy): Evidence for oceanic evolution. Per. Mineral., 81: 35-59. https://doi.org/10.2451/2012PM0003

Scambelluri M., Bebout G.E., Belmonte D., Gilio M., Campomenosi N., Collins N. and Crispini L., 2016. Carbonation of subduction-zone serpentinite (high-pressure ophicarbonate; Ligurian Western Alps) and implications for the deep carbon cycling. Earth Planet. Sci. Lett., 441: 155-166. https://doi.org/10.1016/j.epsl.2016.02.034

Schmidt M.W. and Poli S., 1998. Experimentally based water budgets for dehydrating slabs and consequences for arc magma generation. Earth Planet. Sci. Lett., 163 (1-4): 361-379. https://doi.org/10.1016/S0012-821X(98)00142-3

Pre-Proof

Seyler M., Lorand J.-P., Dick H.J.B. and Drouin M., 2007. Pervasive melt percolation reactions in ultra-depleted refractory harzburgites at the Mid-Atlantic Ridge, 15° 20' N: ODP Hole 1274A. Contrib. Mineral. Petrol., 153: 303-319. https://doi.org/10.1007/s00410-006-0148-6

Shreve R.L. and Cloos M., 1986. Dynamics of sediment subduction, melange formation and prism accretion. J. Geophys. Res., 91 (10): 10229-10245. https://doi.org/10.1029/JB091iB10p10229

Spandler C., Hermann J., Faure K., Mavrogenes J.A. and Arculus R.J., 2008. The importance of talc and chlorite "hybrid" rocks for volatile recycling through subduction zones; evidence from the high-pressure subduction mélange of New Caledonia. Contrib. Mineral. Petrol., 155: 181-198. https://doi.org/10.1007/s00410-007-0236-2

Tartarotti P., Festa A., Benciolini L. and Balestro G., 2017. Record of Jurassic mass transport processes through the orogenic cycle: Understanding chaotic rock units in the high-pressure Zermatt-Saas ophiolite (Western Alps). Lithosphere, 9: 399-407. https://doi.org/10.1130/L605.1

Tartarotti P., Guerini S., Rotondo F., Festa A., Balestro G., Bebout G.E., Cannaò E., Epstein G.S. and Scambelluri M., 2019. Superposed Sedimentary and Tectonic Block-In-Matrix Fabrics in a Subducted Serpentinite Mélange (High-Pressure Zermatt Saas Ophiolite, Western Alps). Geosciences, 9 (8): 358. https://doi.org/10.3390/geosciences9080358

Tartarotti P., Susini S., Nimis P. and Ottolini L., 2002. Melt migration in the upper mantle along the Romanche Fracture Zone (Equatorial Atlantic). Lithos, 63: 125-149. https://doi.org/10.1016/S0024-4937(02)00116-0

Veizer J., Ala D., Azmy K., Bruckschen P., Buhl D., Bruhn F., Carden G.A.F., Diener A., Ebneth S., Godderis Y., Jasper T., Korte C., Pawellek F., Podlaha O.G. and Strauss H., 1999. $^{87}Sr/^{86}Sr$, $\delta^{13}C$ and $\delta^{18}O$ evolution of Phanerozoic seawater. Chem. Geol., 161 (1–3): 59-88. https://doi.org/10.1016/S0009-2541(99)00081-9

Vernon R.H., 2004. A practical guide to Rock Microstructure. Cambridge University Press, 594 pp. https://doi.org/10.1017/CBO9780511807206

Whitney D.L. and Evans B.W., 2010. Abbreviations for names of rock-forming minerals. Am. Mineral., 95: 185–187. https://doi.org/10.2138/am.2010.3371

Wicks F.J., 2000. Status of the reference X-ray powder-diffraction patterns for the serpentine minerals in the PDF database-1997. Powder Diffr., 15: 42-50. https://doi.org/10.1017/S0885715600010824

Zheng Y.F., 1999. Oxygen isotope fractionation in carbonate and sulfate minerals. Geochem. J., 33 (2): 109-126. https://doi.org/10.2343/geochemj.33.109

Zheng Y.F., Zhao Z.F. and Chen Y.X., 2013. Continental subduction channel processes: Plate interface interaction during continental collision. Chinese Sci. Bull., 58 (35): 4371-4377. https://doi.org/10.1007/s11434-013-6066-x

Pre-Proof

FIGURE CAPTIONS

Figure 1: Geographic and geological context of the study area. (a) Geographic location of the study area in the NW Alps (Italy). (b) Tectonic map of the NW Alps (modified after Balestro et al., 2015 and Tartarotti et al., 2017), with location of the high Champorcher Valley (black rectangle). ARL – Aosta-Ranzola Line; BZ – Briançonnais Zone; CL – Canavese Line; CZ – Combin Zone; DB – Dent Blanche; GP – Gran Paradiso; HZ – Helvetic Zone; IL – Insubric Line; MR – Monte Rosa; PF – Penninic Front; SA – Southern Alps; SF – Simplon Fault; SLZ – Sesia-Lanzo Zone; VO – Valaisan Ocean; ZSZ – Zermatt-Saas Zone. Orange areas: eclogitic Lower Austroalpine outliers (see text). (c) Geographic location of the Champorcher valley and of the Mont Avic Natural Park (light green area). Red rectangle represents the location of the LMO reported in Figure 2. Printing realized through GeoNavigatori (aerial photo 2012, SCT project, Regione Autonoma Valle d'Aosta). X and Y scale: 1:108.870.

Figure 2: Geological map of the study area (topographic base CTR Regione Autonoma Valle d'Aosta at scale of 1:10.000, from original field mapping at 1:5.000). Light coloured areas are interpreted geology.

Figure 3: (a) Stratigraphic reconstruction of the complete LMO sequence, north-west to the Refuge Miserin, and (b) stratigraphic section lacking the CCU, west to Lake Miserin (not to scale; see Fig. 2). (c) Outcrop view of the MH and underlying serpentinite, NW to the Refuge Miserin (hammer length is ca. 35 cm; same outcrop of Fig. 11b in Beltrando et al., 2014). (d) Sketch of Fig. 3c, highlighting the lithological contacts between units, their internal textures, and the main foliation.

Figure 4: Outcrop views of MH sub-types exposed in the Lake Miserin area. (a) MH1 interposed between metaophicarbonate and MH2 (red dashed lines delimit the unit). (b) Outcrop view of MH2 characterized by isoclinal D_2 folds with S- and Z-shaped asymmetries along limbs, and M-shaped geometry in the hinge zone (hammer length is 33 cm). Blue, red and yellow dashed lines underline traces of S_1, S_2 and D_2 axial plane, respectively. (c) Close-up of MH2 clast, with S_i (yellow dashed lines) parallel to S_e (i.e. S_2, red dashed lines). (d) Outcrop view of a massive block embedded within MH2. Red dashed lines: trace of S_2 foliation. (e) Detail of MH3 with a well-distinguished coarse-grained carbonate aggregate (Dol) embedded within Amp-rich matrix (hammer length is 30 cm). (f) Outcrop view of MH3 characterized by sigmoidal Dol-rich clasts within a foliated Amp-rich matrix. Red dashed lines: trace of S_2 foliation; arrows show the sense of shear (top-to-NW; chisel length is 17 cm).

Figure 5: Thin section photomicrographs in cross-polarized light (a, b, c, e) and BSE images (d, f) showing massive, foliated serpentinite, and MH1 type. (a) Relict mantle textures in massive serpentinite. One Cpx porphyroblast (on the right) shows irregular grain boundaries, with embayments and protrusions. Cpx porphyroblast on the left includes Srp pseudomorphs on unknown mineral (see text). Lower right: Srp aggregate with a canvas fabric (former mesh texture?); thin section C1. (b) Relict Spl crystals (Fe-Chr core and Mag rim) with an anhedral holly-leaf shape, rimmed by fine-grained Srp+Chl aggregate reminiscent of original Pl corona; thin section C1. (c) Massive serpentinite with Mgs+Dol1 aggregate marking the main foliation S_2 (red dashed line). Mgs composition is confirmed by microprobe analysis (see text). Dol occurs as coarse-grained Dol1 and Dol2 neoblasts; thin section B1. (d) Foliated serpentinite with zoned Spl, with Al-Chr core (dark grey), a first rim of Fe-Chr (light grey) and a second external rim of Mag (white). The two rims have many Srp inclusions along their external boundaries; Spl is surrounded by fine-grained Srp (Atg) aggregates (see Table S3, thin section B1); thin section B1. (e) MH1: inequigranular interlobate Amp aggregate surrounding a Dol-rich domain. Amp sometimes has relict Cpx inclusions (confirmed by microprobe analysis; see Table S6) and is partially replaced by Cal3. Chl is associated to Fe-Chr+Mag crystals, while Dol1 porphyroblast has irregular grain boundaries and is highly fractured (upper left corner); thin section B5. (f) Detail of MH1 Amp-rich domain: Amp crystals are

fractured with fractures filled by Cal3; Chl crystallized at the Amp grain boundaries (see Table S7, thin section B5). Dol is replaced by Cal3 (see text).

Figure 6: Thin section photomicrographs in cross-polarized light (a, b, c, d, f) and plain-polarized light (e) showing MH2 and MH3 types. (a) Coarse-grained boudinaged Amp porphyroclast, with SPO along the S_2 foliation in MH2; boudin neck is filled with Dol2 and Cal3. Polygonal, fine-grained Dol2 aggregates constitute the carbonate-rich microlithons, and, together with Amp, mark the S_2 with their SPO. Red dashed line: track of S_2 (thin section B10B). (b) Inferred S_1 foliation defined by mineral layering consisting of alternating layers of Op(Mag)+Chl, Amp, and Dol, respectively (see Fig. 4b for outcrop view). SPO of Dol2±Dol1 and re-oriented Amp crystals define the axial planar S_2 foliation. Yellow dashed line: track of S_1; red dashed line: track of S_2; red dotted line: track of PA_2 (thin section B11). (c) Close-up of a massive metasomatised block embedded within MH2: the massive texture is produced by fine-grained polygonal Dol2 aggregates (recrystallized from a coarser deformed Dol1) and in equilibrium with Amp grains. Cal3 grows within Dol2 triple points, at the expense of Amp. Interference of two foliation is visible: one folded (S_2) foliation is intersected by a second incipient foliation (S_3?) defined by Amp2 SPO oriented at high angle to S_2 (thin section B12). (d) Detail of disrupted levels within MH2: levels consist of Chl+Op-rich films alternating to Dol+Cpx-rich microlithons defining the S_2 foliation. Sigmoid-shaped recrystallized Cpx crystals are oblique to the S_2 direction and interpreted as marking a relict S_1. Cal3 fills a tension gash. Yellow dashed line: track of S_1; red dashed line: track of S_2 (thin section B13B). (e) Dol1 sigmoidal domain in MH3, recrystallized into Dol2 near the pressure shadow and surrounded by Amp+Chl+Op(Mag)-rich matrix. SPO of Amp grains defines the S_2 foliation. Within the pressure shadow (on the right) a previous S_1 foliation is preserved and defined by SPO of fine-grained Amp grains; alternatively it is a volume of vertical flux of S_2. S-C and S-C' structures are observable near the pressure shadow and the sigmoid border, defined either by Amp grains or by Chl+Op aggregates. Yellow dashed line: track of S_1; red dashed lines: tracks of S_2; white area: sketch schematizing the S-C' structures observed in Amp aggregates; thin section H5. (f) Detail of the contact between Amp+Cpx layers embedding eye-shaped porphyroclasts of Cpx within MH3. Cal3 ribbon develops along the contact between the Amp+Cpx domains and Dol2 domains; thin section G4.

Figure 7: (a-b) Serpentine compositional plots: (a) SiO_2 vs MgO; (b) Si vs Al with the MSH ($MgO–SiO_2–H_2O$) and MASH ($MgO–Al_2O_3–SiO_2–H_2O$) antigorite endmembers indicated with the red square symbol joined by a Tschermak's exchange substitution (continuous line). Dotted horizontal band is the maximum solubility of Al in Atg at 3–20 kbar obtained by Padrón-Navarta et al. (2013) calculations. Legend of symbols categorizes Srp in foliated and massive serpentinites. (c) Dolomite and calcite compositional plot: Ca vs Mg. Legend of symbols categorizes Dol and Cal in serpentinites and MH types. (d) Chlorite compositional plot: Si vs $\#Fe_{tot}$. Legend of symbols categorizes Chl in MH types and massive serpentinite.

Figure 8: BSE photomicrographs of MH2 and MH3 types. (a) Dol-rich level within transposed clast of MH2, characterized by relict Dol1 (zoned) with Cpx (Di) inclusion and associated to inclusion-free Amp1 (zoned); thin section B8. (b) Amp1 aggregate with SPO parallel to S_2, alternating to Dol1 (replaced by Cal), elongated Mag microgranules and Chl levels. Post-D_2 Amp2 porphyroblasts are elongated at high angle to S_2, have Mag inclusion trails (parallel to S_2) and Di inclusion (Cpx). Amp2 is post-kinematic with respect to Mag trails; thin section B8. (c) Amphibole-rich levels consist of coarse-grained (Amp1?) porphyroblasts, boudinaged and with SPO aligned to S_2 in MH2. Cal replaces both Amp and Dol2 aggregates; thin section B11. (d) Zoned amphibole with Dol/Cal inclusions within the pressure shadow of the Dol1 sigmoid (see Fig. 6e. Dol1 porphyroblast is replaced by Amp and Cal (+Tlc) that are the products of Dol destabilization; thin section H5).

Figure 9: (a) Representative micro-Raman spectra of antigorite (thin section B1, analysis s1): left, in the low-wavenumber region corresponding to the inner vibrational modes of the lattice and to $Si–O_4$ vibrations, and right, in the high-wavenumber region corresponding to vibrations of the intracrystalline OH groups (regions from

Pre-Proof

Petriglieri et al. 2015). (b) Measured Srp is fine-grained, fibrous antigorite aggregate of foliated serpentinite (thin section B1, photomicrograph in cross-polarized light).

Figure 10: Oxygen and carbon stable isotope composition of analysed carbonates (samples MIS64bis, MIS46, E9 and 6): (a) $\delta^{18}O_{VSMOW}$ vs. $\delta^{13}C_{VPDB}$ values (per mil) and (b) $\delta^{18}O_{VSMOW}$ values (per mil) vs. LMO units. For comparison, the range of $\delta^{18}O_{VSMOW}$ and $\delta^{13}C_{VPDB}$ values of carbonates from Zermatt-Saas ophicarbonates (Collins et al., 2015) and calcschists (Cartwright and Barnicoat, 1999; Cook-Kollars et al., 2014) are reported. The Zermatt-Saas serpentinites whole rock $\delta^{18}O_{VSMOW}$ values are taken from Cartwright and Barnicoat (1999).

Figure 11: Qualitative P-T stability fields (coloured areas) for the studied LMO rocks during Alpine D_x phases (phase equilibria for model ophicarbonate bulk composition made up of Cal+Atg+Tlc are from Kerrick and Connolly, 1998). Initial volume percents of solid phases in the model rock composition is: 86.94% Atg + 2.26% Tlc + 10.80% Cal. F: fluid (H_2O-CO_2). Pair of numbers denotes rock volatile content (wt.% CO_2 is listed above wt% H_2O) calculated by Kerrick and Connolly (1998), which are not necessarily conformable to our case study. P-T path of the Zermatt-Saas Zone (ZSZ) is shown (red arrow; from Angiboust et al., 2009). Redrawn from Kerrick and Connolly (1998).

Figure 12: Schematic conceptualization of the MH formation during the LMO tectono-metamorphic evolution toward the HP metamorphic peak, from (a) the oceanic stage and subduction (pre-D_1 and D_1 phases, Jurassic to late Eocene) to (b) the late subduction and early collision (D_2 phase, late Eocene to early Oligocene). Details of (c) the D_1 phase and of (d) the D_2 phase are represented showing structures (S_1 and S_2 layering/schistosity, black and red dashed lines respectively) and fluids pathways along the metaophiolite basement and metasediments interface. See text for additional explanation. Sketches were modified and adapted from Lafay et al. (2013), Angiboust et al. (2014) and Balestro et al. (2018).

Pre-Proof

Fig. 1

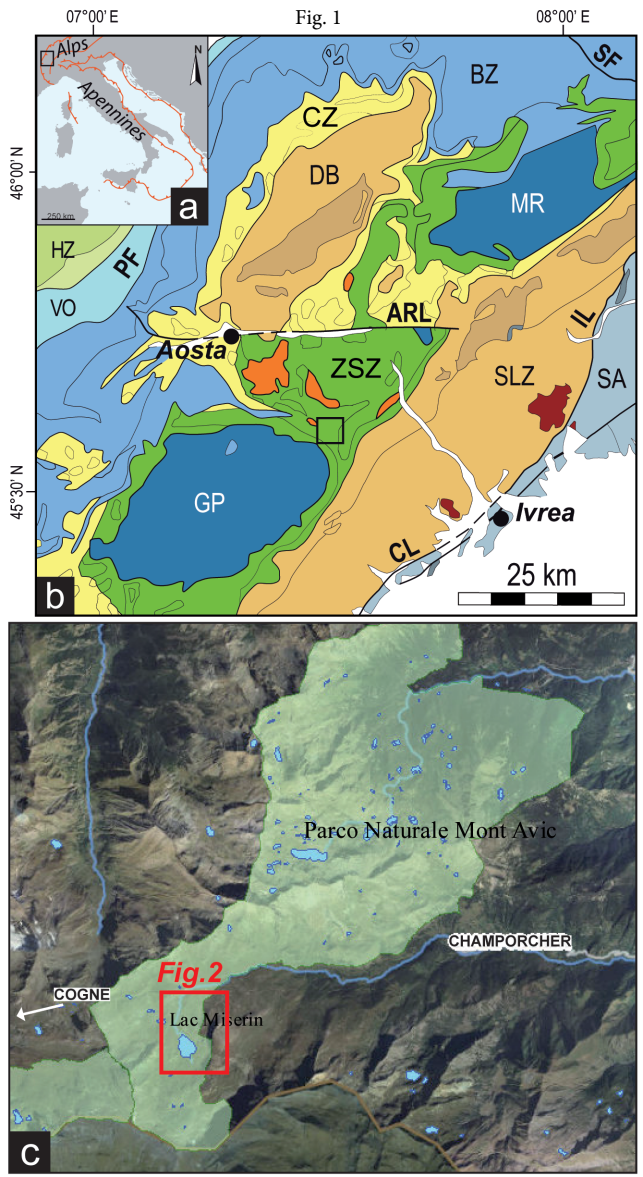
07°00' E
08°00' E
46°00' N
45°30' N
Alps
Apennines
N
250 km
a
BZ
SF
CZ
DB
MR
HZ
PF
VO
ARL
IL
Aosta
ZSZ
SLZ
SA
GP
Ivrea
CL
25 km
b
Parco Naturale Mont Avic
CHAMPORCHER
Fig.2
COGNE
Lac Miserin
c

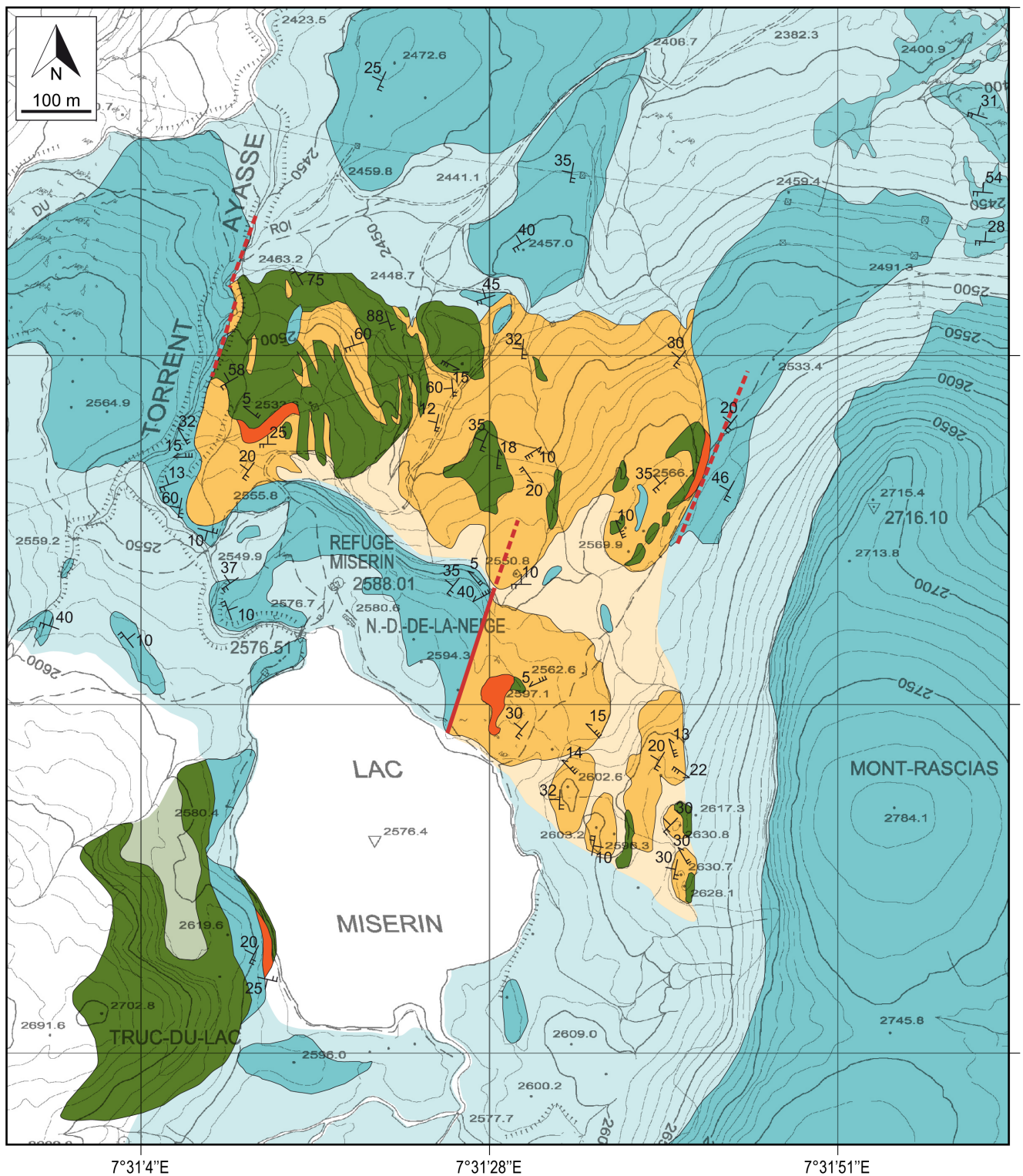

PIEDMONT ZONE
ZERMATT-SAAS ZONE
Lake Miserin Ophiolite (LMO)

- *Calcschist unit (CSU)*
- *Composite Chaotic unit (CCU)*
- *Metasomatic Horizon (MH)*
- *Serpentinite and metaophicarbonate*

Legend of symbols

- Lithologic contact
- Late-Alpine fault (unknown kinematics)
- S_2 foliation
- A_2 fold axis
- A_3 fold axis

Fig. 2

Fig. 3

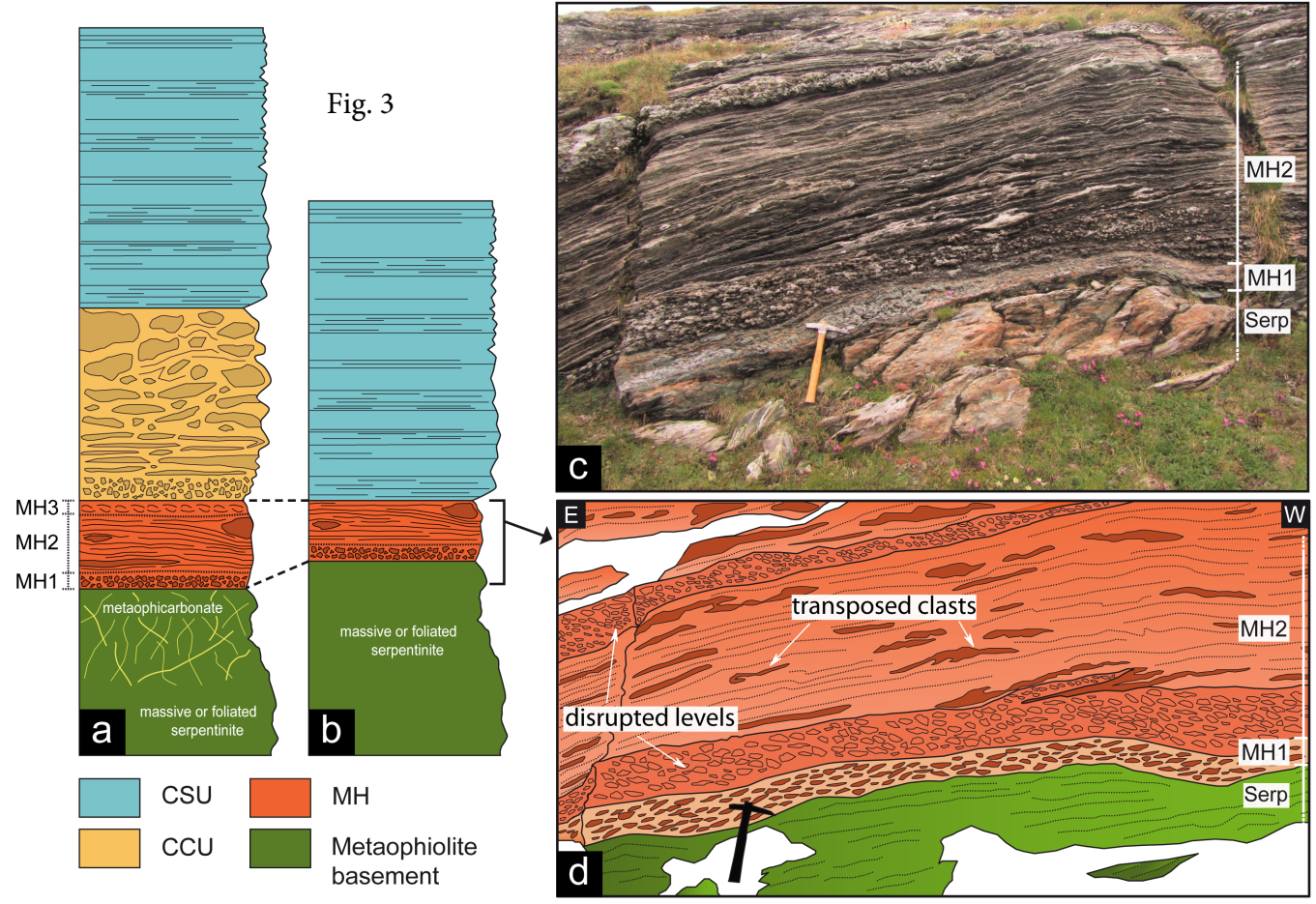
MH3
MH2
MH1
metaophicarbonate
massive or foliated serpentinite
a
massive or foliated serpentinite
b
CSU
CCU
MH
Metaophiolite basement
MH2
MH1
Serp
c
E
W
transposed clasts
disrupted levels
MH2
MH1
Serp
d

Fig. 4

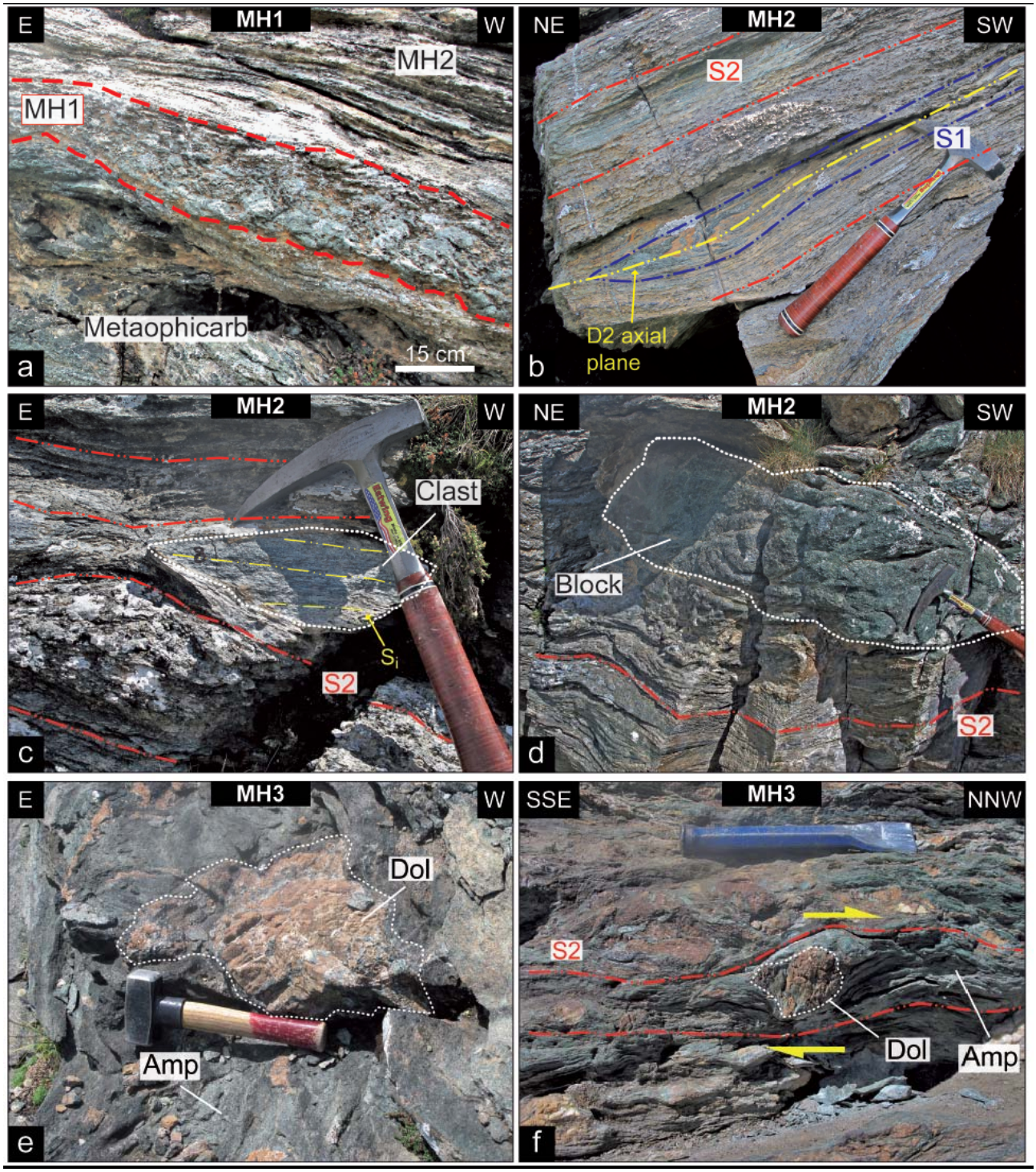
E
MH1
W
MH2
MH1
Metaophicarb
15 cm
a
NE
MH2
SW
S2
S1
D2 axial plane
b
E
MH2
W
Clast
Si
S2
c
NE
MH2
SW
Block
S2
d
E
MH3
W
Dol
Amp
e
SSE
MH3
NNW
S2
Dol
Amp
f

Fig.5

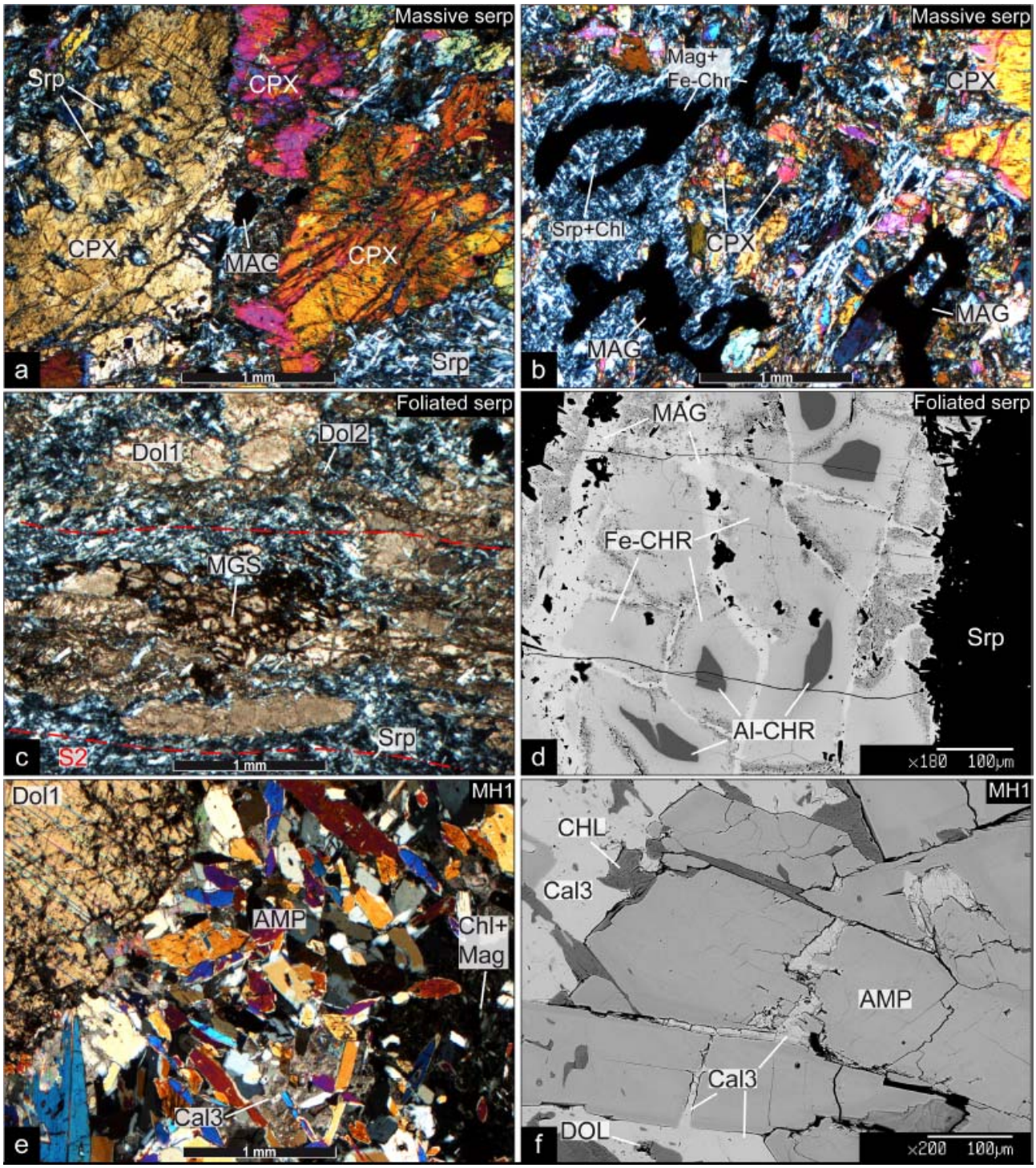
Massive serp
Srp
CPX
CPX
MAG
CPX
Srp
a
1 mm
Massive serp
Mag+
Fe-Chr
CPX
Srp+Chl
CPX
MAG
MAG
b
1 mm
Foliated serp
Dol1
Dol2
MGS
S2
Srp
c
1 mm
MAG
Foliated serp
Fe-CHR
Srp
Al-CHR
d
×180 100µm
Dol1
MH1
AMP
Chl+
Mag
Cal3
e
1 mm
MH1
CHL
Cal3
AMP
Cal3
DOL
f
×200 100µm

Fig.6

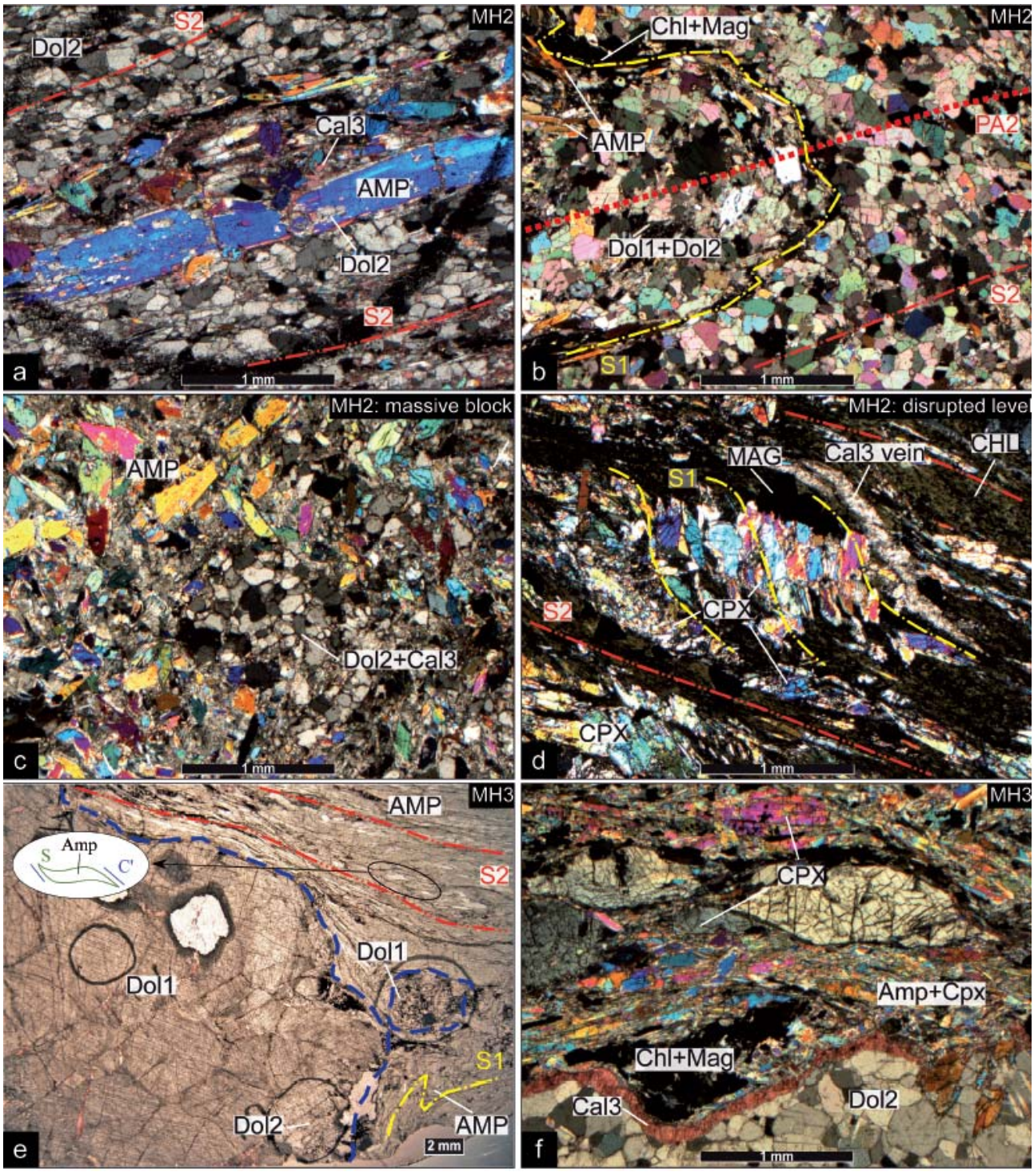
MH2
S2
Dol2
Cal3
AMP
Dol2
S2
a
1 mm
MH2
Chl+Mag
AMP
PA2
Dol1+Dol2
S2
S1
b
1 mm
MH2: massive block
AMP
Dol2+Cal3
c
1 mm
MH2: disrupted level
MAG
Cal3 vein
CHL
S1
S2
CPX
CPX
d
1 mm
MH3
AMP
Amp
S
C'
S2
Dol1
Dol1
S1
Dol2
AMP
e
2 mm
MH3
CPX
Amp+Cpx
Chl+Mag
Cal3
Dol2
f
1 mm

Fig. 7

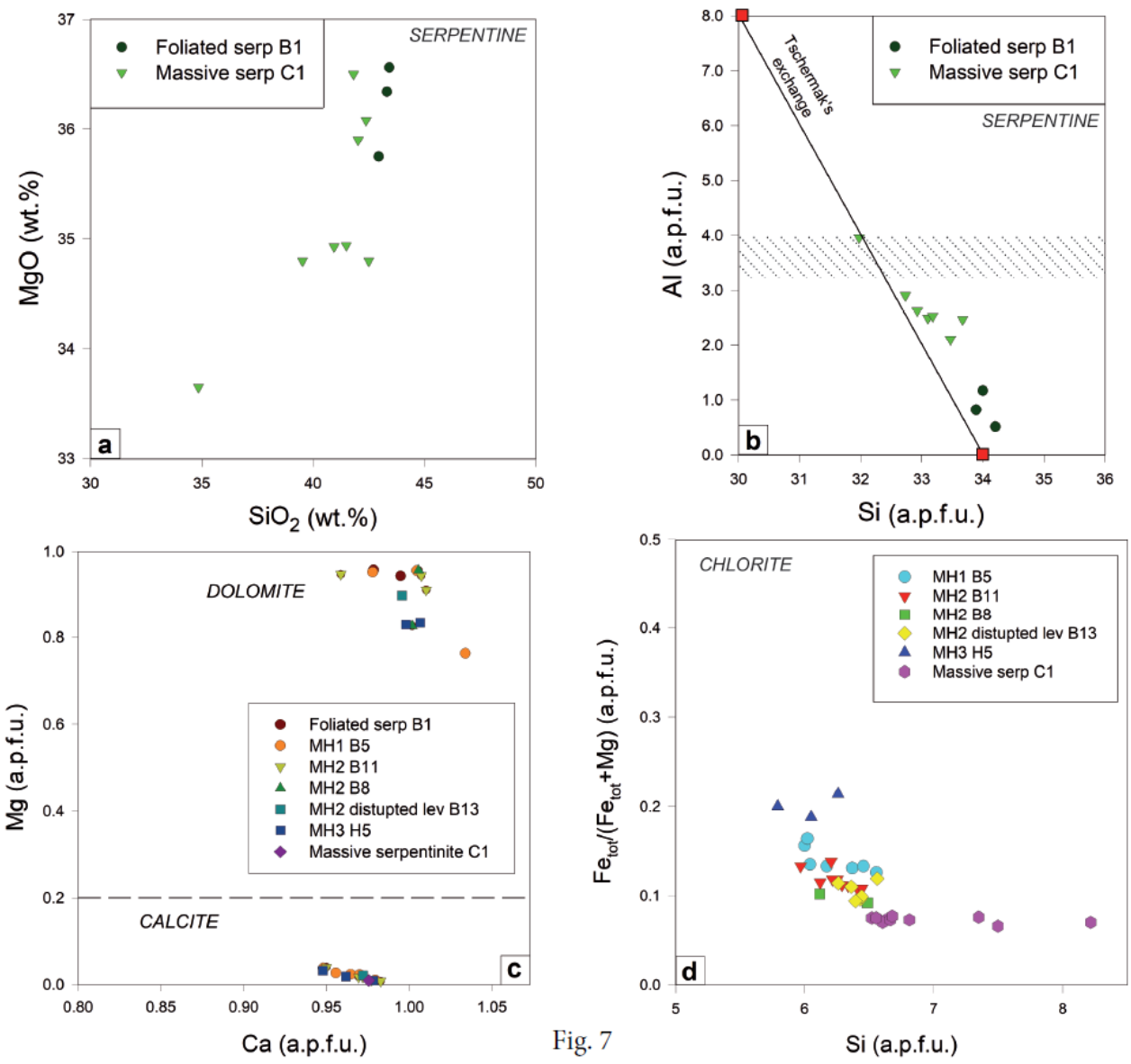
a
SERPENTINE
Foliated serp B1
Massive serp C1
MgO (wt.%)
SiO2 (wt.%)
b
SERPENTINE
Tschermak's exchange
Foliated serp B1
Massive serp C1
Al (a.p.f.u.)
Si (a.p.f.u.)
c
DOLOMITE
CALCITE
Foliated serp B1
MH1 B5
MH2 B11
MH2 B8
MH2 distupted lev B13
MH3 H5
Massive serpentinite C1
Mg (a.p.f.u.)
Ca (a.p.f.u.)
d
CHLORITE
MH1 B5
MH2 B11
MH2 B8
MH2 distupted lev B13
MH3 H5
Massive serp C1
Fetot/(Fetot+Mg) (a.p.f.u.)
Si (a.p.f.u.)

Fig. 7

Fig. 8

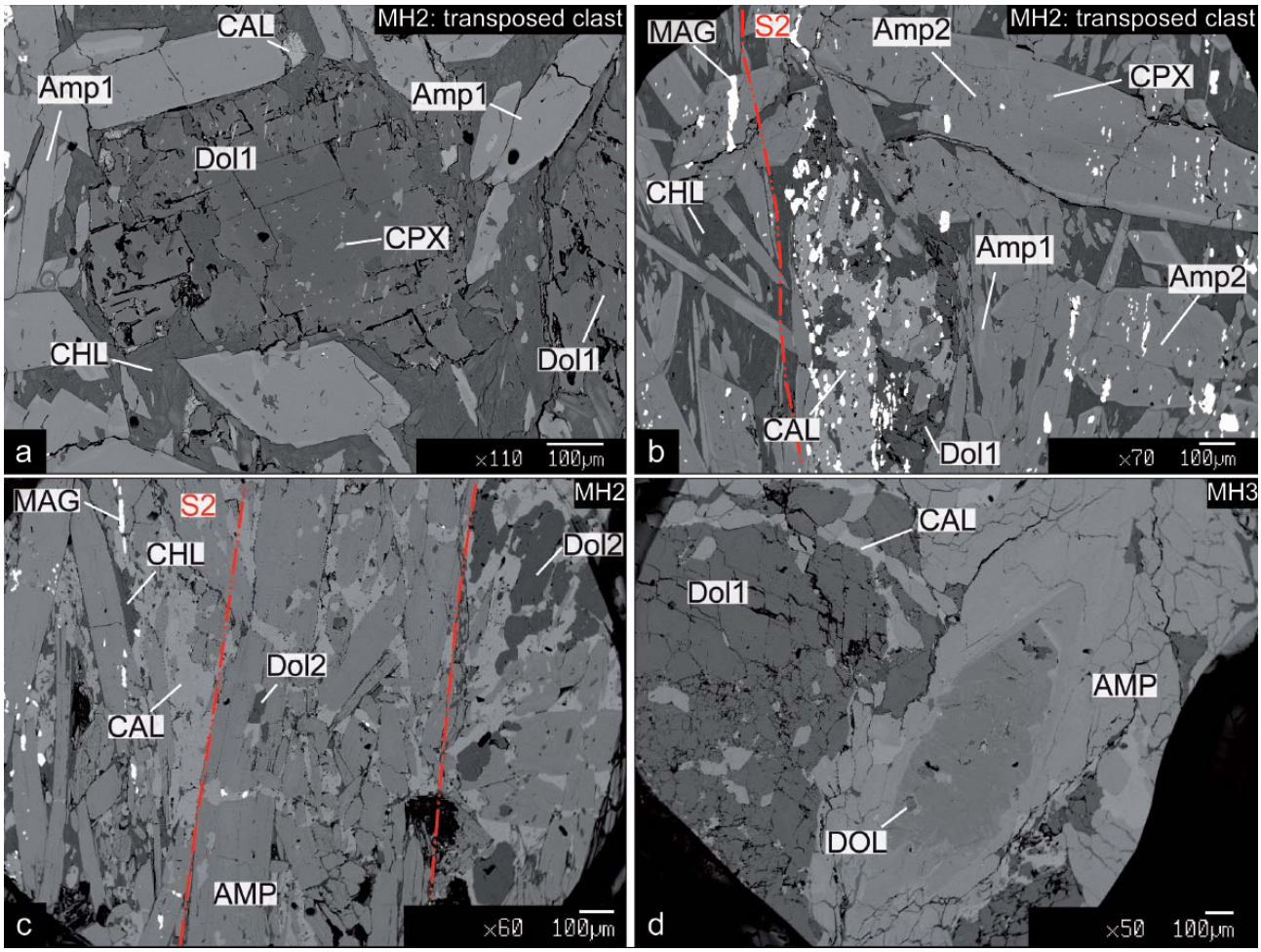
CAL
MH2: transposed clast
Amp1
Amp1
Dol1
CPX
CHL
Dol1
a
×110 100µm
MAG
S2
Amp2
MH2: transposed clast
CPX
CHL
Amp1
Amp2
CAL
Dol1
b
×70 100µm
MAG
S2
MH2
CHL
Dol2
Dol2
CAL
AMP
c
×60 100µm
CAL
MH3
Dol1
AMP
DOL
d
×50 100µm

Fig. 9

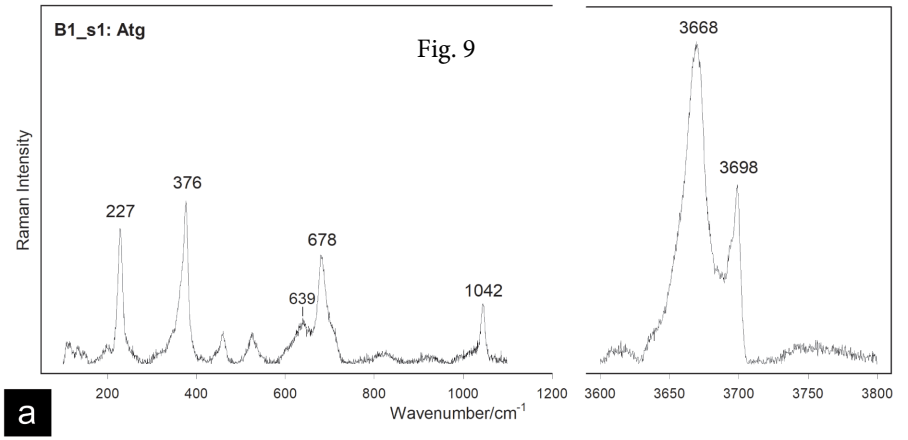
B1_s1: Atg
Raman Intensity
227
376
639
678
1042
3668
3698
200
400
600
800
1000
1200
3600
3650
3700
3750
3800
Wavenumber/cm-1
a

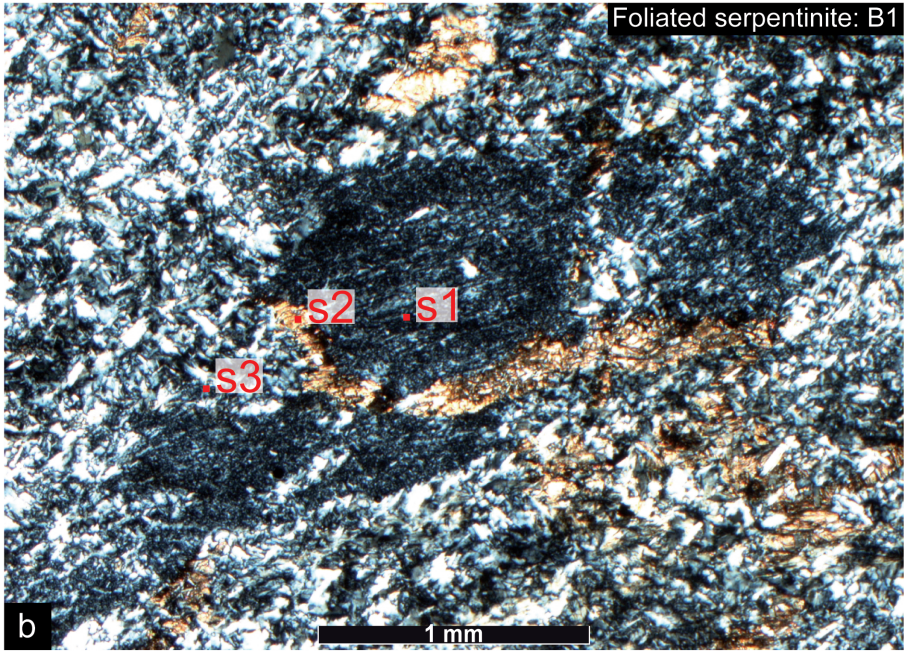
Foliated serpentinite: B1
.s2
.s1
.s3
1 mm
b

Fig. 10

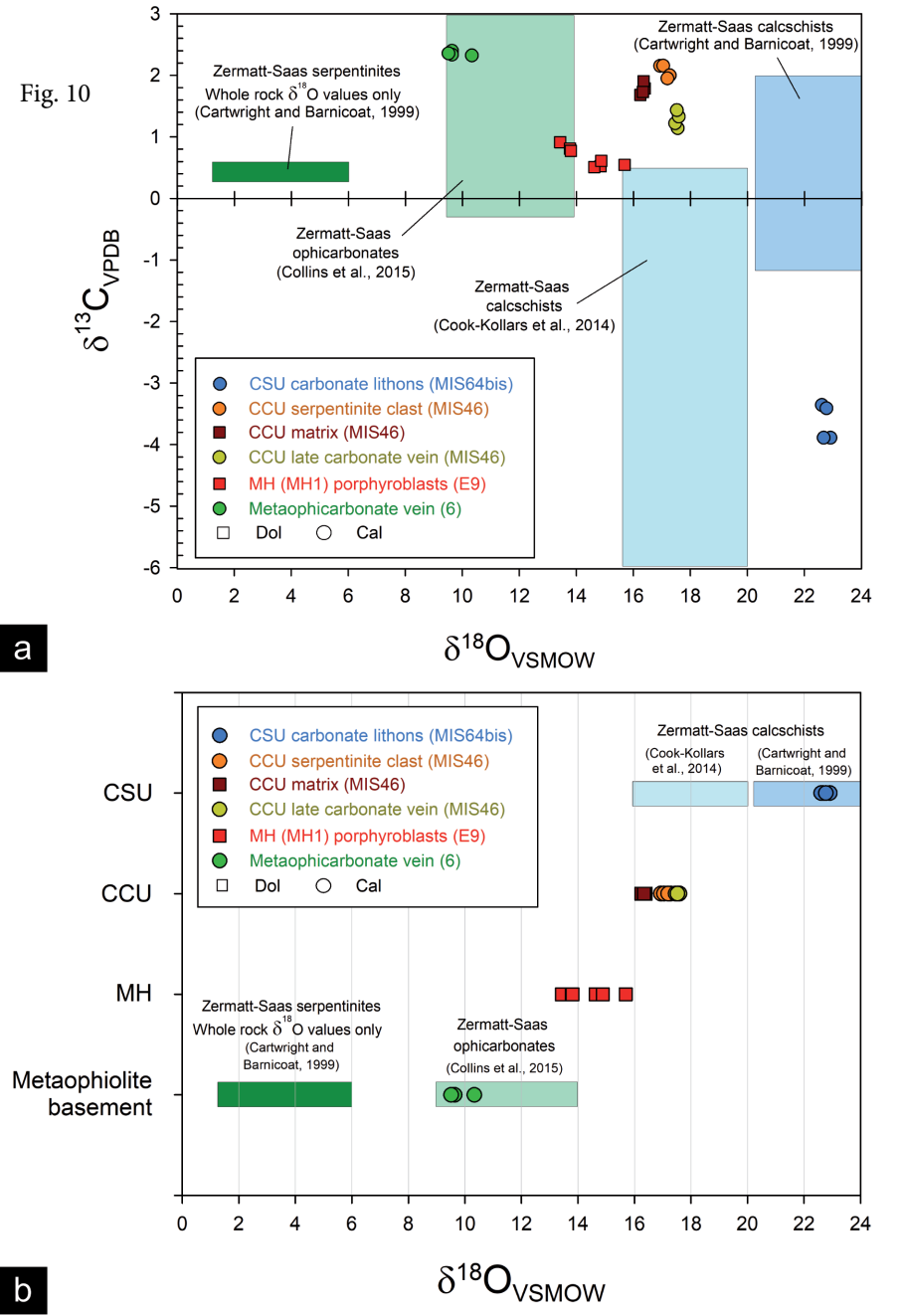
Zermatt-Saas calcschists
(Cartwright and Barnicoat, 1999)
Zermatt-Saas serpentinites
Whole rock δ18O values only
(Cartwright and Barnicoat, 1999)
Zermatt-Saas
ophicarbonates
(Collins et al., 2015)
Zermatt-Saas
calcschists
(Cook-Kollars et al., 2014)
CSU carbonate lithons (MIS64bis)
CCU serpentinite clast (MIS46)
CCU matrix (MIS46)
CCU late carbonate vein (MIS46)
MH (MH1) porphyroblasts (E9)
Metaophicarbonate vein (6)
Dol
Cal
δ13CVPDB
δ18OVSMOW
a
Zermatt-Saas calcschists
(Cook-Kollars et al., 2014)
(Cartwright and Barnicoat, 1999)
CSU
CCU
MH
Metaophiolite basement
Zermatt-Saas serpentinites
Whole rock δ18O values only
(Cartwright and Barnicoat, 1999)
Zermatt-Saas
ophicarbonates
(Collins et al., 2015)
δ18OVSMOW
b

Fig. 11

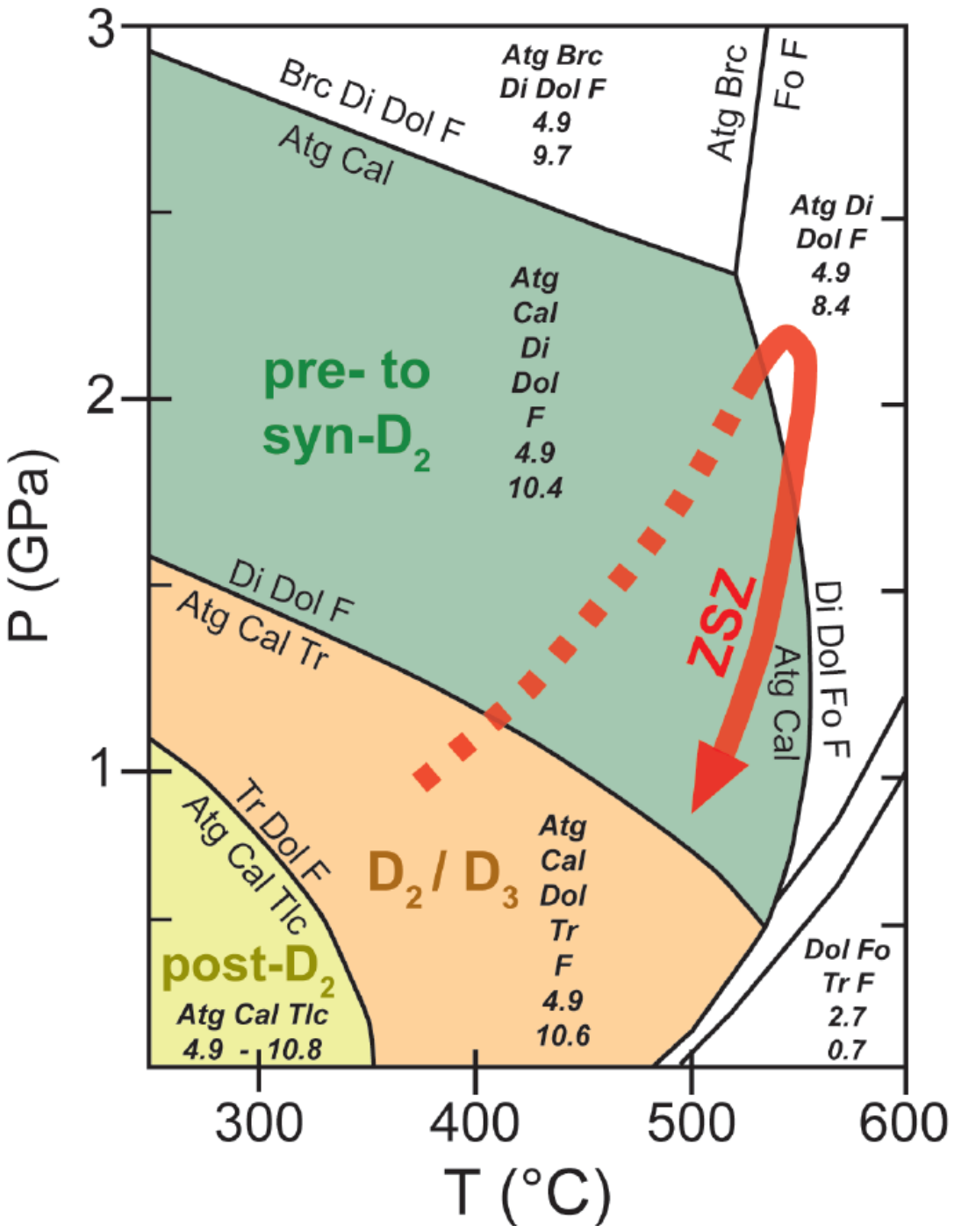
3
2
1
P (GPa)
300
400
500
600
T (°C)
Brc Di Dol F
Atg Cal
Atg Brc
Di Dol F
4.9
9.7
Atg Brc
Fo F
Atg Di
Dol F
4.9
8.4
pre- to
syn-D2
Atg
Cal
Di
Dol
F
4.9
10.4
ZSZ
Di Dol F
Atg Cal Tr
Atg Cal
Di Dol Fo F
Tr Dol F
Atg Cal Tlc
D2 / D3
Atg
Cal
Dol
Tr
F
4.9
10.6
post-D2
Atg Cal Tlc
4.9 - 10.8
Dol Fo
Tr F
2.7
0.7

Fig. 12

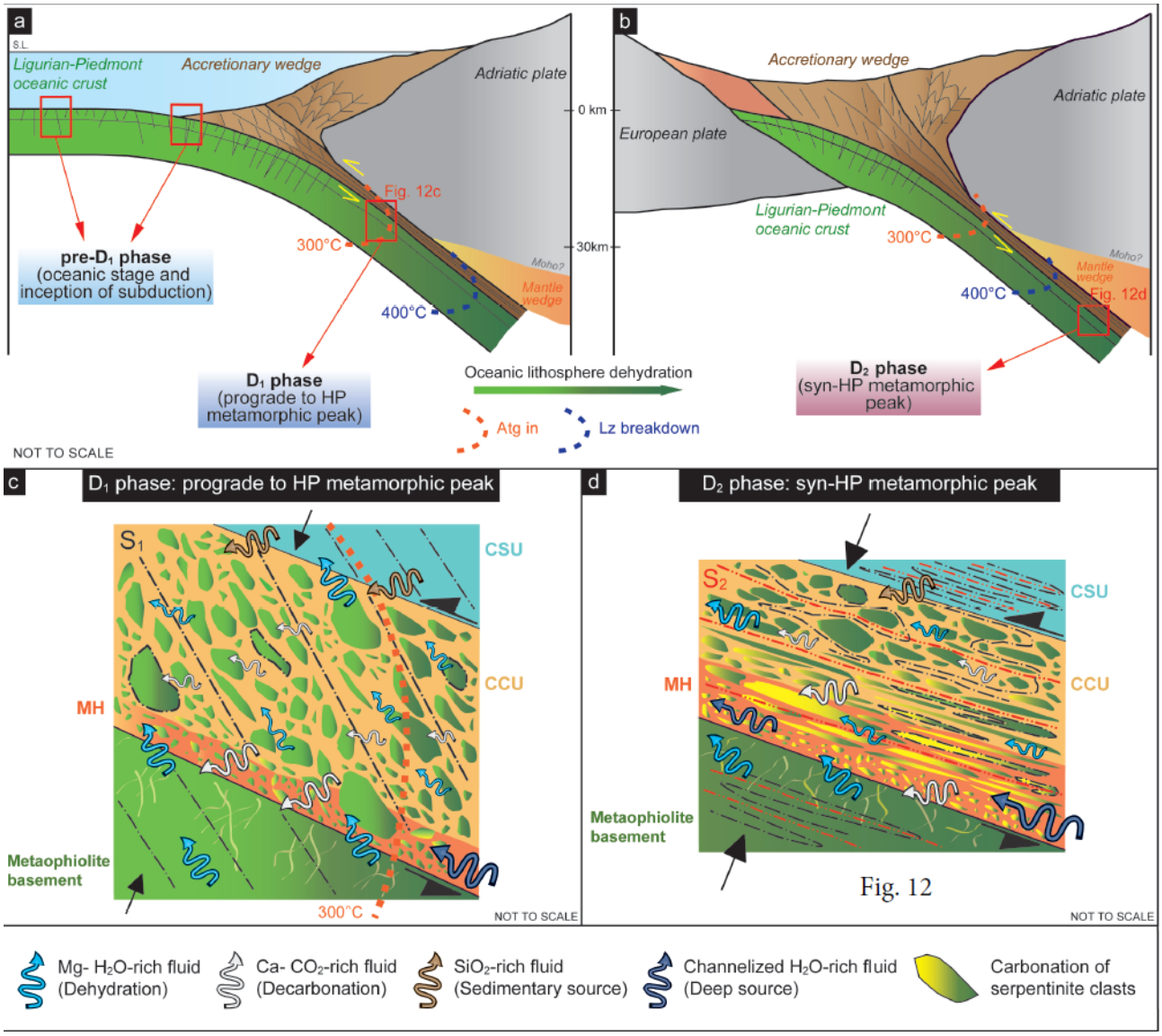
a
S.L.
Ligurian-Piedmont oceanic crust
Accretionary wedge
Adriatic plate
0 km
30km
Fig. 12c
300°C
400°C
Moho?
Mantle wedge
pre-D1 phase
(oceanic stage and inception of subduction)
D1 phase
(prograde to HP metamorphic peak)
b
Accretionary wedge
Adriatic plate
European plate
Ligurian-Piedmont oceanic crust
300°C
400°C
Moho?
Mantle wedge
Fig. 12d
D2 phase
(syn-HP metamorphic peak)
Oceanic lithosphere dehydration
Atg in
Lz breakdown
NOT TO SCALE
c
D1 phase: prograde to HP metamorphic peak
S1
CSU
CCU
MH
Metaophiolite basement
300°C
NOT TO SCALE
d
D2 phase: syn-HP metamorphic peak
S2
CSU
CCU
MH
Metaophiolite basement
NOT TO SCALE
Mg- H2O-rich fluid (Dehydration)
Ca- CO2-rich fluid (Decarbonation)
SiO2-rich fluid (Sedimentary source)
Channelized H2O-rich fluid (Deep source)
Carbonation of serpentinite clasts

Fig. 12

Table 1 - List of rock samples selected for petrographic and microstructural analyses. Samples analysed by EMPA, IRMS, XRD, and Microraman are also indicated. The term "lithon" is referred to "microlithons". Abbreviations: spo – shape preferred orientation, Dx – deformative phase X, Sx – foliation X, Lx – mineral or aggregate lineation X.

Lithostratigraphic unit	Sample	Thin section	Lithology	Textural occurrence	Mineralogical abundances (%)	Microstructures	EMPA	IRMS	XRD	Micro-Raman
Serpentinite – metaophicarbonate basement	MIS17-B-1	B1	Foliated serpentinite	Main rock	Srp 70-75%; Dol ± Mgs 25%; Op 5%	Axial plane S_2: Srp spo; L_2: Op/Dol spo	X		X	X
	MIS17-B-2	B2	Foliated serpentinite	Main rock	Srp ~ 85%; Op 5%	Axial plane S_2: Srp spo; L_2: Op/Dol spo; S-C and S-C' shear bands				
	MIS17-B-3	B3	Metaophicarbonate	Srp-rich portion	Srp 65%; Dol 30%; Tlc <5%; Op <5%					
	MIS17-B-4	B4	Metaophicarbonate	Dol-rich portion	Dol 75%; Srp 20% Tlc <5%; Op <5%					
	MIS17-C-1	C1	Massive serpentinite	Main rock	Srp 35-40%; Chl 25%; Cpx 20%; Opx 5%; Op 10%; Cal <5%; Rt <1%	L_2: Cpx+Opx+Op spo	X		X	X
	MIS17-C-2	C2	Foliated serpentinite	Main rock	Srp 65-70%; Chl 15%; Op 15%, Cpx ± Opx 5%; Rt <1%	S_1: Op spo; S_2: Srp+Chl+Op spo; L_2: Op spo; S-C shear bands			X	
	MIS17-C-4a	C4A	Metaophicarbonate	Intrafoliar Srp+Amp vein	Amp 50%; Srp 35%; Cpx 10%; Op <5%; Chl?; Cal?					
	MIS17-C-4b	C4B	Metaophicarbonate	Contact between extensional Dol+Cpx+Cal vein (1) and C4A vein (2)	*Vein 1:* Dol 65%; Cpx 20%; Cal 10%; Amp <5% *Vein 2:* Amp 70-75%; Srp 10%; Cal ~5-10%; Cpx ~ 5%; Op <5%					
	MIS17-C-6	C6	Metaophicarbonate	Shear Cal vein in contact with the main rock (C2 type)	*Vein:* Cal 90%; Cpx <5%; Srp <5%; Amp<5%; Op <5%	S-C structures within the contact				
	MIS17-C-7b	C7B	Metaophicarbonate	Carbonate vein of last stage	Cal 90%; Dol 10%	Dol porphyroblast replaced by Cal				
	MIS17-Carb2	CRB2	Foliated serpentinite	Main rock	Srp 60%; Dol ± Mgs 25%; Cal 10%; Op 5%; Tlc <5%	Axial plane S_2: Srp spo; L_2: Op/Dol spo; Cal micro veins	X			
Metasomatic horizon (MH)	MIS17-B-5	B5	MH1	"Brecciated" layer	Amp 40%; Dol 25-30%; Cal 15-20%; Chl 5-10%; Ttn <5%; Op <5%		X			
	MIS17-B-6	B6	MH2	Contact between boudin neck and boudinated clast/layer	*Neck:* Cpx 45-50%; Dol 35-40%; Cal 15-20%; Op <5% - *Clast:* Dol+Cal 55%; Amp 15-20%; Chl 5-10%; Op 5%	*Vein:* Cpx+Dol spo // to S_2 (thus to the extension direction); *Clast:* axial plane S_2 by Dol and Amp+Chl+Op spo				
	MIS17-B-8	B8	MH2	Transposed clast embedded within the main rock	Amp 70%; Dol 10%; Op 5-10%; Chl <5%; Cal <5%	S_1: contact between Dol+Op and Amp (?); S_2: transposed layering between Dol+Op and Amp; Dol → Amp II at high angle to S_2 (conjugate?)	X			
	MIS17-B-10a	B10A	MH2	Transposed clast in contact with Cb matrix	Amp 40%; Dol 20%; Cal 15%; Op 10%; Cpx <5%; Chl <1%	*Clast:* axial plane S_2 by Amp spo and Op films; D_2 isoclinal fold hinge; *Matrix:* Dol spo // to S_2				
	MIS17-B-10b	B10B	MH2	Main rock	Dol 45-50%; Cal 25%; Amp 15-20%; Op <10%; Chl <5%	Axial plane S_2: Dol aggregate bands, Amp spo and Op films; S-C shear bands				
	MIS17-B-11	B11	MH2	Main rock	Dol 35%; Amp 25%; Cal 20-15%; Chl <10%; Op <10%; Srp <5%	Axial plane S_2: Dol±Cal aggregate bands, Amp spo and Op±Srp films; D_2 isoclinal fold hinge	X			
	MIS17-B-12	B12	MH2	Block embedded within the main rock	Dol 35-40%; Amp 30%; Cal 20%; Chl 5%; Op <5%; Tlc <1%					
	MIS17-B-13a	B13A	MH2	Disrupted level	Dol 30%; Cal 20%; Amp 20%; Cpx 15-20%; Op <10%; Chl 5%; Srp <1%	Axial plane S_2: Dol±Cal aggregate bands, Amp spo and Op±Srp films; $S_{2\text{-}n}$ (by Cpx+Op) within Dol lithons; S-C shear bands; Cal vein				
	MIS17-B-13b	B13B	MH2	Disrupted level	Chl 40%; Cpx 25%; Dol 10-15%; Cal 10%; Amp <10%; Op <5%	Axial plane S_2 by Chl and Dol±Cal aggregate bands, Cpx spo and Op films; D_2 isoclinal fold hinge; Cal shear vein	X			
	MIS17-E-7	E7	MH2	Block embedded within the main rock	Amp 55%; Dol+Cal 25-30%; Chl 10%; Op 5%	S_2: Amp spo folded by asymmetric D_3 folds, with syn- to post-D_3 (?) S-C shear bands				
	MIS17-E-8	E8	MH3	Epidote-rich domain	Amp 55%; Ep 20% (pistacite > zoisite); Cal 15-20%; Tlc 5%; Cpx <5%; Op <1%	Poikilitic Cal; hydrofractured Amp grains				
	MIS17-E-9	E9	MH1	"Brecciated" layer	Dol 80%; Amp 10-15%; Cal <5%; Op <5%; Tlc <5%; Chl/Srp <1%			X		X
	MIS17-H-4	H4	MH3	Amp matrix in contact with Cb-rich domain	Cal 50%; Dol 25%; Amp 15%; Op 5%; Chl <5%; Cpx <5%; Srp < 5%	Continuous to spaced S_2 by Amp, Dol and Cal spo; L_2 by Op spo; S-C structures; Chl, Dol, Cal, Cpx aggregates sigmoids and Op δ-objects (fish)				
	MIS17-H-5	H5	MH3	Corse-grained Dol sigmoid within Amp-rich matrix	Dol ± Mgs 55%; Amp 35%; Cal 5%; Tlc <1%; Op <5%	S_2 by Amp spo; S-C shear bands; $S_{2\text{-}n}$ by Amp filling the pressure shadow of Dol porphyroblast	X			

Table 2 - Time relationships between deformation phases and stable mineralogical assemblages and/or microstructures for studied lithologies.
Mineral assemblages written in italic are inferred, not observed; Di* is Cpx crystallized from the decarbonation reaction; dr: dynamic recrystallization process.

Deformation phase / *Lithology*		**pre-D_1**	**D_1**	**D_2**	**D_3**	**post-D_3**
METASOMATIC HORIZON	**MH3**		Chl + Mag ± Srp ± Di Amp1? Dol1 ± Cal1/2?	Dol1 → Dol2 (dr) Amp2 ± Di* (Ep)	Amp3 Dol2 Ep Cal3	Cal3 Amp3/4?
	MH2		Chl + Mag + Di ± Srp Amp1? Dol1 ± Cal1/2?	Dol1 → Dol2 (dr) Amp2 ± Di*	Dol2 Amp3 Cal3?	Cal3 Amp3/4? • Cal3 vein
	MH1		Chl + Mag ± Srp ± Di Amp1? Dol1 ± Cal1/2?	Dol1 → Dol2 (dr) Amp2	Amp3 Cal3?	Cal3 Amp3/4?
META-OPHICARBONATE		*Spl (Al-Chr) + Ol + Cpx (Aug) + Opx + Pl → Srp0 ± Chl ± Mgs ± Dol0/Cal*	*Srp0* → Srp1 Fe-Chr → Mag *Mgs ± Dol0/Cal* → Dol1 *Aug* → Di	Srp1 → Srp2 Veins: • Intrafolial Srp2 • Dol1-Dol2, Di* in tension gash	Veins: • Dol1-Dol2, Di* in tension gash • Cal3 shear vein	Cal3 • Cal3 shear vein
SERPENTINITE		*Spl (Al-Chr) + Ol + Cpx (Aug) + Opx + Pl → Srp0 ± Chl (± Mgs ± Dol0/Cal)*	*Srp0* → Srp1 Al-Chr → Fe-Chr → Mag? Mgs ± *Dol0/Cal* → Dol1 *Aug* → Di	Srp1 → Srp2 Dol1 → Dol2 (dr) Di → Amp Srp2 + Di + Chl + Mag	Srp2 + Di + Chl + Mag Dol2	Cal3 • Srp vein

Figure S1: X-ray powder diffraction (XRD) patterns of the three analysed serpentinite samples C1 (massive serpentinite, a), B1 and C2 (foliated serpentinite, b and c respectively).

(a)

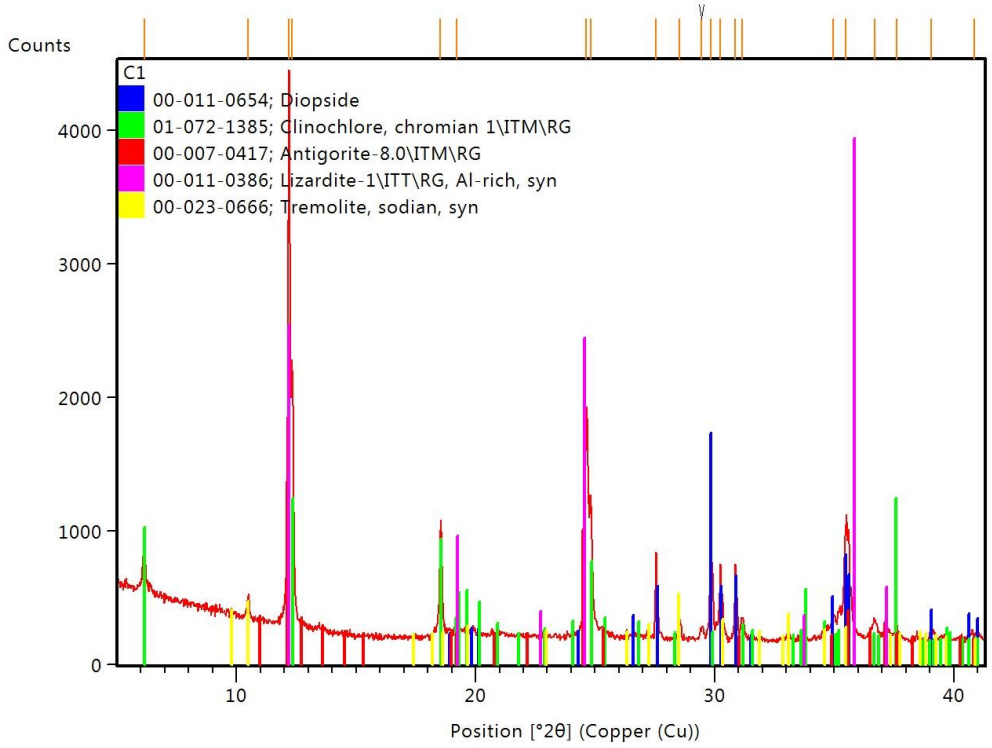

(b)

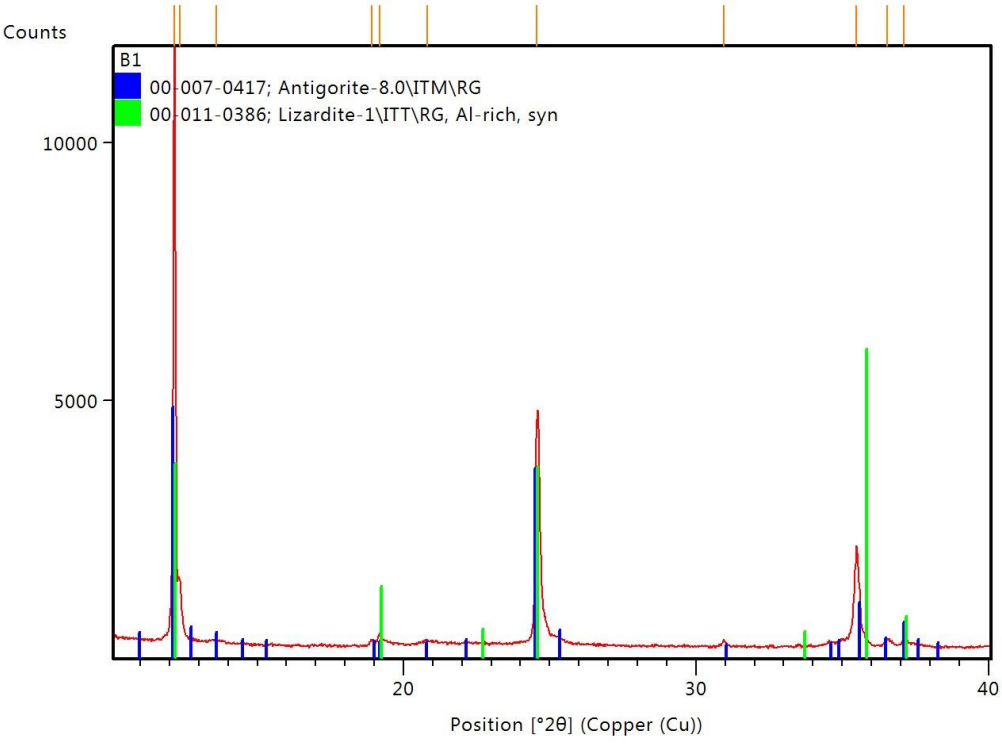

(c)

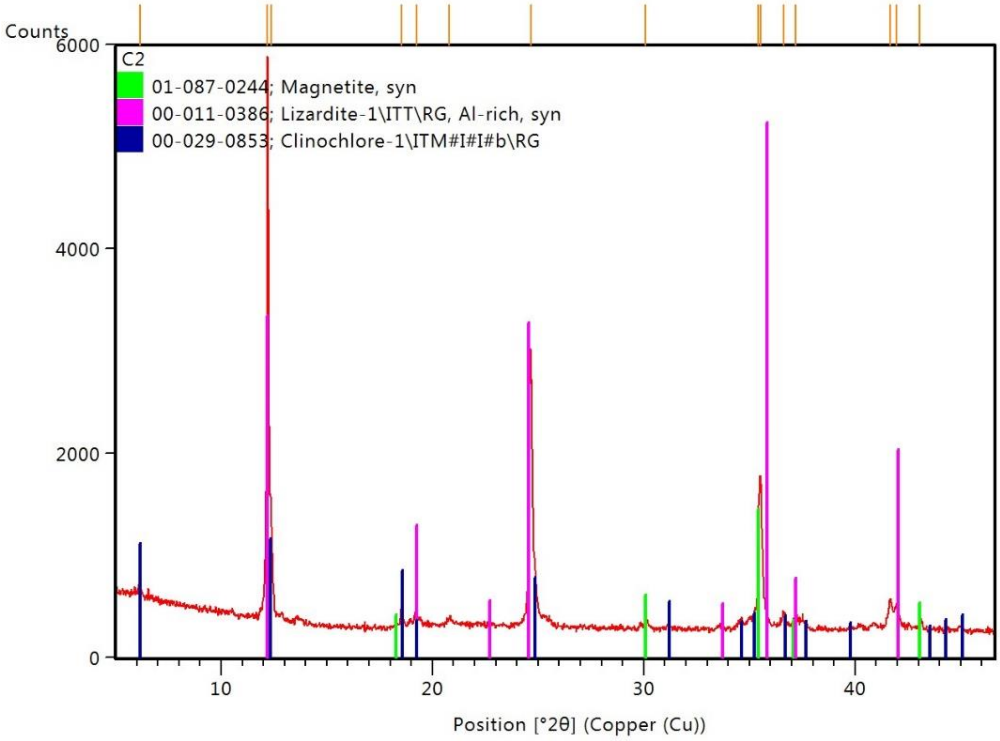
Counts
6000
4000
2000
0
C2
01-087-0244; Magnetite, syn
00-011-0386; Lizardite-1\ITT\RG, Al-rich, syn
00-029-0853; Clinochlore-1\ITM#I#I#b\RG
10
20
30
40
Position [°2θ] (Copper (Cu))

Figure S2: Samples analysed for the stable isotope compositions of carbonates (see Tab. S7), with cathodoluminescence (CL) analyses performed on samples MIS64bis and MIS46 to distinguish the carbonate stages of crystallization.

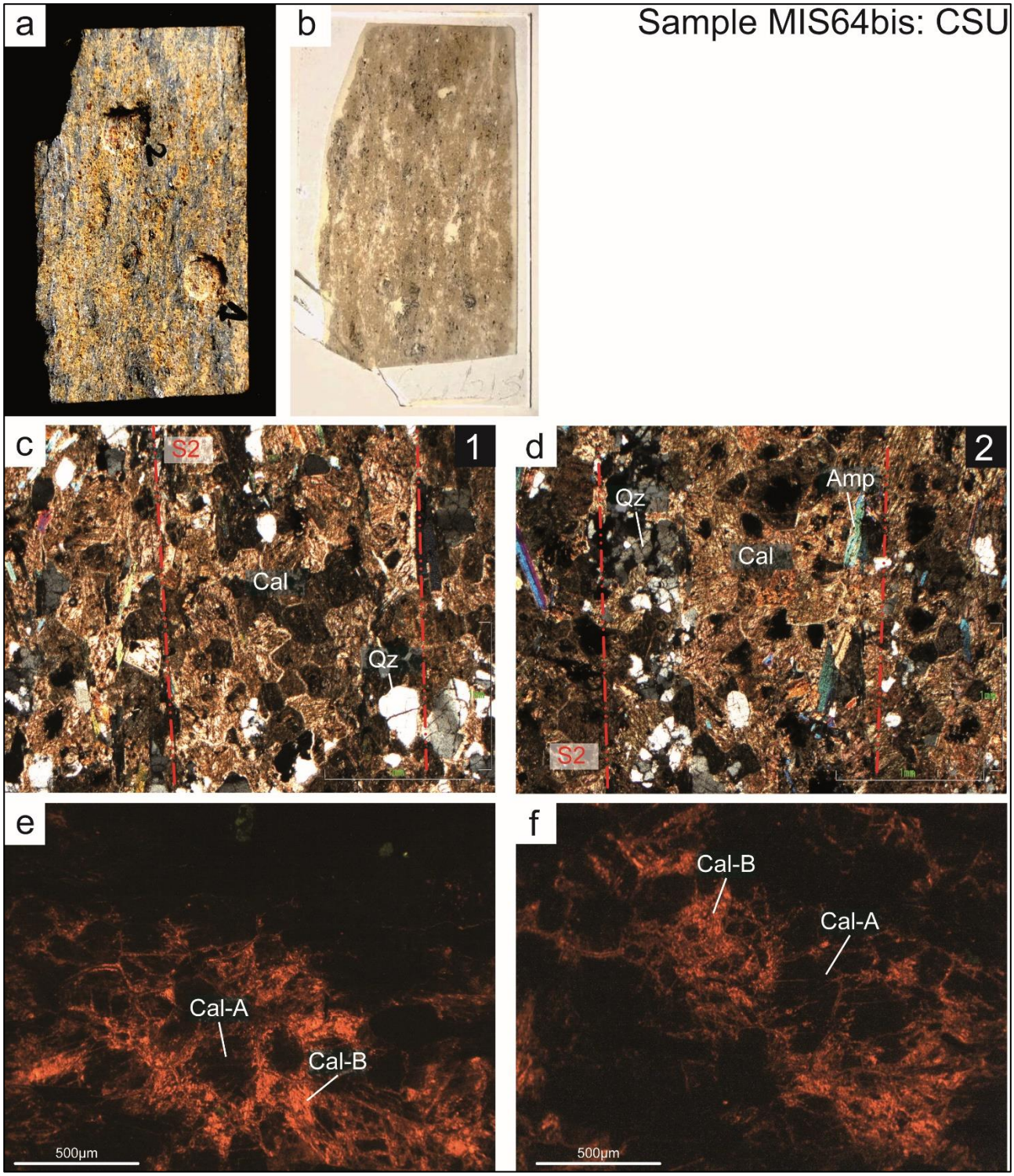

SAMPLE MIS64bis: (a) rock billet and (b) thin section (2.8 x 4.7 cm) with the drilled sites.
Photomicrographs in cross-polarized light, 2.5x zoom: (c) site 1, Cal fine-grained polygonal aggregate within calcschist microlithons; (d) site 2, Cal aggregate with Qz+Wm±Chl; (e-f) cathodoluminescence (CL) imaging of calcite microlithons, Cal-A generation is constituted by euhedral turbid crystals from dull to non luminescent, Cal-B limpid generation is the final growth rims of Cal-A crystals with bright luminescence.

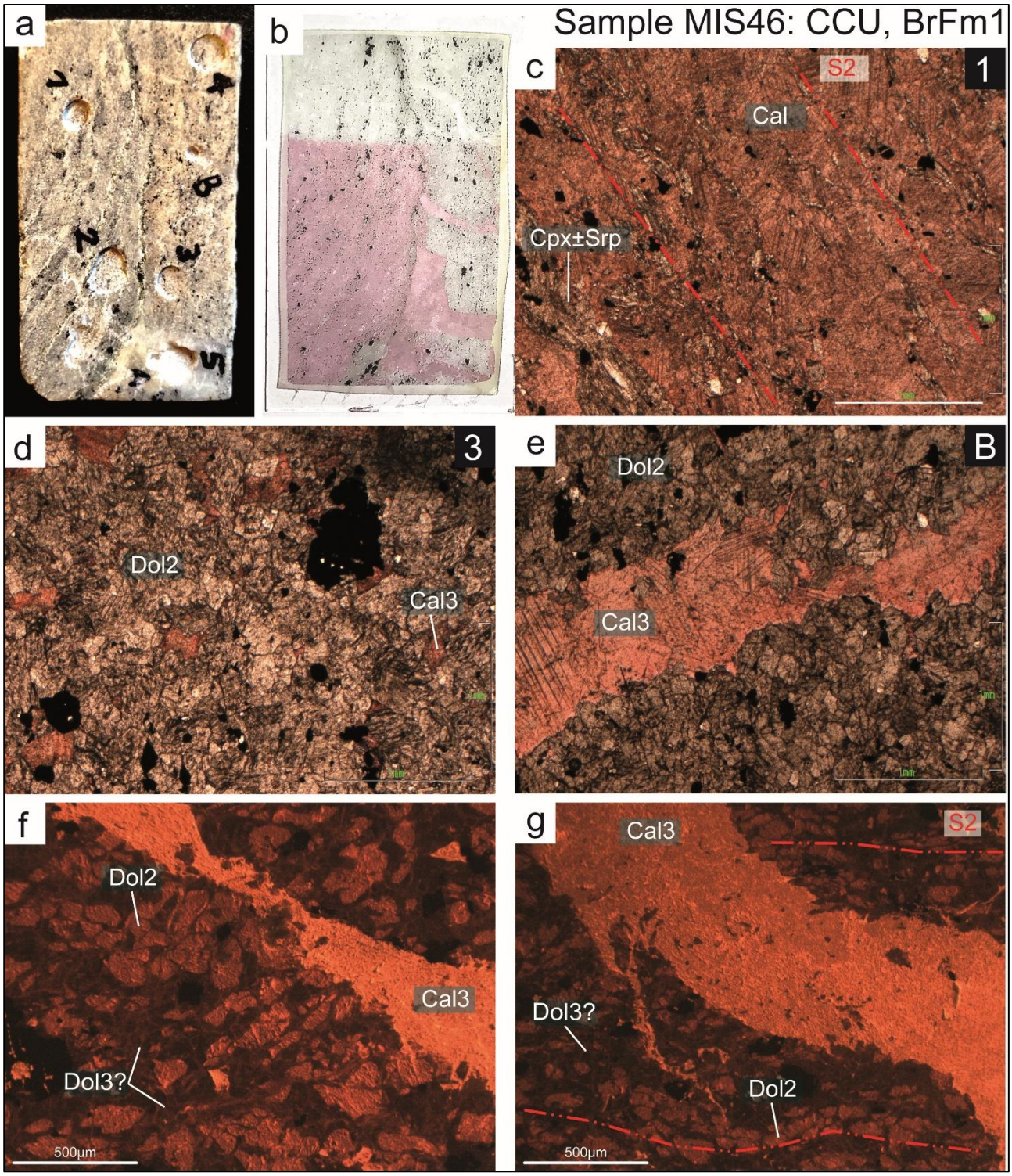

SAMPLE MIS46: (a) rock billet and (b) thin section (2.8 x 4.7 cm) with the drilled sites.
Photomicrographs in plain-polarized light, 2.5x zoom: (c) site 1, Cal equigranular aggregates replacing primary mineralogy within ultramafic clast; (d) site 3, Dol2 fine-grained matrix replaced by Cal3; (e) site C, coarse-grained Cal3 filling a late, exhumation stage vein that crosscut the Dol2 matrix. "Alizarin Red S" (ARS, chemical formula: $C_{14}H_8O_6$) dye has been used to discriminate calcite from dolomite because of their different staining response (calcite becomes pink orange; dolomite does not react; Dickson, 1966). (f-g) Cathodoluminescence (CL) imaging of Dol2 matrix and late Cal3 vein. Dol2 is made of turbid, subhedral grains from bright to dull luminescent, marking the S_2 foliation with their SPO, and of a dull to non luminescent matrix (subsequent Dol3 recrystallization?) embedding the Dol2 grains. Cal3 is bright luminescent indicative of abundance of Mn^{2+} due to precipitation in reducing environment.

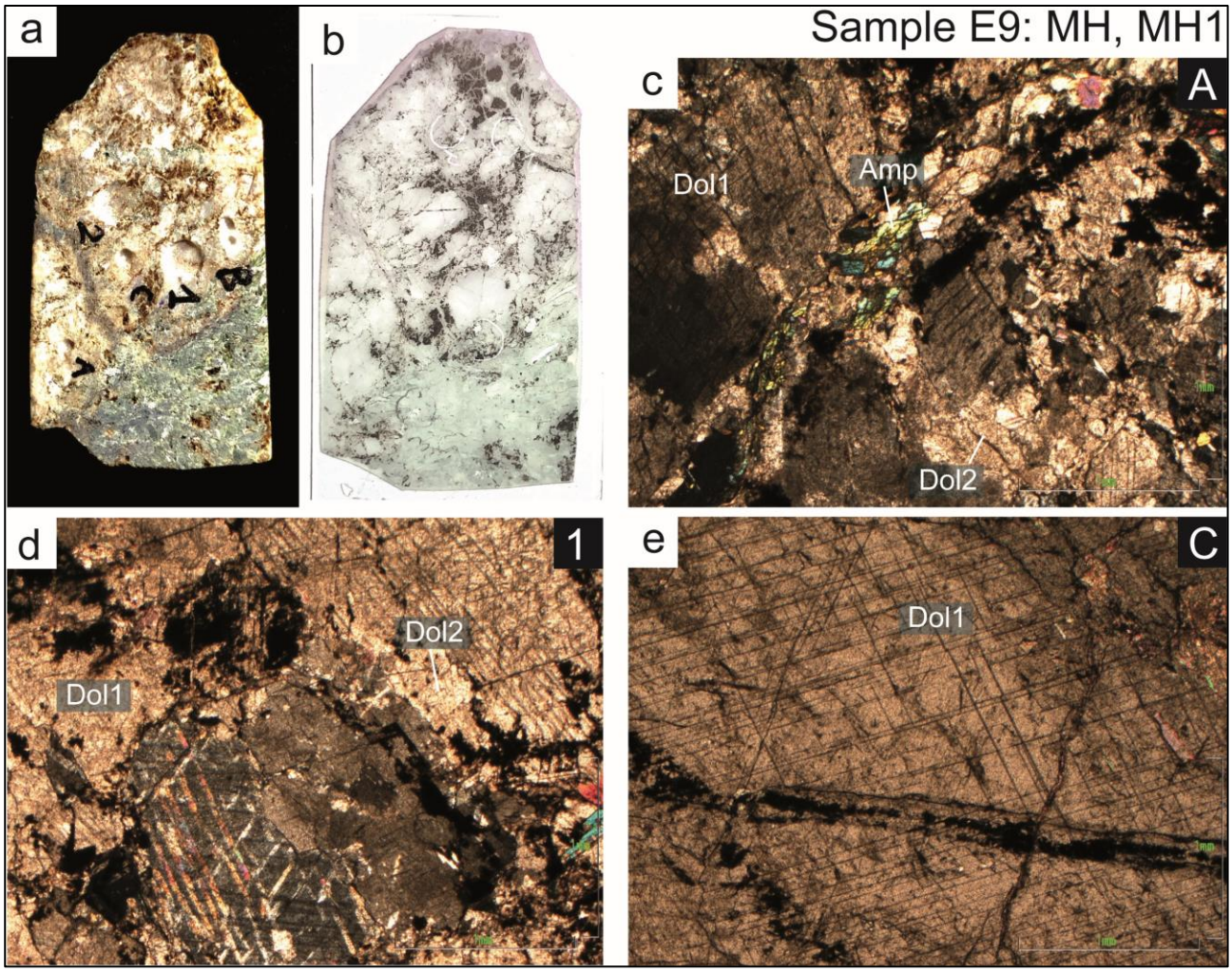

SAMPLE E9: (a) rock billet and (b) thin section (2.8 x 4.7 cm) with the drilled sites.
Photomicrographs in cross-polarized light, 2.5x zoom: (c) site A and (d) site 1, Dol1 porphyroblasts with some dynamic recrystallization and Amp at grain boundaries; (e) site C, coarse-grained Dol1 porphyroblast, with opaque inclusions and fractures. "Alizarin Red S" (ARS, chemical formula: $C_{14}H_8O_6$) dye has been used to discriminate calcite from dolomite because of their different staining response (calcite becomes pink orange; dolomite does not react; Dickson, 1966).

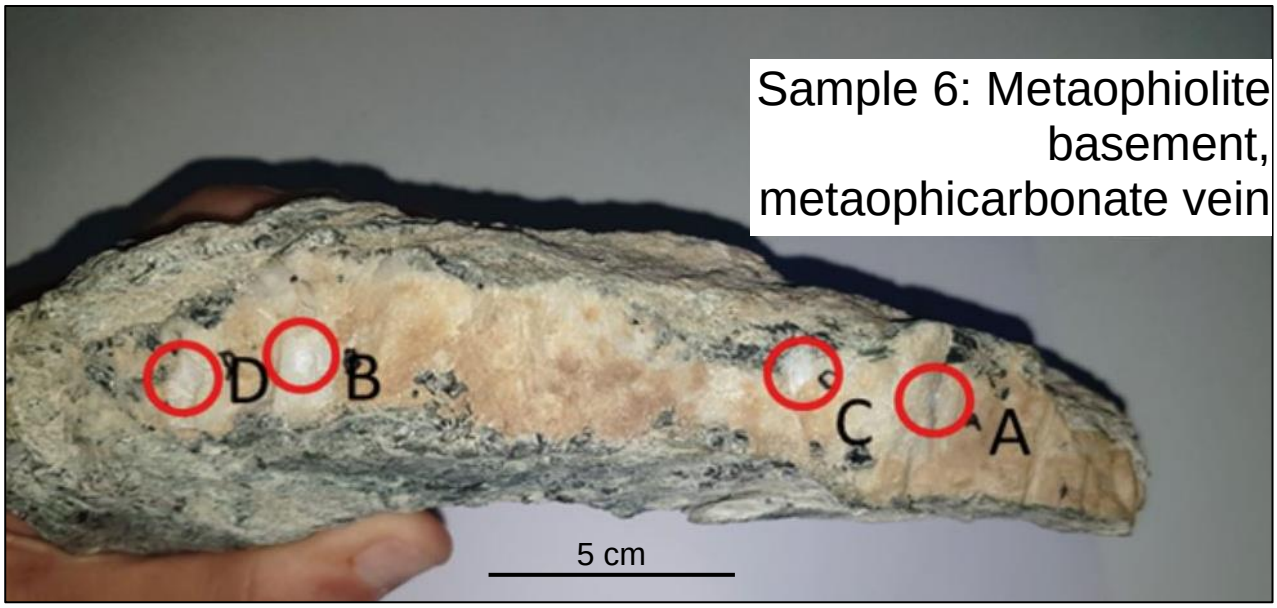

SAMPLE 6: hand sample of metaophicarbonate from the metaophiolite basement. Red circles: drill sites within an intrafolial syn-D_2 carbonate (calcite) vein.

Figure S3: Raman spectra of the three different serpentine polymorphs taken as reference for this study (sample L2-C1 for lizardite and chrysotile; sample L2-C5 for antigorite; from Campomenosi, unpublished data). Lz = lizardite; Atg = antigorite; Ctl = chrysotile. (a) shows the low wavenumber region (100 – 1100 cm^{-1}) related to the internal lattice vibrations while (b) shows the high wavenumber region (3500 – 3800 cm^{-1}) pertaining to the OH vibrations.

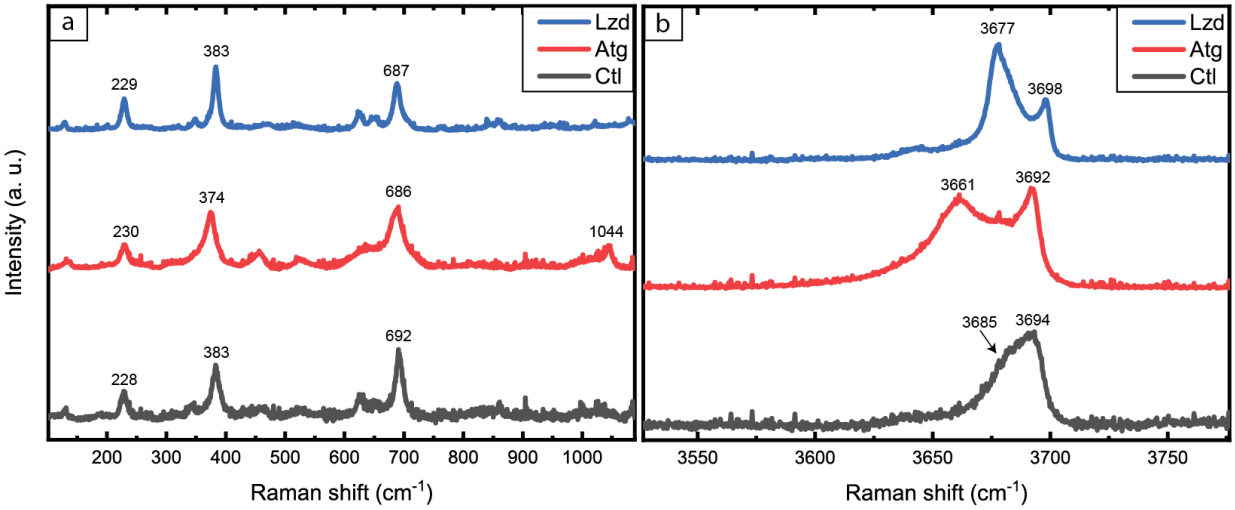

Figure S4: BSE images of zoned Dol in MH1 (a, sample B5) and zoned Mgs in foliated serpentinite (b, sample B1). See also Table S3 for analysis points.

(a)

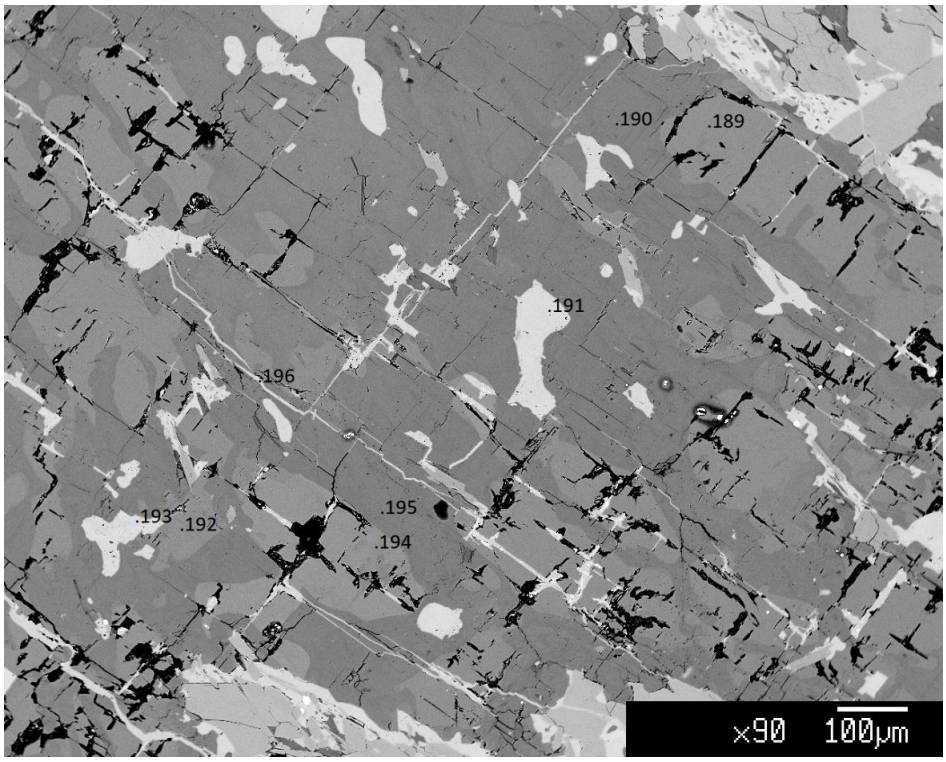

Dark grey (e.g., analysis point 195, 190): Dol1 zoned core.
Light grey (e.g., analysis point 194, 189): Dol1 zoned rim.

(b)

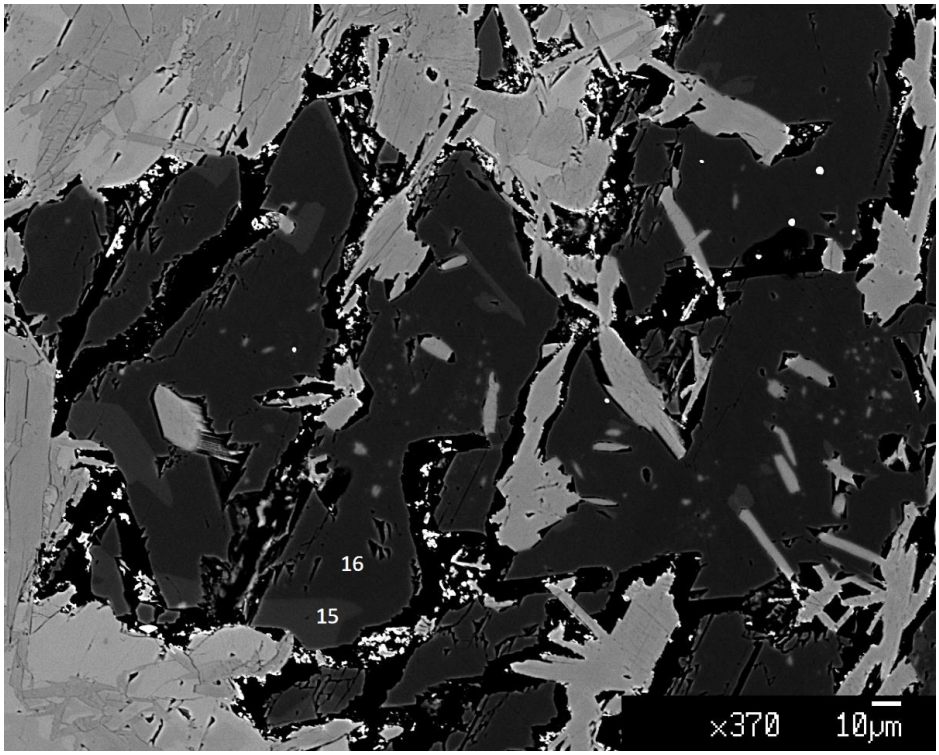

Dark grey (e.g., analysis point 16): Mgs zoned core.
Light grey (e.g., analysis point 15): Mgs zoned rim.

Table S1. Representative analyses of serpentine and talc mineral chemistry (EMPA) in Champorcher valley serpentinites and metasomatic horizon.

	Serpentine											Talc		
Lithology	Foliated serp.	Foliated serp.	Foliated serp.	Massive serp.	Massive serp.	Massive serp.	Massive serp.	Massive serp.	Massive serp.	Massive serp.	Massive serp.	MH3	MH3	MH3
Sample	B1-S1-7	B1-S2-10	B1-S4-19	C1-S1-63	C1-S2-70	C1-S4-89	C1-S5-98	C1-S6-110	C1-S7-114	C1-S8-115	C1-S8-127	H5-S2-272	H5-S4-307	H5-S5-314
Mineral	Atg	Atg	Atg	Atg	Atg	Atg	Atg/Chl	Atg/Lz	Atg	Atg/Lz	Atg/Lz	Tlc	Tlc	Tlc
Textural occurrence	Srp1 (bastite on Opx)	Srp2 // S2	Srp2 // S3	Inclusion in Cpx	Srp1 (bastite on Opx)	Srp1 (bastite on Opx)	Srp1 + Chl	Srp2 (matrix)	Srp1 (bastite on Opx)	Srp2 (vein)	Srp2 (matrix)	Replace Dol + Amp	Replace Dol + Amp	Replace Dol + Amp
wt.%														
SiO_2	43.43	43.32	42.95	41.82	42.02	39.53	34.85	41.49	40.94	42.38	42.50	61.59	61.68	61.52
TiO_2	0.04	0.02	0.02	0.03	bdl	bdl	0.01	bdl	0.08	bdl	bdl	bdl	0.05	0.02
Al_2O_3	0.89	0.55	1.25	3.15	2.68	4.15	11.77	2.68	2.77	2.26	2.64	0.04	0.06	0.12
Cr_2O_3	0.36	0.24	0.30	0.30	0.53	0.64	0.17	0.16	0.77	0.08	0.23	0.03	0.03	0.01
FeO	5.91	5.40	5.30	4.58	4.87	4.83	4.88	5.59	4.85	4.80	5.03	4.92	5.10	4.02
MnO	0.06	0.03	0.05	0.11	0.07	0.03	0.04	0.13	0.11	0.07	0.08	0.04	0.05	0.06
NiO	0.30	0.30	0.31	0.29	0.23	0.35	0.18	0.30	0.26	0.19	0.31	0.22	0.11	0.28
MgO	36.56	36.34	35.75	36.50	35.90	34.80	33.65	34.94	34.93	36.08	34.80	27.00	27.10	27.94
CaO	bdl	0.01	bdl	0.03	bdl	0.04	0.04	0.04	bdl	0.01	0.09	0.09	0.10	0.06
Na_2O	bdl	0.02	0.03	bdl	0.01	bdl	bdl	bdl	bdl	bdl	bdl	bdl	0.08	0.07
K_2O	bdl	0.01	bdl	bdl	0.02	bdl	0.01	bdl	bdl	0.02	bdl	bdl	0.04	0.02
H_2O (calc.)	12.54	12.38	12.32	12.52	12.41	12.14	12.39	12.22	12.15	12.37	12.27	4.55	4.58	4.59
TOTAL	87.58	86.24	85.95	86.81	86.36	84.40	85.60	85.33	84.71	85.90	85.68	93.94 (*)	94.43	94.18
CATIONS calculated on the basis of 116 OXYGENS														
Si	33.891	34.205	34.000	32.733	33.101	31.974	27.844	33.179	32.926	33.471	33.668	8.110	8.077	8.035
Ti	0.024	0.012	0.012	0.018	bdl	bdl	0.006	bdl	0.048	bdl	bdl	bdl	0.005	0.002
$Al^{(IV)}$	0.109	bdl	bdl	1.267	0.899	2.026	6.156	0.821	1.074	0.529	0.332	bdl	bdl	bdl
$Al^{(VI)}$	0.710	0.512	1.166	1.639	1.589	1.930	4.927	1.705	1.552	1.574	2.133	0.006	0.009	0.019
Cr	0.222	0.150	0.188	0.186	0.330	0.409	0.107	0.101	0.490	0.050	0.144	0.003	0.003	0.001
Fe^{2+}	3.857	3.566	3.509	2.998	3.208	3.267	3.261	3.739	3.262	3.170	3.332	0.542	0.559	0.439
Mn	0.040	0.020	0.034	0.073	0.047	0.021	0.027	0.088	0.075	0.047	0.054	0.005	0.006	0.007
Ni	0.188	0.191	0.197	0.183	0.146	0.228	0.116	0.193	0.168	0.121	0.198	0.023	0.012	0.029
Mg	42.525	42.769	42.182	42.583	42.152	41.955	40.072	41.647	41.873	42.472	41.091	5.299	5.289	5.439
Ca	bdl	0.009	bdl	0.025	bdl	0.035	0.034	0.034	bdl	0.009	0.076	0.013	0.014	0.008
Na	bdl	0.031	0.046	bdl	0.015	bdl	bdl	bdl	bdl	bdl	bdl	bdl	0.020	0.018
K	bdl	0.010	bdl	bdl	0.020	bdl	0.010	bdl	bdl	0.020	bdl	bdl	0.007	0.003
Sum cations	81.565	81.473	81.334	81.704	81.508	81.844	82.560	81.507	81.468	81.463	81.028	14.000	14.000	14.000
#Mg(Fe^{2+})	0.917	0.923	0.923	0.934	0.929	0.928	0.925	0.918	0.928	0.931	0.925	0.907	0.904	0.925
Al	0.819	0.512	1.166	2.906	2.488	3.956	11.083	2.526	2.626	2.104	2.465			
y(Atg)	0.10	0.06	0.15	0.36	0.31	0.49	1.39	0.32	0.33	0.26	0.31			

*(*) CATIONS calculated on the basis of 20 OXYGENS*

(bdl) = below the detection limit (0.01 wt.% for all oxides).

Mineral abbreviations adopted from Whitney and Evans (2010). Serp. = serpentinite

Atg normalized to 116 oxygen assuming a polysome m = 17 and an ideal polysomatic formular $M_{3m-3}T_{2m}O_{5m}(OH)_{4m-6}$ *(from Padrón-Navarta et al., 2013).*

#Mg(Fe^{2+}) = Mg/(Mg+Fe^{2+}); Al = $Al^{(IV)}$ + $Al^{(VI)}$; y(Atg) = Al/8

Table S2. Representative analyses of amphibole mineral chemistry (EMPA) in Champorcher valley serpentinites and metasomatic horizoı

Lithology	MH1	MH1	MH1	MH2	MH2	MH2	MH2	MH2	MH2	Massive serp.	MH3	MH3	MH3	MH3
Sample	B5-S1-168	B5-S2-46	B5-S4-54	B8-S1-27	B8-S3-39	B11-S1-207	B11-S2-214	B13-S1-131	B13-S5-160	C1-S3-81	H5-S2-276	H5-S3-287	H5-S3-288	H5-S4-299
Mineral*	Tr	Act	Act	Tr	Tr	Tr	Tr	Tr	Tr	Tr	Tr	Act	Act	Act
Textural occurrence	Boudin replaced by Cal	Replace Dol	Replace Dol	⊥ S2 with Dol	⊥ S2	// S2	Boudin // S2	Replace Cpx	Replace Cpx	Replace Cpx	Zoned (core) ⊥ S2	Zoned (rimI) ⊥ S2	Zoned (rimII) ⊥ S2	// S2 with Tlc
wt.%														
SiO_2	55.90	*57.57*	*58.24*	*58.55*	*58.16*	*58.25*	58.13	*59.03*	*58.25*	*58.67*	*58.80*	56.03	*57.88*	56.78
TiO_2	bdl	0.05	0.04	bdl	0.05	bdl	0.01	0.05	bdl	0.05	0.04	0.02	bdl	0.01
Al_2O_3	0.51	0.47	0.44	0.15	0.12	0.31	0.25	0.07	0.05	0.11	0.03	0.73	0.28	0.66
Cr_2O_3	0.15	0.10	0.02	0.11	0.08	0.05	0.05	0.01	0.05	0.00	0.03	0.29	0.08	0.19
Fe_2O_3	bdl	bdl	bdl	bdl	bdl	bdl	bdl	bdl	bdl	bdl	bdl	bdl	bdl	bdl
FeO	5.12	5.05	4.72	3.81	3.47	3.56	3.81	2.39	2.67	1.39	2.21	8.76	5.63	6.45
MnO	0.13	0.05	0.08	0.01	0.05	0.05	bdl	0.03	0.05	0.10	0.07	0.08	0.12	0.13
NiO	0.22	0.22	0.24	0.21	0.22	0.29	0.08	0.16	0.17	0.04	0.15	0.17	0.17	0.22
MgO	20.97	20.06	20.66	21.70	21.55	21.41	21.77	22.50	22.45	23.06	22.66	17.87	20.53	19.95
CaO	12.85	12.78	12.90	12.81	13.04	13.09	13.23	13.51	13.46	13.54	13.32	11.27	12.52	12.03
Na_2O	0.40	0.51	0.38	0.38	0.34	0.27	0.28	0.03	0.07	0.08	0.13	0.80	0.36	0.57
K_2O	0.03	0.06	0.07	0.03	0.09	0.02	0.05	0.01	0.05	0.01	0.05	0.16	0.17	0.12
H_2O	2.12	2.12	2.15	2.16	2.15	2.16	2.17	2.19	2.17	2.18	2.18	2.07	2.14	2.12
TOTAL	96.29	96.94	97.80	97.82	97.21	97.34	97.68	97.82	97.26	97.06	97.48	96.19	97.76	97.10
CATIONS calculated on the basis of 23 OXYGENS and 15 CATIONS + K														
Si	7.837	*8.051*	*8.062*	*8.059*	*8.057*	*8.063*	8.008	*8.095*	*8.032*	*8.063*	*8.076*	8.010	*8.044*	7.950
Ti	bdl	0.005	0.004	bdl	0.005	bdl	0.001	0.005	bdl	0.005	0.004	0.002	bdl	0.001
Al	0.084	0.078	0.072	0.024	0.020	0.051	0.041	0.011	0.008	0.018	0.005	0.123	0.046	0.109
Cr	0.017	0.011	0.002	0.012	0.009	0.006	0.005	0.001	0.006	0.000	0.003	0.033	0.009	0.021
Fe^{3+}	0.328	bdl	bdl	bdl	bdl	bdl	0.003	bdl	bdl	bdl	bdl	0.013	bdl	0.101
Fe^{2+}	0.273	0.591	0.546	0.439	0.402	0.412	0.437	0.274	0.308	0.160	0.254	1.035	0.654	0.655
Mn	0.015	0.006	0.009	0.001	0.006	0.006	bdl	0.004	0.006	0.012	0.008	0.010	0.014	0.015
Ni	0.025	0.025	0.027	0.023	0.025	0.032	0.009	0.018	0.019	0.004	0.017	0.020	0.019	0.025
Mg	4.382	4.181	4.263	4.452	4.450	4.417	4.470	4.599	4.614	4.724	4.639	3.808	4.253	4.164
Ca	1.930	1.915	1.913	1.889	1.936	1.941	1.953	1.985	1.989	1.994	1.960	1.726	1.864	1.805
Na	0.109	0.138	0.102	0.101	0.091	0.073	0.075	0.008	0.019	0.021	0.035	0.222	0.097	0.155
K	0.005	0.011	0.012	0.005	0.016	0.004	0.009	0.002	0.009	0.002	0.009	0.029	0.030	0.021
H	2.000	2.000	2.000	2.000	2.000	2.000	2.000	2.000	2.000	2.000	2.000	2.000	2.000	2.000
Sum cations	15.005	15.011	15.012	15.005	15.016	15.004	15.009	15.002	15.009	15.002	15.009	15.029	15.030	15.021
#Mg(Fe^{2+})	0.941	0.876	0.886	0.910	0.917	0.915	0.911	0.944	0.937	0.967	0.948	0.786	0.867	0.864
#Mg(Fe_{tot})	0.880	0.876	0.886	0.910	0.917	0.915	0.911	0.944	0.937	0.967	0.948	0.784	0.867	0.846
Fe^{3+}/Fe_{tot}	0.546	–	–	–	–	–	0.006	–	–	–	–	0.012	–	0.133
Al^{IV}	0.084	–	–	–	–	–	–	–	–	–	–	–	–	0.050
Al^{VI}	0.000	0.128	0.133	0.083	0.077	0.113	0.048	0.106	0.040	0.081	0.081	0.133	0.090	0.059
Na^{M4}	0.070	0.085	0.087	0.101	0.064	0.059	0.047	0.008	0.011	0.006	0.035	0.222	0.097	0.155

** From the classifications of Leake et al. (1997, 2004)*

(bdl) = below the detection limit (0.01 wt.% for all oxides).

Mineral abbreviations adopted from Whitney and Evans (2010). Serp. = serpentinite

SiO_2 and Si values in excess are reported in italic.

#Mg(Fe^{2+}) = Mg/(Mg+Fe^{2+}); #Mg(Fe_{tot}) = Mg/(Mg+Fe_{tot})

Table S3. Representative analyses of carbonates and titanite mineral chemistry (EMPA) in Champorcher valley serpentinites and metasomatic horizon.

	Calcite														**Dolomite**		
Lithology	MH1	MH1	MH1	MH1	MH2	MH2	MH2	MH2	MH2	MH2	Massive serp.	MH3	MH3	MH3	Foliated serp.	Foliated serp.	MH1
Sample	B5-S1-41	B5-S1-166	B5-S4-178	B5-S5-191	B5-S3-34	B11-S1-210	B11-S2-219	B11-S3-227	B11-S4-239	B13-S2-137	C1-S5-92	H5-S2-279	H5-S3-286	H5-S4-306	B1-S2-9	B1-S3-17	B5-S1-42
Mineral	Cal	Cal	Cal	Cal	Cal	Cal	Cal	Cal	Cal	Cal	Cal	Cal	Cal	Cal	Dol	Dol	Dol
Textural occurrence	Cal fracture in Dol1	In Amp boudin neck	Replace Amp	Replace Dol1	Replace Dol	Replace Dol2	In Amp boudin neck	Replace Amp	In Mag boudin neck	Replace Dol2	Micro-vein	Cal fracture in Dol1	Inclusion in Amp	Replace Dol	Replace Mgs	Micro-fracture	porphyro blast (Dol1)
wt.%																	
SiO_2	bdl	0.11	bdl	0.02	0.02	0.02	0.04	0.05	0.04	0.03	0.43	0.01	0.09	0.05	0.03	0.02	0.02
TiO_2	0.02	0.06	0.03	0.03	bdl	0.05	0.02	bdl	bdl	0.01	bdl	bdl	bdl	bdl	0.02	bdl	0.02
Al_2O_3	0.01	bdl	0.02	bdl	bdl	0.01	0.03	bdl	0.02	0.01	0.03	0.10	bdl	bdl	0.01	bdl	bdl
Cr_2O_3	bdl	0.02	0.02	bdl	bdl	0.03	bdl	bdl	0.05	bdl	0.07	bdl	bdl	0.03	bdl	bdl	bdl
Fe_2O_3	0.05	bdl	bdl	bdl	bdl	bdl	bdl	bdl	bdl	bdl	bdl	bdl	bdl	bdl	bdl	bdl	bdl
FeO	0.31	0.78	0.55	0.37	0.85	0.49	0.67	0.46	0.54	0.35	0.24	0.87	0.94	0.44	2.17	2.06	2.41
MnO	0.25	0.26	0.25	0.06	0.17	0.25	0.20	0.17	0.18	0.14	0.15	0.49	0.38	0.39	0.34	0.40	0.34
MgO	0.50	1.17	1.07	1.02	1.62	0.77	0.76	0.73	0.42	0.93	0.41	0.77	1.34	0.41	22.08	21.38	21.98
CaO	62.61	57.86	61.19	60.37	56.21	57.94	57.91	55.54	55.34	60.39	57.42	56.96	54.87	58.63	31.39	31.36	31.40
Na_2O	bdl	0.01	0.01	0.02	bdl	bdl	bdl	bdl	0.01	bdl	0.04	bdl	0.01	bdl	bdl	bdl	0.03
K_2O	0.06	bdl	bdl	bdl	0.01	0.01	bdl	0.01	bdl	bdl	bdl	bdl	0.01	0.01	bdl	bdl	bdl
CO_2 (calc.)*	36.19	39.73	36.86	38.11	41.12	40.43	40.37	43.04	43.40	38.14	41.21	40.80	42.36	40.04	-3.76	47.26	-3.74
TOTAL	63.81	60.27	63.14	61.89	58.88	59.57	59.63	56.96	56.60	61.86	58.79	59.20	57.64	59.96	103.76	52.74	103.74
CATIONS calculated on the basis of 6 OXYGENS																	
Si	bdl	0.010	bdl	0.002	0.002	0.002	0.004	0.005	0.004	0.003	0.041	0.001	0.009	0.005	0.003	0.002	0.002
Ti	0.001	0.004	0.002	0.002	bdl	0.004	0.001	bdl	bdl	0.001	bdl	bdl	bdl	bdl	0.001	bdl	0.001
Al	0.001	bdl	0.002	bdl	bdl	0.001	0.003	bdl	0.002	0.001	0.003	0.011	bdl	bdl	0.001	bdl	bdl
Cr	bdl	0.001	0.001	bdl	bdl	0.002	bdl	bdl	0.004	bdl	0.005	bdl	bdl	0.002	bdl	bdl	bdl
Fe^{3+}	0.003	bdl	bdl	bdl	bdl	bdl	bdl	bdl	bdl	bdl	bdl	bdl	bdl	bdl	bdl	bdl	bdl
Fe^{2+}	0.023	0.060	0.041	0.028	0.067	0.038	0.052	0.038	0.045	0.026	0.019	0.069	0.076	0.034	0.158	0.153	0.176
Mn	0.019	0.020	0.019	0.005	0.014	0.020	0.016	0.014	0.015	0.011	0.012	0.039	0.031	0.031	0.025	0.030	0.025
Mg	0.065	0.161	0.141	0.137	0.228	0.108	0.106	0.107	0.062	0.125	0.058	0.108	0.193	0.057	2.872	2.830	2.857
Ca	5.881	5.727	5.790	5.821	5.687	5.818	5.810	5.831	5.860	5.830	5.813	5.765	5.681	5.864	2.935	2.983	2.933
Na	bdl	0.002	0.002	0.003	bdl	bdl	bdl	bdl	0.002	bdl	0.007	bdl	0.002	bdl	bdl	bdl	0.005
K	0.007	bdl	bdl	bdl	0.001	0.001	bdl	bdl	bdl	bdl	bdl	bdl	0.001	0.001	bdl	bdl	bdl
Sum cations	6.000	5.986	5.997	5.998	5.999	5.994	5.993	5.994	5.994	5.996	5.959	5.993	5.993	5.995	5.996	5.998	5.999
X_{MgCO3}	0.011	0.027	0.024	0.023	0.038	0.018	0.018	0.018	0.010	0.021	0.010	0.018	0.032	0.010	0.481	0.474	0.479
X_{FeCO3}	0.004	0.010	0.007	0.005	0.011	0.006	0.009	0.006	0.007	0.004	0.003	0.012	0.013	0.006	0.027	0.026	0.029
X_{CaCO3}	0.985	0.963	0.970	0.972	0.951	0.976	0.973	0.976	0.982	0.975	0.987	0.970	0.955	0.985	0.492	0.500	0.492

MH1	MH1	MH2	MH2	MH2	MH2	MH2	MH2	MH2	MH3	MH3
B5-S5-194	B5-S5-195	B8-S1-25	B8-S2-30	B11-S1-197	B11-S2-224	B11-S5-260	B13-S2-136	B13-S3-144	H5-S1-267	H5-S4-303
Dol	Dol	Dol	Dol	Dol	Dol	Dol	Dol	Dol	Dol	Dol
Dol1 (zoned rim)	Dol1 (zoned core)	Dol2	Dol2	Dol2 in fold hinge	Dol2 in S2	Dol2 in fold hinge	Dol2 relic	Dol2 in micro-lithon	Dol1	replaced by Tlc + Cal
0.01	bdl	0.01	bdl	0.01	0.01	0.02	0.03	bdl	0.01	0.03
0.06	bdl	0.03	0.02	0.06	0.02	bdl	bdl	bdl	0.01	bdl
0.01	bdl	bdl	bdl	0.02	0.01	bdl	bdl	0.02	bdl	0.01
bdl	0.05	0.01	bdl	0.63	bdl	0.03	bdl	bdl	bdl	bdl
bdl	bdl	bdl	0.06	bdl	0.05	bdl	0.04	bdl	bdl	bdl
6.74	1.19	1.35	6.37	3.00	1.58	2.82	3.86	3.60	6.06	5.63
0.25	0.40	0.21	0.06	0.29	0.22	0.34	0.30	0.20	0.67	0.54
14.98	22.76	22.76	17.95	22.61	21.92	21.01	20.93	19.43	18.47	18.46
28.25	33.28	33.29	30.30	31.83	32.53	32.40	32.27	31.71	30.93	31.03
0.01	bdl	bdl	0.04	bdl	0.05	bdl	0.04	bdl	0.01	0.02
0.01	0.01	bdl	bdl	bdl	bdl	bdl	0.01	bdl	bdl	bdl
13.94	-8.00	-7.99	4.39	-6.13	-5.07	-3.72	-3.98	0.43	2.02	2.20
86.06	108.00	107.99	95.61	106.13	105.07	103.72	103.98	99.57	97.98	97.80
0.001	bdl	0.001	bdl	0.001	0.001	0.002	0.003	bdl	0.001	0.003
0.005	bdl	0.002	0.001	0.004	0.001	bdl	bdl	bdl	0.001	bdl
0.001	bdl	bdl	bdl	0.002	0.001	bdl	bdl	0.002	bdl	0.001
bdl	0.003	0.001	bdl	0.042	bdl	0.002	bdl	bdl	bdl	bdl
bdl	bdl	bdl	0.004	bdl	0.003	bdl	0.003	bdl	bdl	bdl
0.577	0.084	0.095	0.494	0.211	0.115	0.206	0.279	0.273	0.458	0.428
0.022	0.029	0.015	0.005	0.021	0.016	0.025	0.022	0.015	0.051	0.042
2.287	2.868	2.868	2.480	2.830	2.833	2.733	2.697	2.627	2.490	2.501
3.100	3.014	3.015	3.009	2.864	3.022	3.029	2.989	3.081	2.997	3.021
0.002	bdl	bdl	0.007	bdl	0.008	bdl	0.007	bdl	0.002	0.004
0.001	0.001	bdl	bdl	bdl	bdl	bdl	0.001	bdl	bdl	bdl
5.995	5.999	5.997	6.000	5.973	6.000	5.997	6.000	5.999	5.999	5.999
0.383	0.481	0.480	0.415	0.479	0.475	0.458	0.452	0.439	0.419	0.420
0.097	0.014	0.016	0.083	0.036	0.019	0.034	0.047	0.046	0.077	0.072
0.520	0.505	0.504	0.503	0.485	0.506	0.508	0.501	0.515	0.504	0.508

	Magnesite			
Lithology	Foliated serp.			
Sample	B1-S2-11	B1-S2-12	B1-S2-15	B1-S2-16
Mineral	Mgs	Mgs	Mgs	Mgs
Textural occurrence	Relic replaced by Dol	Relic replaced by Dol	Mgs (zoned rim)	Mgs (zoned core)
	wt.%			
SiO_2	0.03	0.05	bdl	0.01
TiO_2	bdl	0.01	0.01	0.04
Al_2O_3	0.02	bdl	0.01	bdl
Cr_2O_3	0.04	0.02	bdl	bdl
FeO	7.91	4.66	7.13	4.90
MnO	0.75	0.66	0.76	0.74
MgO	43.30	44.61	43.60	45.01
CaO	0.16	0.16	0.16	0.18
CO_2 (calc.)*	52.72	52.10	52.57	52.75
TOTAL	96.18	96.87	96.33	97.94
Si	0.002	0.004	bdl	0.001
Ti	bdl	0.001	0.001	0.003
Al	0.002	bdl	0.001	bdl
Cr	0.003	0.001	bdl	bdl
Fe^{2+}	0.550	0.328	0.498	0.341
Mn	0.053	0.047	0.054	0.052
Mg	5.371	5.599	5.431	5.584
Ca	0.014	0.014	0.014	0.016
Sum cations	5.995	5.994	5.999	5.997
	0.905	0.942	0.914	0.940
	0.093	0.055	0.084	0.057
	0.002	0.002	0.002	0.003

Table S4. Representative analyses of clinopyroxene mineral chemistry (EMPA) in Champorcher valley serpentinites and metasomatic horizon

Lithology	MH1	MH2	MH2	MH2	MH2	MH2	Massive serp.	Massive serp.	Massive serp.	Massive serp.	Massive serp.	Massive serp.
Sample	B5-S4-176	B8-S3-38	B11-S4-248	B13-S1-134	B13-S2-140	B13-S5-159	C1-S1-60	C1-S2-71	C1-S3-79	C1-S4-84	C1-S6-102	C1-S8-128
Mineral	Cpx	Cpx	Cpx	Cpx	Cpx	Cpx	Cpx	Cpx	Cpx	Cpx	Cpx	Cpx
Textural	Inclusion in	Inclusion in	Inclusion in	Within micro-	Within fold	Within micro-	Cpx porphyro-	Relict in Srp	Cpx porphyro-	Relict in Srp	Cpx porphyro-	Cpx porphyro-
wt.%												
SiO_2	54.82	56.29	55.63	55.01	55.07	54.56	55.74	55.10	55.76	54.92	54.17	55.75
TiO_2	bdl	0.03	bdl	bdl	bdl	bdl	0.02	bdl	0.06	0.03	bdl	0.04
Al_2O_3	bdl	0.02	0.01	0.03	0.04	bdl	0.05	0.06	bdl	0.05	bdl	0.06
Cr_2O_3	0.05	0.07	0.23	0.13	0.07	bdl	bdl	0.06	bdl	bdl	bdl	0.08
Fe_2O_3	bdl	0.31	0.21	0.19	0.28	0.07	0.41	0.36	0.44	0.39	0.26	0.53
FeO	1.20	1.34	1.17	3.03	2.06	2.55	1.47	1.59	1.29	1.27	1.48	1.50
MnO	0.09	bdl	0.06	0.17	0.05	0.06	0.10	0.03	0.14	0.16	0.12	0.13
NiO	0.07	0.07	0.07	bdl	bdl	0.02	0.02	0.07	bdl	bdl	0.03	0.03
MgO	17.47	17.39	17.59	16.24	16.66	16.75	17.48	17.04	17.33	17.16	17.27	17.59
CaO	25.84	24.99	24.78	24.80	25.62	25.97	24.60	24.89	24.70	24.72	25.68	24.17
Na_2O	bdl	0.13	0.18	0.13	0.16	0.02	0.18	0.20	0.16	0.16	0.10	0.23
K_2O	0.01	0.01	bdl	0.01	bdl	0.01	bdl	bdl	0.02	bdl	bdl	0.02
TOTAL	99.57	100.61	99.94	99.74	100.00	100.01	100.06	99.38	99.86	98.84	99.11	100.08
Normalization on the basis of 12 CHARGES and Fe^{3+} = Acmite												
Si	1.999	2.021	2.013	2.012	2.005	1.994	2.015	2.010	2.018	2.011	1.990	2.014
Ti	bdl	0.001	bdl	bdl	bdl	bdl	0.001	bdl	0.002	0.001	bdl	0.001
Al	bdl	0.001	bdl	0.001	0.002	bdl	0.002	0.003	bdl	0.002	bdl	0.003
Cr	0.001	0.002	0.007	0.004	0.002	bdl	bdl	0.002	bdl	bdl	bdl	0.002
Fe^{3+}	bdl	0.008	0.006	0.005	0.008	0.002	0.011	0.010	0.012	0.011	0.007	0.014
Fe^{2+}	0.037	0.040	0.036	0.093	0.063	0.078	0.044	0.048	0.039	0.039	0.045	0.046
Mn	0.003	bdl	0.002	0.005	0.002	0.002	0.003	0.001	0.004	0.005	0.004	0.004
Ni	0.002	0.002	0.002	bdl	bdl	0.001	0.001	0.002	bdl	bdl	0.001	0.001
Mg	0.949	0.931	0.949	0.885	0.904	0.912	0.942	0.927	0.935	0.937	0.945	0.947
Ca	1.009	0.961	0.961	0.972	0.999	1.017	0.953	0.973	0.958	0.970	1.011	0.935
Na	bdl	0.009	0.013	0.009	0.011	0.001	0.013	0.014	0.011	0.011	0.007	0.016
K	0.001	0.001	bdl	0.001	bdl	0.001	bdl	bdl	0.001	bdl	bdl	0.001
Sum cations	4.001	3.977	3.987	3.988	3.995	4.006	3.984	3.990	3.980	3.987	4.010	3.984
#Mg(Fe^{2+})	0.963	0.958	0.964	0.905	0.935	0.921	0.955	0.950	0.960	0.960	0.954	0.954
#Mg(Fe_{tot})	0.963	0.950	0.958	0.900	0.928	0.920	0.944	0.941	0.948	0.950	0.947	0.941
Fe^{3+}/Fe_{tot}	–	0.171	0.137	0.053	0.108	0.024	0.203	0.169	0.233	0.219	0.136	0.240
WO%	50.6	49.7	49.4	49.8	50.8	50.7	49.1	49.9	49.6	49.9	50.5	48.5
EN%	47.6	48.2	48.8	45.4	46.0	45.5	48.6	47.6	48.4	48.1	47.2	49.1
FS%	1.8	2.1	1.8	4.8	3.2	3.9	2.3	2.5	2.0	2.0	2.3	2.4

(bdl) = below the detection limit (0.01 wt.% for all oxides).

Mineral abbreviations adopted from Whitney and Evans (2010). Serp. = serpentinite

#Mg(Fe^{2+}) = Mg/(Mg+Fe^{2+}); #Mg(Fe_{tot}) = Mg/(Mg+Fe_{tot})

*WO% = Ca/(Ca+Mg+Fe^{2+})*100; EN% = Mg/(Ca+Mg+Fe^{2+})*100; FS% = Fe^{2+}/(Ca+Mg+Fe^{2+})*100*

Table S5. Representative analyses of chlorite mineral chemistry (EMPA) in Champorcher valley serpentinites and metasomatic horizon

Lithology	MH1	MH1	MH2	MH2	MH2	MH2	MH2	Massive serp.	Massive serp.	Massive serp.	Massive serp.	MH3
Sample	B5-S2-47	B5-S4-180	B8-S3-37	B11-S3-229	B11-S5-256	B13-S1-129	B13-S3-152	C1-S3-76	C1-S4-86	C1-S6-104	C1-S8-126	H5-S3-285
Mineral	Chl	Chl	Chl	Chl	Chl	Chl	Chl	Chl	Chl	Chl	Chl	Chl
Textural occurrence	Replace Amp	Inclusion in Amp	Replace Amp	Replace Amp	Replace Amp	Chl S2 film	Chl S2 film	Replace Cpx	Srp2 + Chl (ex Opx)	Inclusion in Cpx	Replace Cpx	Inclusion in Amp
wt.%												
SiO_2	30.62	30.46	31.44	30.55	32.01	33.13	32.38	34.48	33.15	37.12	33.83	30.63
TiO_2	bdl	0.07	0.05	0.03	bdl	0.05	bdl	0.10	bdl	0.08	0.03	bdl
Al_2O_3	16.20	15.84	14.84	15.70	13.63	13.46	14.99	12.69	12.26	7.54	12.52	17.14
Cr_2O_3	1.81	0.93	2.86	2.94	2.41	1.23	1.13	0.20	0.51	1.69	0.56	2.04
Fe_2O_3	0.16	0.85	bdl	bdl	bdl	bdl	bdl	bdl	0.34	bdl	bdl	bdl
FeO	9.22	9.15	6.17	7.96	6.85	6.00	7.10	4.57	4.44	3.53	4.83	10.81
MnO	0.03	0.05	0.02	bdl	0.04	0.02	0.05	0.03	0.07	0.07	0.02	0.11
NiO	0.64	0.74	0.86	0.46	0.65	0.50	0.47	0.18	0.37	0.43	0.26	0.41
MgO	28.37	28.28	30.62	29.18	30.44	31.86	30.89	34.03	33.08	27.98	33.46	26.26
CaO	0.03	0.06	0.07	0.43	0.02	0.03	0.06	0.04	0.01	6.02	0.02	0.20
Na_2O	0.08	0.03	bdl	bdl	0.05	0.04	0.02	bdl	0.02	0.03	0.02	bdl
K_2O	0.06	0.05	bdl	bdl	0.03	bdl	bdl	bdl	0.01	0.04	bdl	bdl
H_2O	12.24	12.14	12.33	12.28	12.21	12.36	12.41	12.52	12.20	11.88	12.38	12.14
TOTAL	87.25	86.46	86.97	87.26	86.14	86.32	87.10	86.32	84.26	84.55	85.59	87.59
CATIONS calculated on the basis of 28 OXYGENS												
Si	6.000	6.021	6.116	5.968	6.289	6.431	6.260	6.604	6.519	7.497	6.553	6.050
Ti	bdl	0.010	0.007	0.004	bdl	0.007	bdl	0.014	bdl	0.012	0.004	bdl
Al	3.742	3.690	3.402	3.615	3.156	3.079	3.416	2.864	2.842	1.795	2.858	3.990
Cr	0.280	0.145	0.440	0.454	0.374	0.189	0.173	0.030	0.079	0.270	0.086	0.319
Fe^{3+}	0.023	0.127	bdl	bdl	bdl	bdl	bdl	bdl	0.051	bdl	bdl	bdl
Fe^{2+}	1.511	1.513	1.004	1.300	1.126	0.974	1.148	0.732	0.730	0.596	0.782	1.786
Mn	0.005	0.008	0.003	bdl	0.007	0.003	0.008	0.005	0.012	0.012	0.003	0.018
Ni	0.101	0.118	0.135	0.072	0.103	0.078	0.073	0.028	0.059	0.070	0.041	0.065
Mg	8.286	8.331	8.878	8.496	8.915	9.218	8.902	9.714	9.696	8.423	9.661	7.731
Ca	0.006	0.013	0.015	0.090	0.004	0.006	0.012	0.008	0.002	1.303	0.004	0.042
Na	0.030	0.012	bdl	bdl	0.019	0.015	0.008	bdl	0.008	0.012	0.008	bdl
K	0.015	0.013	bdl	bdl	0.008	bdl	bdl	bdl	0.003	0.010	bdl	bdl
H	16.000	16.000	16.000	16.000	16.000	16.000	16.000	16.000	16.000	16.000	16.000	16.000
Sum cations	20.000	20.000	20.000	20.000	20.000	20.000	20.000	20.000	20.000	20.000	20.000	20.000
#Mg(Fe^{2+})	0.846	0.846	0.898	0.867	0.888	0.904	0.886	0.930	0.930	0.934	0.925	0.812
#Mg(Fe_{tot})	0.844	0.836	0.898	0.867	0.888	0.904	0.886	0.930	0.925	0.934	0.925	0.812
$Al^{(IV)}$	2.000	1.980	1.884	2.032	1.711	1.569	1.740	1.396	1.481	0.503	1.447	1.950
$Al^{(VI)}$	1.742	1.710	1.518	1.583	1.445	1.510	1.676	1.468	1.361	1.292	1.411	2.039
#Fe_{tot}	0.156	0.164	0.102	0.133	0.112	0.096	0.114	0.070	0.075	0.066	0.075	0.188
Fe^{3+}/Fe_{tot}	0.015	0.078	–	–	–	–	–	–	0.065	–	–	–

(bdl) = below the detection limit (0.01 wt.% for all oxides).

Mineral abbreviations adopted from Whitney and Evans (2010). Serp. = serpentinite

#Mg(Fe^{2+}) = Mg/(Mg+Fe^{2+}); #Mg(Fe_{tot}) = Mg/(Mg+Fe_{tot})

Table S6. Representative analyses of spinel group mineral chemistry (EMPA) in Champorcher valley serpentinites and metasomatic horizon

Lithology	Foliated serp.	Foliated serp.	Foliated serp.	Foliated serp.	MH1	MH1	MH2	MH2	MH2	MH2	MH2	Massive serp.	Massive serp.	Massive serp.
Sample	B1-S1-1	B1-S1-3	B1-S1-6	B1-S4-20	B5-S2-48	B5-S2-49	B8-S3-36	B11-S1-202	B11-S3-236	B11-S3-237	B13-S4-155	C1-S2-67	C1-S2-67	C1-S6-107
Mineral	Al-Chr	Chr	Cr-Mag	Mag	Fe-Chr	Mag	Mag	Mag	Mag	Fe-Chr	Mag	Fe-Chr	Mag	Mag
Textural occurrence	Relict grain (core)	Relict grain (rimI)	Relict grain (rimII)	fine grains in Srp matrix	Relict grain (core)	Relict grain (rim)	Inclusion trails in Amp //S2	fine grains along S2	Relict grain (rim)	Relict grain (core)	Euehdral crystals	Relict grain (core)	Relict grain (rim)	// to incipient S2
wt. %														
SiO_2	0.02	0.07	0.08	0.04	3.17	0.11	0.06	0.03	0.05	0.07	0.06	0.30	0.56	0.36
TiO_2	0.17	0.36	0.18	0.02	0.50	0.13	0.10	0.07	0.11	0.38	0.26	0.50	bdl	0.07
Al_2O_3	29.81	5.27	0.57	0.03	1.32	bdl	bdl	0.03	bdl	0.22	bdl	0.09	0.22	0.03
Cr_2O_3	36.83	31.80	10.91	1.73	11.25	1.61	1.64	2.39	6.26	26.62	1.67	20.76	1.24	0.02
Fe_2O_3	bdl	31.18	58.40	67.71	48.34	68.13	67.95	67.11	63.61	40.57	68.52	46.87	66.63	68.92
FeO	27.93	29.82	30.45	30.97	31.25	31.39	30.74	31.03	30.57	29.91	31.33	29.59	30.37	30.95
MnO	0.51	0.78	0.25	0.02	0.18	0.05	0.05	0.06	0.06	0.49	bdl	1.26	0.04	bdl
NiO	0.20	0.22	0.55	0.36	0.46	0.39	0.50	0.31	0.81	0.54	0.57	0.40	0.28	0.32
MgO	5.44	1.37	0.50	0.03	2.56	0.05	0.07	0.08	0.18	0.50	0.19	0.69	0.62	0.35
CaO	0.02	bdl	bdl	bdl	0.03	bdl	0.22	bdl	0.04	0.02	bdl	0.03	0.03	0.04
Na_2O	bdl	0.05	0.03	bdl	bdl	bdl	bdl	bdl	0.02	bdl	bdl	0.01	0.04	0.01
K_2O	bdl	0.01	0.01	0.01	bdl	bdl	bdl	bdl	bdl	bdl	bdl	bdl	bdl	0.01
TOTAL	100.94	97.81	96.14	94.14	94.21	95.08	94.53	94.40	95.40	95.26	95.82	95.83	93.36	94.16
Normalization on the basis of 3 CATIONS and 8 CHARGES														
Si	0.001	0.003	0.003	0.002	0.118	0.004	0.002	0.001	0.002	0.003	0.002	0.011	0.021	0.014
Ti	0.004	0.010	0.005	0.001	0.014	0.004	0.003	0.002	0.003	0.011	0.007	0.014	bdl	0.002
Al	1.092	0.224	0.025	0.001	0.058	bdl	bdl	0.001	bdl	0.010	bdl	0.004	0.010	0.001
Cr	0.905	0.908	0.322	0.052	0.330	0.048	0.049	0.072	0.187	0.801	0.049	0.618	0.037	0.001
Fe^{3+}	bdl	0.847	1.640	1.943	1.349	1.936	1.940	1.921	1.804	1.162	1.931	1.328	1.913	1.968
Fe^{2+}	0.726	0.900	0.950	0.988	0.969	0.991	0.975	0.987	0.964	0.952	0.981	0.932	0.969	0.982
Mn	0.013	0.024	0.008	0.001	0.006	0.002	0.002	0.002	0.002	0.016	bdl	0.040	0.001	bdl
Ni	0.005	0.006	0.017	0.011	0.014	0.012	0.015	0.010	0.025	0.017	0.017	0.012	0.009	0.010
Mg	0.252	0.074	0.028	0.002	0.142	0.003	0.004	0.005	0.010	0.028	0.011	0.039	0.035	0.020
Ca	0.001	bdl	bdl	bdl	0.001	bdl	0.009	bdl	0.002	0.001	bdl	0.001	0.001	0.002
Na	bdl	0.004	0.002	bdl	bdl	bdl	bdl	bdl	0.002	bdl	bdl	0.001	0.003	0.001
K	bdl	0.001	0.001	0.001	bdl	bdl	bdl	bdl	bdl	bdl	bdl	bdl	bdl	0.001
#Mg(Fe^{2+})	0.258	0.076	0.028	0.002	0.127	0.003	0.004	0.005	0.010	0.029	0.011	0.040	0.035	0.020
Al-spinels	0.547	0.113	0.013	0.001	0.033	–	–	0.001	–	0.005	–	0.002	0.005	0.001
Cr-spinels	0.453	0.459	0.162	0.026	0.190	0.024	0.025	0.036	0.094	0.406	0.025	0.317	0.019	0.000
Fe^{3+}-spinels	–	0.428	0.825	0.973	0.777	0.976	0.975	0.963	0.906	0.589	0.975	0.681	0.976	0.999

(bdl) = below the detection limit (0.01 wt.% for all oxides).

Mineral abbreviations adopted from Whitney and Evans (2010). Serp. = serpentinite

#Mg(Fe^{2+}) = Mg/(Mg+Fe^{2+}); Al-spinels = Al/(Cr+Al+Fe^{3+}); Cr-spinels = Cr/(Cr+Al+Fe^{3+}); Fe^{3+}-spinels= Fe^{3+}/(Cr+Al+Fe^{3+})

Table S7. Oxygen and Carbon isotopic composition of carbonates from Lake Miserin Ophiolite and Oxygen isotopic composition of aqueous fluid calculated in equilibrium with carbonates at 350, 400 and 500°C.

Unit	Lithotype	Textural occurrence	Mineralogy	Sample	Analysis point	Petrography and Cathodoluminescence	δ13C VPDB	Sd δ13C	δ18O VPDB	Sd δ18O	δ18O VSMOW (using Kim et al. 2015)	Average δ13C	Average Sd δ13C	Average δ18O VPDB	Average Sd δ18O	Average δ18O VSMOW	Zheng (1999) (0-1200°C)						Golyshev et al. (1981) (100-650°C)					
																	δ18O fluid at 350 °C	δ18O fluid at 400 °C	δ18O fluid at 550 °C	Average δ18O fluid at 350 °C	Average δ18O fluid at 400 °C	Average δ18O fluid at 550 °C	δ18O fluid at 350 °C	δ18O fluid at 400 °C	δ18O fluid at 550 °C	Average δ18O fluid at 350 °C	Average δ18O fluid at 400 °C	Average δ18O fluid at 550 °C
CSU	Calcschist	Carbonate lithons	Cal	MIS64bis	1	Non luminescent subhedral (200-300 microns crystals) with bright orange luminescent rims of last growth phase	-3.9	0.05	-7.8	0.07	22.9	**Calcite carbonate lithons (n=4)**					18.4	19.3	20.9	**Calcite lithons (n=4)**			20.5	21.6	23.7	**Calcite lithons (n=4)**		
CSU	Calcschist	Carbonate lithons	Cal	MIS64bis	1BIS		-3.9	0.05	-8.0	0.05	22.7						18.1	19.0	20.7				20.2	21.3	23.5			
CSU	Calcschist	Carbonate lithons	Cal	MIS64bis	2		-3.4	0.05	-8.1	0.06	22.6	**-3.6**	**0.04**	**-7.9**	**0.06**	**22.7**	18.1	19.0	20.6	**18.2**	**19.1**	**20.8**	20.2	21.3	23.4	**20.3**	**21.4**	**23.6**
CSU	Calcschist	Carbonate lithons	Cal	MIS64bis	2BIS		-3.4	0.03	-7.9	0.05	22.8						18.2	19.1	20.8				20.3	21.4	23.6			
CCU	BrFm1	Late carb vein	Cal	MIS46	A	Bright orange luminescent	1.1	0.02	-13.1	0.04	17.6	**Serpentinite clast (n=4)**					13.0	13.9	15.6	**Serpentinite clast (n=4)**			15.1	16.2	18.4	**Serpentinite clast (n=4)**		
CCU	BrFm1	Late carb vein	Cal	MIS46	B		1.2	0.08	-13.0	0.06	17.5						12.9	13.8	15.5				15.0	16.1	18.3			
CCU	BrFm1	Serpentinite clast	Cal	MIS46	1	Bright orange luminescent	2.2	0.07	-13.6	0.02	16.9	**2.1**	**0.05**	**-13.4**	**0.04**	**17.1**	12.4	13.3	15.0	**12.6**	**13.5**	**15.1**	14.5	15.6	17.8	**14.7**	**15.8**	**17.9**
CCU	BrFm1	Serpentinite clast	Cal	MIS46	1BIS		2.2	0.02	-13.5	0.06	17.0						12.5	13.4	15.1				14.6	15.7	17.9			
CCU	BrFm1	Serpentinite clast	Cal	MIS46	2		2.0	0.06	-13.2	0.04	17.3	**Matrix (n=4)**					12.7	13.6	15.3	**Matrix (n=4)**			14.8	15.9	18.1	**Matrix (n=4)**		
CCU	BrFm1	Serpentinite clast	Cal	MIS46	2BIS		2.0	0.05	-13.3	0.05	17.2						12.6	13.6	15.2				14.8	15.9	18.0			
CCU	BrFm1	Matrix	Dol (Cal <5%)	MIS46	3	Subhedral (equigranular, interlobate to polygonal) Dol2 crystals (100-300 microns in size) bright to dull luminescent embedded in a dull to non luminescent matrix (Dol3?)	1.8	0.02	-14.1	0.02	16.4	**1.8**	**0.05**	**-14.1**	**0.03**	**16.3**	11.7	12.6	14.3	**11.6**	**12.6**	**14.3**	12.5	13.7	16.1	**12.4**	**13.6**	**16.0**
CCU	BrFm1	Matrix	Dol (Cal <5%)	MIS46	3BIS		1.9	0.14	-14.1	0.05	16.4						11.7	12.6	14.3				12.5	13.7	16.1			
CCU	BrFm1	Matrix	Dol (Cal <5%)	MIS46	4		1.7	0.02	-14.2	0.03	16.2	**Late carb vein (n=4)**					11.5	12.5	14.2	**Late carb vein (n=4)**			12.4	13.6	15.9	**Late carb vein (n=4)**		
CCU	BrFm1	Matrix	Dol (Cal <5%)	MIS46	4BIS		1.7	0.02	-14.1	0.03	16.3						11.6	12.6	14.3				12.5	13.7	16.0			
CCU	BrFm1	Late carb vein	Cal	MIS46	5	Bright orange luminescent	1.3	0.03	-12.9	0.03	17.6	**1.3**	**0.04**	**-13.0**	**0.06**	**17.5**	13.0	14.0	15.6	**13.0**	**13.9**	**15.6**	15.2	16.3	18.4	**15.1**	**16.2**	**18.4**
CCU	BrFm1	Late carb vein	Cal	MIS46	5BIS		1.4	0.04	-13.0	0.09	17.5						13.0	13.9	15.6				15.1	16.2	18.3			
MH	MH1	Carb porphyroblasts	Dol (Cal <1%)	E9	A	Dol1 porphyroblast of inclusion-rich anhedral dolomite crystals 1-2 mm in size partially recrystallized by limpid Dol2	0.5	0.04	-14.8	0.04	15.7	**Dol porphyroblast (n=7)**					11.0	11.9	13.6	**Dol porphyroblast (n=7)**			11.8	13.0	15.4	**Dol porphyroblast (n=7)**		
MH	MH1	Carb porphyroblasts	Dol (Cal <1%)	E9	B		0.9	0.03	-17.0	0.06	13.4						8.7	9.7	11.4				9.5	10.7	13.1			
MH	MH1	Carb porphyroblasts	Dol (Cal <1%)	E9	C		0.5	0.04	-15.6	0.06	14.8						10.1	11.1	12.8				11.0	12.2	14.5			
MH	MH1	Carb porphyroblasts	Dol (Cal <1%)	E9	1		0.8	0.07	-16.6	0.07	13.8	**0.7**	**0.05**	**-16.0**	**0.06**	**14.4**	9.1	10.0	11.7	**9.7**	**10.7**	**12.4**	9.9	11.1	13.5	**10.6**	**11.8**	**14.1**
MH	MH1	Carb porphyroblasts	Dol (Cal <1%)	E9	1BIS		0.8	0.05	-16.6	0.03	13.8						9.1	10.0	11.8				9.9	11.1	13.5			
MH	MH1	Carb porphyroblasts	Dol (Cal <1%)	E9	2		0.5	0.04	-15.8	0.05	14.6						9.9	10.9	12.6				10.7	11.9	14.3			
MH	MH1	Carb porphyroblasts	Dol (Cal <1%)	E9	2BIS		0.6	0.09	-15.6	0.08	14.9						10.2	11.1	12.8				11.0	12.2	14.6			
Metaophiolite basement	Metaophicarbonate	Intrafolial carb vein	Cal	6	A	Calcite filling a syn-D_2 intrafolial vein	2.3	0.02	-20.0	0.03	10.3	**Intrafolial carbonate vein (n=4)**					5.8	6.7	8.4	**Intrafolial carb vein (n=4)**			7.9	9.0	11.2	**Intrafolial carb vein (n=4)**		
Metaophiolite basement	Metaophicarbonate	Intrafolial carb vein	Cal	6	B		2.4	0.02	-20.6	0.01	9.6						5.1	6.0	7.7				7.2	8.3	10.5			
Metaophiolite basement	Metaophicarbonate	Intrafolial carb vein	Cal	6	C		2.3	0.01	-20.6	0.03	9.6	**2.4**	**0.02**	**-20.5**	**0.02**	**9.8**	5.1	6.0	7.7	**5.2**	**6.1**	**7.8**	7.2	8.3	10.5	**7.4**	**8.4**	**10.6**
Metaophiolite basement	Metaophicarbonate	Intrafolial carb vein	Cal	6	D		2.4	0.03	-20.8	0.03	9.5						5.0	5.9	7.6				7.1	8.2	10.3			

Carb - Fluid	T (°C) range	Reference	Equations	$\Delta_{carb-H2O} = 10^3 ln\alpha$ 350 °C	400 °C	550 °C
Calcite-H2O	100-650	Golyshev et al. (1981)	$10^3 ln\alpha = 2.96*10^6/T^2 + 0*10^3/T + (-5.19)$	2.4	1.3	-0.8
	0-1200	Zheng (1999)	$10^3 ln\alpha = 4.01*10^6/T^2 + (-4.66)*10^3/T + 1.71$	4.6	3.6	2.0
Dolomite-H2O	100-650	Golyshev et al. (1981)	$10^3 ln\alpha = 3.26*10^6/T^2 + 0*10^3/T + (-4.51)$	3.9	2.7	0.3
	0-1200	Zheng (1999)	$10^3 ln\alpha = 4.06*10^6/T^2 + (-4.65)*10^3/T + 1.71$	4.7	3.8	2.1